THÈSE DE DOCTORAT EN COTUTELLE

SIMULATIONS ET OPTIMISATION DE SYSTÈMES DE STOCKAGE ET DE PURIFICATION D'HYDROGÈNE EN UTILISANT DES ADSORBANTS ET DES HYDRURES MÉTALLIQUES

SIMULATION AND OPTIMIZATION OF HYDROGEN STORAGE AND PURIFICATION USING ADSORBENTS AND METAL HYDRIDES

THÈSE PRÉSENTÉE À
L'UNIVERSITÉ DU QUÉBEC À TROIS-RIVIÈRES
ET À
WUHAN UNIVERSITY OF TECHNOLOGY
COMME EXIGENCE PARTIELLE DU
DOCTORAT EN SCIENCES DE L'ÉNERGIE ET DES MATÉRIAUX

PAR
LIANG TONG

MAI 2020

Simulation and Optimization of Hydrogen Storage and Purification Using Adsorbents and Metal Hydrides

Ph.D. Candidate: Liang Tong

Under the guidance of

Prof. Pierre Bénard & Prof. Jinsheng Xiao

(*Supervisor*) (*Co-supervisor*)

28 November, 2019

Members of Jury:

Pierre Bénard, Ph. D., directeur de recherché	Université du Québec à Trois-Rivières
Jinsheng Xiao, Ph. D., codirecteur de recherche	Wuhan University of Technology, China
Fuwu Yan, Ph. D., président du jury	Wuhan University of Technology, China
Richard Chahine, Ph. D., évaluateur	Université du Québec à Trois-Rivières
Zaoxiao Zhang, Ph. D., évaluateur externe	Xi'an Jiaotong University, China
Qifeng Tian, Ph. D., évaluateur	Wuhan Institute of Technology, China
Pang-Chieh Sui, Ph. D., évaluateur	Wuhan University of Technology, China
Shichun Mu, Ph. D., évaluateur	Wuhan University of Technology, China

摘 要

高效的氢气储存和氢气纯化在能源市场中占有重要地位。氢气可以通过物理方法或化学方法进行储存，例如，基于吸附剂的吸附/脱附过程和基于金属氢化物的吸氢/脱氢过程。氢气也可以通过物理方法利用吸附剂，或通过化学方法利用金属氢化物，从含氢气体混合物中分离出来，达到氢气纯化的目的。本文主要针对基于微孔材料吸附作用和氢化物吸收作用的储氢和氢气纯化系统，通过数值模拟研究了储氢和氢气纯化系统的优化策略。

对于物理储氢，本文以大型活性炭氢气储运罐为研究对象，将贯通冷却方式应用于加氢过程，增加储运罐的储氢量，提升储氢系统效率。对于化学储氢，本文针对金属氢化物储氢罐建立了集总参数模型，研究储氢罐整体性能。同时基于基本的热力学模型，推导出金属氢化物储氢系统的集总温度的解析解。该解析解可作为一种衡量标准，用来验证集总参数/分布参数模型。另外，本文也建立分布参数模型研究氢化过程中热效应对其系统性能的影响。由于氢化过程伴随着大量反应热的释放，可将螺旋管换热器应用于金属氢化物储氢系统，降低金属氢化物储氢罐罐内温度。本文建立了完整的三维模型，研究配备螺旋管换热器的金属氢化物储氢罐的储氢性能，考虑不同种类的换热器对其性能的影响。同时，为了简化计算，针对配备螺旋管换热器的储罐建立简化的二维模型，通过将简化的二维模型的结果与三维模型的结果对比，验证二维模型的有效性。

相变材料可用于储热。本文以石蜡 R35 作为相变材料，尝试将其与铜制和铝制金属泡沫相结合，提高复合相变材料的有效热导率。本文将传统的相变材料与金属泡沫相结合，应用于金属氢化物储氢罐，通过模拟研究，优化系统性能。

利用物理方法或化学方法，可将氢气从混合气体中分离和提纯。目前变压吸附（PSA）广泛应用于氢气纯化。对于基于物理吸附方式的氢气纯化系统，本文以沸石 5A 为吸附剂，基于扩展 Langmuir 等温线模型和一维计算流体动力学（CFD）方案，建立并验证了建模策略，从而模拟氢气纯化 PSA 过程。本文同

时研究了真空变压吸附（VPSA）过程，结果表明真空变压吸附过程对提升氢气纯度有显著影响。随后，将验证后的变压吸附模型用来模拟不同操作条件下的系统性能，产生数据库，并用该数据库进行训练人工神经网络模型（ANN）。训练后的人工神经网络模型用于预测氢气纯化系统的性能，结合多目标优化函数，在限制条件内寻找最优操作条件，使得氢气纯化系统性能最优。金属氢化物可应用基于化学方式的氢气纯化系统，通过类似的变压吸附循环过程进行氢气纯化。本文针对基于金属氢化物的氢气纯化系统建立了集总参数模型，通过参数研究，优化氢气纯化系统的性能。

关键词：氢气储存，氢气纯化，金属氢化物，吸附剂，优化

Abstract

Effective hydrogen storage and hydrogen purification play an important role in the energy market. Hydrogen can be stored using physical and chemical methods, such as the adsorption-desorption process based on adsorbents and the hydriding-dehydriding process based on metal hydrides. Hydrogen also can be purified from mixture gases physically using adsorbents and chemically using metal hydrides. In this thesis, we examine storage and purification system optimisation strategies through numerical simulations using both adsorption on highly microporous materials and absorption in hydrides.

In our work on hydrogen storage by physisorption, we examine the use of flow-through cooling in an adsorption-based storage delivery tank in order to improve the system efficiency. We also examine the performance of a chemical storage system based on metal hydrides using a lumped parameter model to investigate system performance. An analytic solution was obtained and used as a benchmark for lumped/distributed parameter models. In addition, distributed parameter models have been developed to examine the thermal effect during hydriding on the system performance. In view of the large reaction heat released during hydriding, the coiled-tube heat exchanger is applied into the metal hydride hydrogen storage tank. Complete 3D models have been used to investigate the performance of metal hydride reactor equipped with complex heat exchanger. Reduced 2D models for coiled-tube heat exchangers have been examined and validated.

Phase change materials such as paraffin RT35 can be used to store the heat energy during phase transition process. We examine their use in conjunction with various metal foams including aluminium foam and copper foam to improve thermal conductivity. These composited phase change materials were integrated to the metal hydride storage system for performance optimization.

Hydrogen can be separated and purified from the gaseous mixtures physically using the adsorption phenomena or chemically through hydration of metallic materials.

Pressure swing adsorption (PSA) is widely used for hydrogen purification. In our work on hydrogen purification by physisorption, we developed and validated a modeling strategy for a system using zeolite 5A based on the extended Langmuir isotherm model and a 1D computational fluid dynamics (CFD) approach in order to simulate the PSA system. The performance of a vacuum pressure swing adsorption (VPSA) system was compared with that of the PSA system. The results show that VSPA can be used effectively to purify hydrogen. The validated PSA model was used to generate a dataset for training an artificial neural network (ANN) model. The trained ANN model and a multi-objective optimization function were used to obtain optimal operation conditions for the performance optimization of hydrogen purification system. Finally, we examined a chemical process based on metal hydrides to purify hydrogen. A lumped parameter model for the metal hydride hydrogen purification system has been developed and validated, the performances of this system are researched through parametric study.

Keywords: Hydrogen storage, hydrogen purification, metal hydride, adsorbent, optimization

Content

Chapter 1 Introduction

1.1 Problem statement and motivation

In order to achieve sustainability, challenges such as our limited reserves of fossil fuels, the environmental consequences of their use (specifically pollution and global warming associated with greenhouse gas (GHG) emissions) should be dealt carefully. Renewable energy sources, such as hydropower, solar energy, wind power and geothermal energy, can be used effectively to mitigate the environmental issues associated with energy utilization.

Hydrogen, which can be produced from renewable energy and fossil fuel[1], has been proposed as an energy vector to displace fossil fuels in such systems as vehicles, submarines, planes and rockets. Due to the low volumetric energy density of hydrogen and the fact that hydrogen is almost always found chemically bound to other elements on earth, effective storage and purification technologies are required to introduce the use of hydrogen in energy systems. In general, hydrogen is stored using methods such as compression[2], cryocompression[3], liquefaction, physical adsorption, chemical absorption and chemical hydrogen carriers. Large amounts of hydrogen from production sites to their end-users are often brought by trucks. Compression and liquefaction of hydrogen are typically used, depending on the distance between the production plant and the end-users.

The sorption processes, including the physical adsorption process and the chemical absorption process, are exothermic. A significant amount of heat is generated in the sorption process while a lot of heat is absorbed in the desorption process. The thermal effect caused by the adsorption heat or the reaction heat can impact the performance of hydrogen storage and purification.

The objective of this work is to study hydrogen storage and purification systems, using validated numerical predictive tools, in order to optimize engineering processes relevant to renewable energy and environmental engineering applications that rely on

gas-solid interactions (sorption phenomena). Various materials are used to store hydrogen and purify hydrogen from the gaseous mixtures through physical and chemical methods. Various models, including the lumped parameter model and the distributed parameter model, are developed on different software platforms. These validated models are used to investigate and search effective methods to improve system performance. The parametric studies have been performed in order to identify the critical parameters that affect the performance of specific sorption-based processes. We examine the use of heat exchanger configurations and processes for hydrogen storage systems based on metal hydrides, and the use of phase change materials to store reaction heat in order to optimize hydrogen storage performance. Artificial intelligence and machine learning methods have been applied to determine optimum operation parameters as a function of hydrogen purification process. The purpose of thesis is to simulate and optimize the hydrogen storage and purification system using adsorbents and metal hydrides.

1.2 Research Background

The thermal effects associated with sorption-based physical or chemical processes must be managed to optimize their performance depending on the intended use. They can affect the storage capacity of materials-based storage systems and the performance and efficiency of purification applications. It is directly relevant to their performance when these processes are used to regulate heat, such as an air conditioning system based on hydriding-dehydriding cycles of metal hydrides.

The method of physical adsorption is attractive for hydrogen storage, and activated carbon adsorption hydrogen storage has been considered as one of the promising storage methods. The adsorbent is chemically and physically modified to improve its hydrogen storage capactiy [4]. Adsorption heat is released when the adsorbent adsorbs hydrogen, and the temperature of the adsorbent bed increases in the adsorption process, which induces a negative effect on the hydrogen storage capacity of the system.

A first approach to the problem is to decrease the equilibrium temperature of the storage tank to increase the storage capacity of an adsorption-based storage tank. The hydrogen

storage capacity of activated carbon tank cooled by room temperature water [5, 6], ice water [6, 7] and liquid nitrogen [8-10] have been investigated through various numerical models, including the lumped parameter models [6, 10] and the distributed parameter models [5, 7-9]. The storage system geometry assumes a dewar container which encloses liquid nitrogen and a tank containing activated carbons in which hydrogen will be store [11]. This coupled model is considered as a good method to optimize the empirical heat transfer coefficient. The hydrogen storage tank packed with the activated carbon cooled by liquid nitrogen shows better performance than that cooled by ice water and room temperature water. The metal-organic framework (MOF) is a high specific surface area material, which can be used as an adsorbent for hydrogen storage. The hydrogen storage capacity of compacted MOF-5 is higher than that of MOF-5 powder [12].

Based on the simple thermodynamic models, the analytical solutions of the lumped temperature for adsorption-based hydrogen storage system [13], compression-based hydrogen storage systems [14] and metal hydride hydrogen storage system [15] have been obtained, which can be used to validate the numerical model. In general, a numerical model, either a lumped parameter model or a distributed parameter model, can be validated by experimental data or analytical solutions obtained using simplified boundary conditions and material properties. The analytical solutions can be considered as a basic benchmark to validate the complicated two-dimensional and three-dimensional numerical models.

The temperature of the adsorbent bed can be decreased not only by changing the ambient temperature around the hydrogen storage tank, but also by the filling gas with a relatively low temperature. The flow-through cooling method can be used to decrease the temperature of the adsorbent bed and improve the hydrogen storage capacity. Normally, the charging process ceases when the pressure in the hydrogen storage tank reaches up to the target value. During the flow-through cooling process, the inlet valve of the tank is kept open until the pressure reaches the target value, at which point the outlet valve of the tank is changed from the closed condition to the open condition. The low-temperature hydrogen is charged into the tank from the inlet, and the high-temperature hydrogen flows out from the tank. The heat released in the adsorption

process is removed with the high-temperature hydrogen, and the temperature of the hydrogen storage tank decreases. The pressure in the tank is maintained to the target value in the flow-through cooling process. The flow-through cooling method is an effective measure to decrease the temperature of the adsorbent bed and increase hydrogen capacity.

The flow-through method has been used to mitigate the thermal effects during filling and improve hydrogen storage capacity [16-18]. Corgnale et al. [16] have examined the hydrogen storage capacity of a tank that uses flow-through cooling. The material gravimetric capacity of a 2.5 L tank filled with MOF-5 is about 11% under optimized conditions (target pressure: 8.5 MPa, minimum temperature in the tank: 110K), exhibiting better performance than those of the carbon materials (MaxSorb®). Ubaid et al. [17] applied the flow-through cooling method to a 20 m^3 cryo-adsorptive hydrogen tank packed with MOF-5 and investigated its hydrogen storage capacity. The pre-cooling method is used in compressed hydrogen storage systems [19], and can also be used in adsorptive hydrogen storage systems. The effects of flow-through cooling and pre-cooling on the hydrogen storage capacity of the 51.4 m^3 adsorptive hydrogen delivery tank have been investigated [18].

The reaction heat in the metal hydride hydrogen storage reactor is larger than the adsorption heat in the adsorptive hydrogen storage tank. The thermal effects in the metal hydride tank have a significant impact on the hydrogen storage performance due to the relatively low thermal conductivity of the metal hydride bed and the large amount of reaction heat released. In general, metal hydrides are classified as AB_5 type, AB type, AB_2 type, and so on. The hydrogen storage properties of metal hydrides can be improved by adding specific elements [20, 21].

The heat and mass transfer in the metal hydride reactor has been studied by many researchers [22-24]. The geometry and structure of the metal hydride reaction bed must be carefully designed to achieve an acceptable performance of hydrogen storage. Various heat exchangers have been applied to the metal hydride tank to improve the hydrogen storage performance. Chung et al. [25] have studied the hydriding and dehydriding processes of the $LaNi_5$ metal hydride reactor based on the Comsol software

platform. The expansion volume, which is usually ignored in most cases, has been considered in their model. The model was validated by comparing simulation results with the published data [26]. In order to enhance the heat transfer in the metal hydride bed, a concentric heat exchanger with fins was used in the Mg_2Ni metal hydride reactor. Their results showed that the reaction rate in the desorption process increased when the reactor was adopted with a heat exchanger pipe and fins [27]. Then, the heat pipes were taken into consideration in the metal hydride reactor. The effect of heat pipes on the absorption and desorption time of a metal hydride tank (contained 295g $LaNi_5$) has been studied experimentally. Their results showed that the heat pipe could be used to improve the reaction rate during absorption and desorption. When the hydrogen supply pressure is set to be 10 atm, the hydriding time can be reduced by more than half. When the outflow rate is set to be 1 L/min, the dehydriding time is increased by 44% [28].

The major parameter affecting the hydrogen storage process of a sodium alanate metal hydride storage system equipped with a honeycomb structured heat exchanger is the wall length of the honeycomb cell when external cooling is used [29]. Then, the multi-tube reactor structure is designed for the hydrogen storage system using sodium alanate hydride, where the longitudinal fin has been taken into consideration, the parametric studies are performed to obtain the main parameters influencing the system performance and improve system efficiency [30]. The honeycomb structure heat exchanger has also been applied to a hydrogen storage system using MOF-5 as adsorbent. This heat exchanger works with electric heating equipment in order to improve the hydrogen desorption performance [31].

Heat pipe is widely used in many fields due to its excellent performance of heat transfer. There are some phase change materials in this device. These special materials can be considered as the carrier to transfer the heat energy from the high-temperature zone to the low-temperature zone.

In general, the heat pipe heat exchanger works based on the space difference while the phase change material heat exchanger works based on the time difference. There is no obvious dynamic displacement for the materials in the phase change material heat exchanger. When the phase change material heat exchanger works, the phase transition

occurs in the same position at different times. As the thermal conductivity of the phase change materials is usually low, the metal foam [32] and the heat transfer fluid pipe [33] can be used to improve the heat transfer in the phase change materials. The phase change material heat exchanger can be applied for the metal hydride reactor and the battery. As for the metal hydride reactor, the phase change material heat exchanger can be used to adsorb the reaction heat during hydriding in order to decrease the temperature of the metal hydride reactor and improve the hydrogen storage capacity of the system, and release the heat energy during dehydriding to increase the rate of dehydriding. The materials transfer from the solid state to the liquid state during hydriding, and from the liquid state to the solid state during dehydriding. As for the battery, the phase change material heat exchanger is used to present the severe temperature rise and make sure the battery to be safe [34-36].

Gkanas et al.[37] have studied various three-dimensional models for metal hydride reactor and presented three designs of the cooling tubes, including the plain embedded tubes, the transverse finned tubes and the longitudinal finned tubes. Wu et al. [38] investigated the hydrogen storage performance of the Mg-based metal hydride reactor equipped with the helical coil heat exchanger and studied the various helical coil heat exchangers. The coiled-tube heat exchanger has been used in high-pressure hydrogen storage system using metal hydrides [39, 40]. Assuming the coiled-tube as several parallel ring tubes, a reduced two-dimensional model for the $LaNi_5$ metal hydride reactor with the coiled-tube heat exchanger was developed for simplification, the simulation results of the reduced two-dimensional model agreed with those of the completed three-dimensional model [41].

Metal foam (MF) can be used in the metal hydride (MH) tank to increase the effective conductivity of metal hydride bed and improve the hydrogen storage efficiency. Laurencelle et al.[42] validated their 1D model for the metal hydride reactor equipped with aluminium foam by the experimental data, and the impact of different aluminium foams cell sizes on the performance of metal hydride system was studied. Mellouli et al. [43] presented a 2D mathematical model and showed their simulation results agreed well with the work of Laurencelle [42], and the effects of different metal foams,

including zinc, copper and aluminium foams, on the mass of absorbed hydrogen were studied.

Phase change materials (PCM) can be used to store the heat energy during the phase transition process and received wide attention [44]. Phase change materials were introduced into the metal hydride hydrogen storage system [33, 45-47]. The effects of the physical parameters of phase change materials , the configuration of metal hydride tank [47] and the heat transfer fluid pipe between metal hydride bed and phase change materials [33] on the metal hydride system have been studied. Metal foam (MF) was widely used in metal hydride (MH) beds to increase its effective thermal conductivity [48-50]. Therefore metal foam (MF) can be used in conjunction with phase change materials (PCM) to improve the heat transfer performance [32] . Phase change materials (PCM) composited with metal foam (MF) can be applied to the metal hydride (MH) system [51].

Metal hydrides, which were traditionally used for hydrogen storage [52], have recently been proposed for hydrogen purification [53-60]. Talaganis et al. [52] set up a lumped model for hydrogen storage using metal hydrides. A validated model was then developed to simulate and analyse hydrogen purification processes [53]. Saitou et al. [54] carried out an experimental investigation to study the performance of the hydrogen purification system using $FeTi_{0.95}Mm_{0.08}$ sintered pellets pressed with copper. Minko et al. [55,56] developed a mathematical model to analyse metal hydride system, and investigated the effect of the thickness of the porous bed on the hydrogen purification systems. Then the hydrogen purification reactor equipped with aluminium foam was studied [57,58]. Dunikov et al. [59] discussed the influence of impurities on hydrogen absorption in different AB_5 type metal hydride reactors.

The hydrogen purification process plays an important role to obtain high purity hydrogen and maintain good performance of fuel cell applications. The common processes used for hydrogen purification include pressure swing adsorption, cryogenic separation and membrane separation technologies. Pressure swing adsorption is a widely used method to separate and purify hydrogen from gaseous mixtures. In general, pressure swing adsorption system using adsorbent materials is more widely used than

that using metal hydride.

Various adsorbent materials, such as zeolite [61-66], activated carbon [63-69] and CuBTC [70, 71], have been used as the adsorbent to separate and purify hydrogen by pressure swing adsorption process. Layered bed [64-66,72,73], a so-called combination of different adsorbent materials, can be considered as an effective method to improve the performance of the hydrogen purification system. Of course, some novel adsorbent materials [74] and new technology methods [75,76] are also being studied in order to improve the hydrogen purity and the hydrogen recovery.

In general, there are three steps to study the hydrogen purification pressure swing adsorption system based on the adsorbent, as follows: the adsorption isotherms equation, the breakthrough curve model and the pressure swing adsorption cycle model. The adsorption isotherm of the adsorbate on the adsorbent bed is the basis of the breakthrough curve model. The breakthrough curve model can be used to obtain a breakthrough time when the impurities are detected in the product outlet. The adsorption time in the hydrogen purification pressure swing adsorption process is designed to be lower than the breakthrough time in order to obtain high-purity hydrogen.

Park et.al [77] measured the adsorption isotherms of CO_2, CO, N_2, CH_4, Ar and H_2 on activated carbon and on zeolite LiX as a function of pressures and considered various adsorption isotherm models, such as the Langmuir, Toth and Sips models, to model the uptake as a function of pressure. Based on the adsorption isotherm data [77], the dual-site Langmuir model was selected and used in the four-bed and two-bed pressure swing adsorption system [78]. In most cases, the adsorption isotherms of pure gas on the adsorbent bed are measured. The parameters for the adsorption isotherm model, such as the Langmuir adsorption isotherm equation, can be fitted from the experimental data. Then, the extended adsorption isotherms, such as the extended Langmuir adsorption isotherm equation, can be used to predict the adsorption isotherms of gaseous mixtures on the adsorbent. The parameters used in the adsorption isotherm equation for pure gas are as the same as those for gaseous mixtures. Kloutse et.al directly measured the gaseous mixtures adsorption on CuBTC [79] and MOF-5 [79,80], their adsorption data can be considered as an benchmark to check the adsorption isotherm models.

Casas et.al [81] have presented the breakthrough curve experiment of carbon dioxide and hydrogen mixtures on the activated carbon adsorbent bed, which is considered to be a necessary step for the pressure swing adsorption system. Based on the published experimental data [82], a one-dimensional model for the breakthrough curves of the gaseous mixtures on zeolite adsorbent bed has been developed and implemented on the Comsol software platform [83]. Then, the model of breakthrough curve for a layered bed of activated carbon and zeolite was validated by comparing its simulation results with other works [63]. Xiao et.al studied the thermal effects on the breakthrough curves of pressure swing adsorption [84]. The pressure swing adsorption cycle is difficult to simulate on the Comsol software platform, the Aspen/Adsorption software is considered to develop the pressure swing adsorption model. Based on previous works [83,84], the pressure swing adsorption cycle model for the hydrogen purification system using CuBTC as adsorbent was completed, and applied to optimize the performance of the system by a parametric study [71].

As the nature of the adsorbent materials is important for hydrogen purification systems, new classes of adsorbent materials can be used to improve the performance of pressure swing adsorption processes. Based on the process schedule of the pressure swing adsorption cycle in precious work [68], Jamali et.al [72] have investigated new combinations of materials involving CuBTC, activated carbon and zeolite for hydrogen purification systems. Zhang et al. [62] have compared the performance of the double bed pressure swing adsorption system with that of the single bed pressure swing adsorption system. Their results show that the hydrogen recovery and productivity of the double bed pressure swing adsorption system are higher than that of the single bed system. Moon et al. [73] have analyzed the hydrogen recovery performance of an eight-layered bed pressure swing adsorption process using activated carbon and zeolite, and compared the performance between the four-layered bed and the eight-layered bed system. The eight-layered bed hydrogen purification system showed higher hydrogen recovery than that of a four-layered bed hydrogen purification system. The use of porous membranes has been considered in pressure swing adsorption processes for hydrogen production, and various hybrid schemes were analyzed in order to optimize system performance [75]. Zhu et al. [76] have proposed a two-train elevated-temperature

pressure adsorption process in order to produce hydrogen from coal-fired shifted gas. Song et al. [85] have used heat integration technology to recover the wasted heat for reducing the energy consumption of a steam methane reforming system coupled with pressure swing adsorption process. Golmakani et al. [86] investigated three methods: pressure swing adsorption, vacuum swing adsorption (VSA) and temperature swing adsorption (TSA) for hydrogen purification. Their researches showed that the VSA process could be considered economical method to produce pure hydrogen (>99.99%) from syngas streams for fuel cells application.

Various methods have been used to optimize a pressure swing adsorption system in order to improve their performance [87-90]. Huang et al. [89] carried out the optimization routines of the PSA process for hydrogen purification in gPROMS software. Based on the hydrogen purification model validated by comparing its simulation results with other works [69], Tao et al. [90] have used the Sequential Quadratic Programming method to optimize the vacuum pressure swing adsorption (VPSA) cycle. Makarem et al.[91] used artificial neural network to predict behavior of a VPSA system for oxygen production. Artificial neural network appears to be a good tool to save time for simulations of complex systems.

Machine learning technology has received wide attention in many fields. Artificial neural network is an effective method for predicting and optimizing system performance in various fields, such as estimation of solar radiation [92], prediction of the performance of gas turbine [93] or the products of biomass gasification process [94], research of gas adsorption [95, 96], absorption [97] and separation [87,88]. Morse et al. [95] have simulated and predicted adsorption isotherm behavior by neural networks. The carbon dioxide/methane selectivity of MOFs has been studied using the artificial neural network [98]. Ma et al. [88] applied artificial neural networks to predict the breakthrough curves of the layered bed composited of activated carbon and zeolite, and find the optimal layer ratio of activated carbon to zeolite height and obtain the maximum breakthrough time. Ye et al. [87] examined the performance of a pressure swing adsorption cycle based on the artificial neural network model. The artificial neural network and machine learning methods can be used to predict the cycle life [99] and the

hydrogen uptake [100] of metal hydride systems, and thus play an important role in system optimization.

1.3 Research contents and methods

Lumped parameter model and distributed parameter modeling approaches are used in this work. Various softwares are used to simulate hydrogen storage and purification processes, including Matlab/Simulink, Comsol, Aspen/Adsorption and Matlab/Neural Net Fitting. Lumped parameter models for the hydrogen storage and purification system using metal hydride are set up on Matlab/Simulink platform. Distributed parameter models for the hydrogen storage system using adsorbent and metal hydride are developed on the Comsol software platform. The hydrogen storage performance of the metal hydride tank equipped with the coiled tube heat exchanger or the phase change materials heat exchanger are investigated using a validated model on the Comsol software platform. The Aspen/Adsorption software is used to simulate the hydrogen purification pressure swing adsorption (PSA) process using adsorbent. The trained artificial neural network (ANN) model was developed and implemented on Matlab/Neural Net Fitting software platform. The ANN model was used to predict the performance of the hydrogen purification system, and applied to obtain the optimal operation conditions under the help of multi-objective optimization function.

Table 1.1 Softwares for simulating and optimizing system performance in present work

Software	Application	Classification
Matlab/Simulink	Hydrogen storage and purification using metal hydride	Lumped parameter model
Comsol	Hydrogen storage using metal hydride and adsorbent	Distributed parameter model
Aspen/Adsorption	Hydrogen purification using adsorbent	Distributed parameter model
Matlab/Neural Net Fitting	Hydrogen purification using adsorbent	-

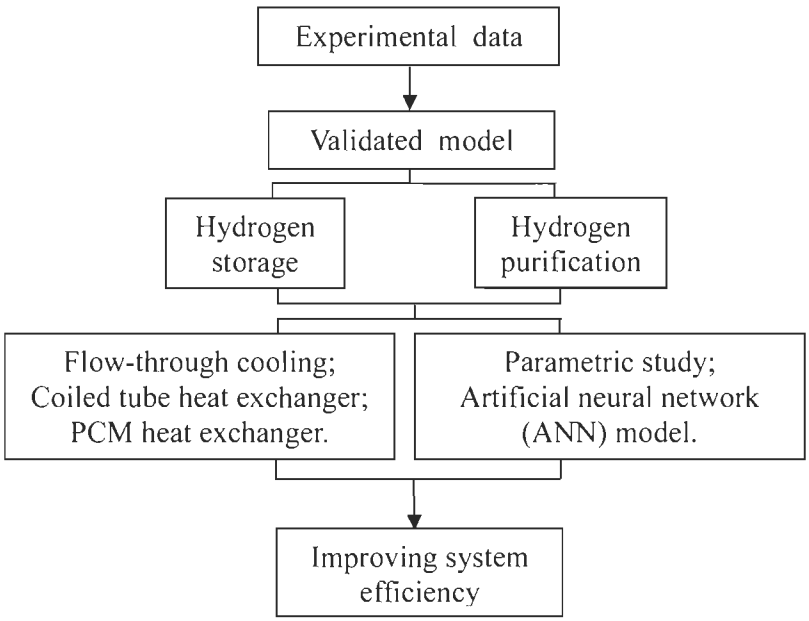

Fig.1.1 Roadmap of this work

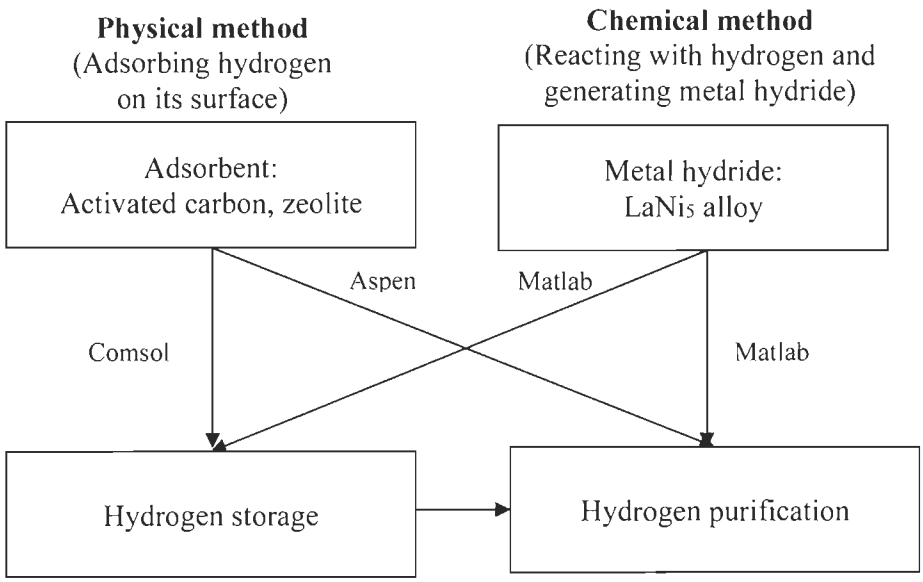

Fig.1.2 Research contents and methods

1.4 Thesis layout

In this work, I present the results of my research on hydrogen storage and hydrogen purification.

First, I studied hydrogen storage systems using activated carbon as adsorbent. The pre-cooling and flow-through cooling methods were applied to the hydrogen delivery tank in order to improve the hydrogen storage capacity. See chapter 2.

Second, analytical solutions of certain thermodynamic properties were obtained from a lumped parameter thermodynamic model for a metal hydride hydrogen storage system for various processes, such as hydriding, dormancy and dehydriding processes. The analytical solutions were applied to validate the numerical model with a constant reaction rate. Then, the variable mass source term is taken into consideration in the validated lumped parameter numerical model. The effect of mass flow rate on the metal hydride hydrogen storage system is discussed in chapter 3.

Third, I studied metal hydride hydrogen storage tanks equipped with various heat exchangers. The thermal effects during hydriding/dehydriding have a significant influence on the system performance of metal hydride hydrogen storage systems, and the coiled tube heat exchanger and the phase change material heat exchanger have been applied to the hydrogen storage system using metal hydride. See chapter 4 and 5.

Fourth, I studied the hydrogen purification pressure swing adsorption system using zeolite 5A as the adsorbent. An artificial neural network model was trained by the dataset produced by the validated hydrogen purification model. The trained artificial neural network model and multi-objective optimization function were used to obtain the optimal operation condition (chapter 6).

Finally, I studied hydrogen purification systems based on metal hydrides. Lumped parameter models were developed for the hydrogen storage system and the hydrogen purification system. Parametric studies were conducted for performance optimization (chapter 7).

Chapter 2 Hydrogen Storage using physisorption

This section has been published in: Tong L, Xiao J S, Cai Y H, et al. Thermal effect and flow-through cooling of an adsorptive hydrogen delivery tank. International Journal of Hydrogen Energy, 2016, 36(41):16094-16100.

My specific contributions in this work was to mitigate thermal effect of adsorption in a large-scale hydrogen delievery tank by pre-cooling and flow-through cooling.

Hydrogen storage is one of the main challenges in hydrogen energy applications. Cryosorption on highly microporous adsorbents has been proposed as a potentiel solution. The thermal effects associated with the adsorption process is an important issue that needs to be studied in detail as it has a great influence on the storage capacity of a cryosorption-based storage system.

2.1 Governing equations for hydrogen storage system

The mass, momentum, energy conservation equations and the modified Dubinin-Astakov isotherm are used in this model and implemented on the Comsol software platform. The governing equations and their validation are detailed in previous work [7, 8].

The mass and momentum conservation equation in porous media is expressed as [7, 8]:

$$\frac{\partial}{\partial t}\left(\varepsilon_b \rho_g\right) + \nabla \cdot \left[\rho_g\left(-\frac{\kappa}{\mu}\nabla p\right)\right] = -\left(1-\varepsilon_b\right)\rho_p M_{H_2}\frac{\partial n_a}{\partial t} \tag{2.1}$$

where ε_b is the bed porosity, ρ_g (kg/m^3) is the gaseous hydrogen density, κ (m^2) is the permeability, μ (Pa s) is the dynamic viscosity of hydrogen, and ∇p (Pa/m) is the pressure gradient. The right side of the equation is the mass source term. ρ_p is the particle density of activated carbon, and M_{H_2} is the molecular mass of hydrogen, and n_a is the absolute adsorption amount per unit adsorbent.

The energy equation for the tank can be written as [7, 8]:

$$\left(\rho c_p\right)_{eff} \frac{\partial T}{\partial t} + \rho_g c_{pg} \vec{v} \cdot \nabla T = \nabla \cdot \left(k_{eff} \nabla T\right) + Q \tag{2.2}$$

The left-hand side of Eq. (2.2) includes a transient term and a convection term, and the right-hand side consists of a heat conduction term and a heat source term. The effective heat capacity $\left(\rho c_p\right)_{eff}$ includes the heat capacity of gaseous hydrogen, adsorbed hydrogen and active carbon, and is given by Refs. [7, 8]:

$$\left(\rho c_p\right)_{eff} = \varepsilon_b \rho_g c_{pg} + \rho_b n_a M_{H_2} c_{pa} + \rho_b c_{ps} \tag{2.3}$$

The effective thermal conductivity k_{eff}, can be calculated from the conductivities of hydrogen and of activated carbon and is given as [7, 8]:

$$k_{eff} = \varepsilon_b k_g + \left(1 - \varepsilon_b\right) k_s \tag{2.4}$$

The energy source term Q of Eq. (2.2) consists of adsorption heat source term Q_a and compression heat source term Q_p, which is shown as follows [7, 8]:

$$Q = Q_a + Q_p = \left(1 - \varepsilon_b\right) \rho_p \frac{\partial n_a}{\partial t} \Delta H + \gamma T \left[\varepsilon_b \frac{\partial p}{\partial t} + \left(\vec{v} \cdot \nabla\right) p\right] \tag{2.5}$$

Based on adsorption model, the absolute adsorption amount n_a can be calculated at the pressure p and temperature T. The adsorption model in this work is based on modified Dubinin-Astakhov isotherm, and the absolute adsorption isotherm is given by Refs. [7, 8]:

$$n_a = n_{max} \exp\left[-\left(\frac{RT}{\alpha + \beta T}\right)^m \ln^m\left(\frac{p_0}{p}\right)\right]. \tag{2.6}$$

where n_{max} (mol/kg) is the limiting adsorption and is set as 71.6 mol/kg, m is equal to 2 for most activated carbons. R is the universal gas constant, p is the equilibrium pressure, p_0 is the saturation pressure and is set as 1.47e9 Pa. The parameters α and β represent the enthalpic and the entropic factors, equal to 3080 J/mol and 18.9 J/mol/K, respectively.

2.2 Model parameters

We consider a large-scale hydrogen delivery tank whose volume is about 51.4 m^3, is packed with activated carbon AX-21™. On the whole, the hydrogen storage system includes gaseous and adsorbed hydrogen, activated carbon and steel wall. The effect of gravity on gaseous hydrogen can be ignored. Fig.2.1 shows the geometric model and the mesh of the hydrogen storage tank. The temperature monitor points are presented in Fig.2.1b, and distributed along the axial and radial directions. It took about 25 min to complete the calculation on a computer equipped with an Intel Core i7 CPU and 16G memory. The mesh consists of 9 935 elements, and the number of degrees of freedom of the model is 38 899, as shown in Fig.2.1c. The mesh near the inlet area and steel wall is more compact than any other position. There is a mesh of another model that includes one inlet and one outlet, and it is used for researching the effect of flow-through cooling, as shown in Fig.2.1d. The sizes of the geometry model and the coordinates of monitoring points are given in Table 2.1.

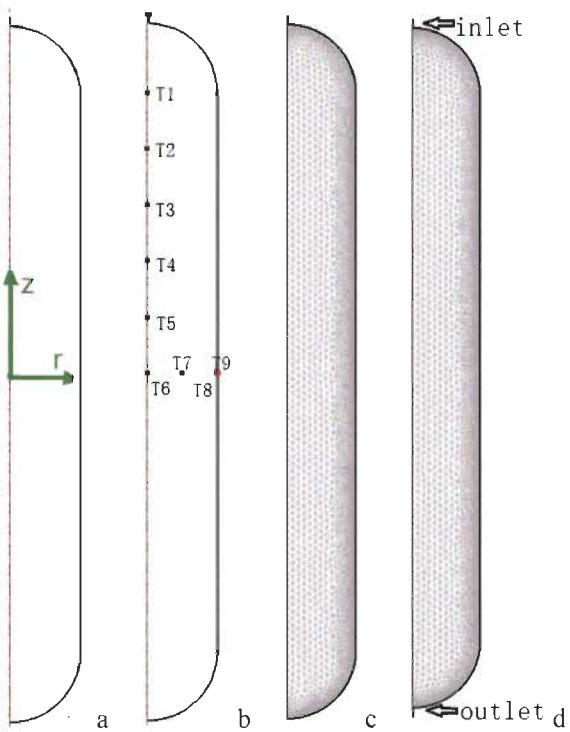

Fig.2.1 Geometric outline (a), temperature monitoring points (b), and finite element meshes of hydrogen tank without outlet (c) and with outlet (d).

The material properties of large-scale hydrogen delivery tank system are given in Table 2.2. The average diameter of activated carbon is equal to 2 mm. As far as this study is concerned, the gaseous hydrogen is modeled using the ideal gas equation of state.

In this work, the initial pressure in the delivery tank is set to 101325 Pa, the initial temperature of the steel wall is set to 298 K, and the initial temperature of materials in the tank including gaseous hydrogen, adsorbed hydrogen and activated carbon are set to 298 K. It is assumed that the adsorptive hydrogen delivery tank is maintained at room temperature environment and the heat transfer coefficient between the outer tank wall and environment is set as 12 W/(m^2 K).

Table 2.1 Geometric parameters and coordinates

Parameter	Value [mm]	Parameter	Value [mm]
Inner radius of tank	1200.15	Point T3	(0,2926.2)
Thickness of tank wall	19.05	Point T4	(0,1950.8)
Length of tank	12192.1	Point T5	(0,975.4)
Inner radius of pipe	19.05	Point T6	(0, 0)
Length of pipe	152.7	Point T7	(600.075 , 0)
Thickness of pipe wall	6.35	Point T8	(1200.15 , 0
Point T1	(0, 4877)	Point T9	(1219.2 , 0)
Point T2	(0, 3901.6)		

Table 2.2 Material properties

	Activated carbon	Hydrogen	Steel wall
Density[kg/m^3]	269	Ideal gas	7830
Specific heat capacity [J/kg K]	825	14700	468
Thermal conductivity [W/m K]	0.764	0.206	13
Porosity	0.49	-	-

2.3 Results and discussions

Based on experiments carried out by the Hydrogen Research Institute of the University of Quebec at Trois-Rivieres, a lab-scale model with a volume of 2.5 L was developed and discussed in our early works [7, 8]. The small hydrogen storage tank was cooled by ice water [7] and liquid nitrogen [8] respectively. The model established in Comsol was validated by comparing the simulation results with the experiment data. The large-scale hydrogen delivery tank with a volume of 51.4 m^3 is unfit for realistic experiments and

measurements. However, the validated model can be extended to simulate a large-scale hydrogen delivery tank. In addition, the large-scale model can be used to study the thermal effects during the charging process and improve the efficiency of hydrogen delivery tanks.

Hydrogen can be viewed from a modeling perspective as existing in the storage tank in the form of an adsorbed phase and a gaseous phase. Fig.2.2a shows the variation of pressure during the charging process and the mass balance of hydrogen in the tank. In this work, the target pressure is set to 10 MPa, the mass flow rate is equal to 10 000 SLPM (about 0.013907 kg/s), and the temperature of hydrogen filling in charging process is set to 298 K. It takes 29 140 s to reach the target pressure. Fig.2.2a also shows the pressure during the filling process, which increases linearly. The parameter m_g represents the mass in the gas phase, the m_a represents the mass of hydrogen adsorbed by activated carbon bed, and the m_t is the total mass of hydrogen present in the tank. The initial mass of hydrogen stored in the tank was 3.2379 kg. The simulation results indicate that the sum of m_a and m_g is equal to m_t. The total mass of hydrogen is approximately equal to 408 kg when the pressure reaches to 10 MPa.

Fig.2.2b shows the evolution of the temperature at different monitor points. The 6 monitor points are located along the axial direction from T1 to T6, and 4 monitor points are located along the radial direction from T6 to T9. The temperature monitor point T8 is placed on the internal steel wall, and T9 close to the outside steel wall. During the charging process, the temperature in the hydrogen storage tank increases as a result of adsorption heat revealed and pressure work. The curves of temperature at T1, T2 and T3 rise quickly in the earlier process, and the changes are relatively tiny in the latter process. The temperature of the area near the inlet is greatly influenced by the filling hydrogen, and the variation of temperature at T5, T6 and some other position along the axial direction trend to be uniform. The curves of temperature at T6 and T7 are broadly similar, but obviously different from those of T8 and T9. In other words, the heat generated in the tank is not transferred effectively to the environment along with radial direction due to the poor thermal conductivity of activated carbon.

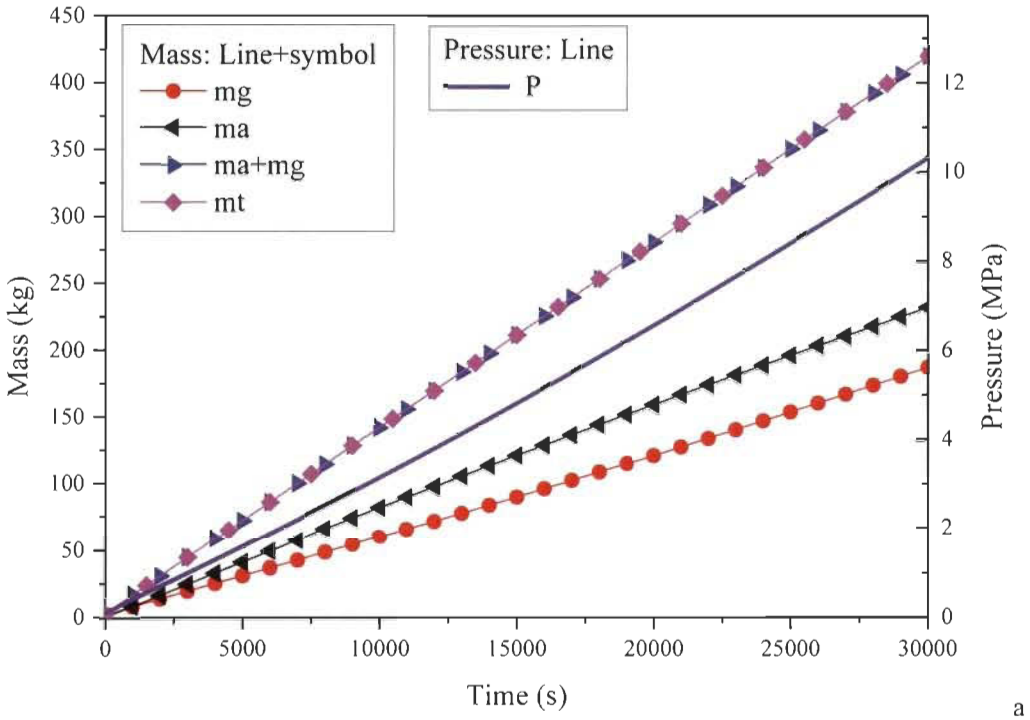

a

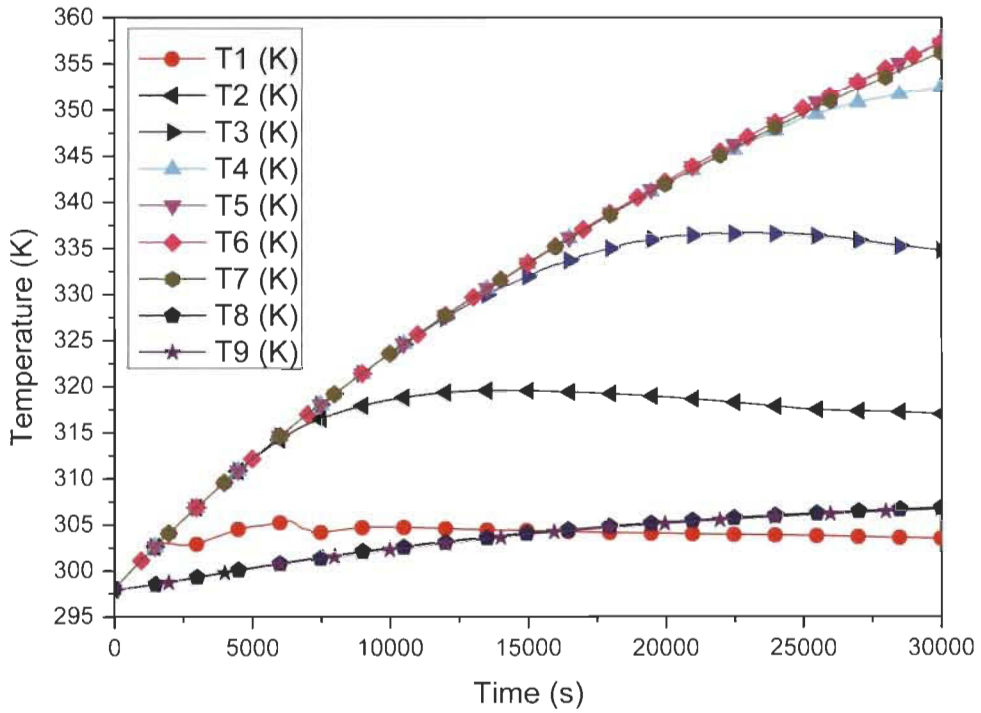

b

Fig.2.2 Verification of hydrogen mass balance and pressure variation (a) and temperature (b) in the tank during the charging process

2.4 Parametric study

2.4.1 Effect of charging flow rate

In order to study the effect of charging flow rates on adsorption, we compare the variations of pressure and temperature at T6 in three cases. The charging flow rates at entrance are 10000 SLPM, 20000 SLPM (about 0.027814 kg/s) and 30000 SLPM (about 0.041721 kg/s) respectively. The filling time in these cases is the same and assumed to be 30000 s. Fig.2.3 shows the curves of pressure and temperature at T6 histories under different charging flow rates. The pressure rises fast with the increase of mass flow rate. However, the temperature at T6 under the mass flow rate of 30 000 SLPM decreases slightly in the latter process because of the cooling effect of filling hydrogen.

2.4.2 Effect of pre-cooling

The feeding hydrogen can be used to cool the activated carbon bed. In this section, the effect of pre-cooling is taken into consideration. And the filling gaseous hydrogen is cooled by ice water before the charging process. The temperature of feeding hydrogen is set to 273 K, and the mass flow rate is equal to 10000 SLPM. Fig.2.4 shows the pressure and mass of hydrogen in the storage tank with and without pre-cooling (a) and temperatures at T1, T3 and T6 with and without pre-cooling (b). The curves of pressure without pre-cooling rise faster than the other with an increase of charging time. When the pressure reaches up to 10MPa, the total mass of hydrogen stored in the tank with pre-cooling is about 7.5 kg more than the other case. The pre-cooling has a great influence on the area near the inlet, and the effect of cooling decreases along the axial direction.

The adsorptive hydrogen storage capacity is mainly dependent on the temperature and the pressure in the tank. For the case of Fig.2.4, the temperature difference caused by pre-cooling (25 K) is small, so the improvement of the pre-cooling on hydrogen storage capacity is only 7.5 kg (~1.8%). In order to validate the effect of pre-cooling on the hydrogen storage capacity, a series of cases with different inlet temperatures are also studied. For the case with a pre-cooling temperature of 225 K, the improvement of the pre-cooling on hydrogen storage capacity is 36.3 kg (~8.9%).

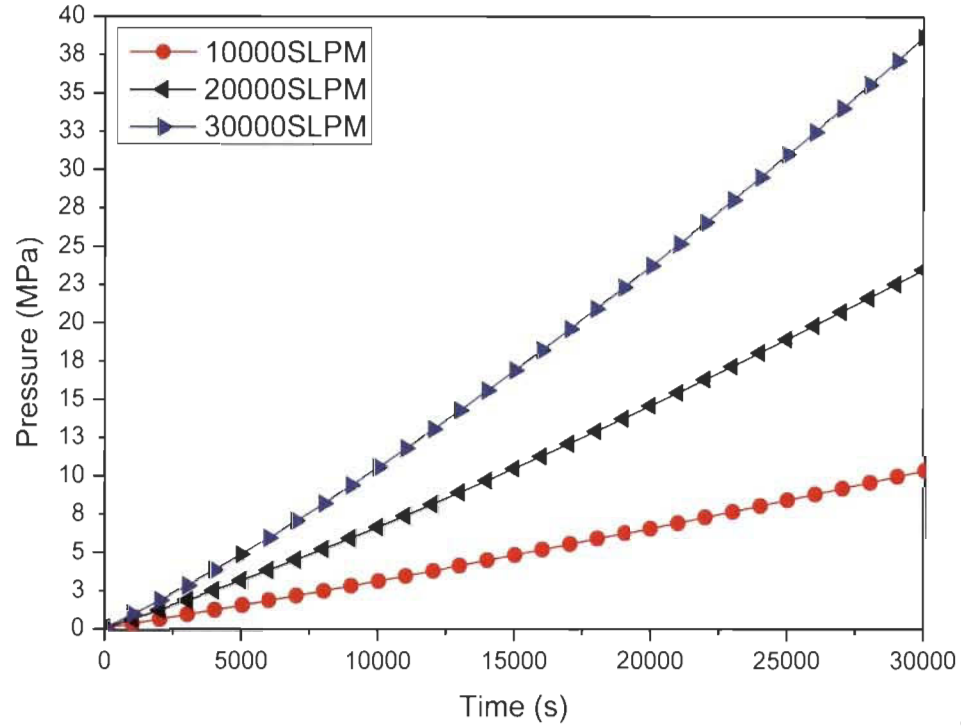

a

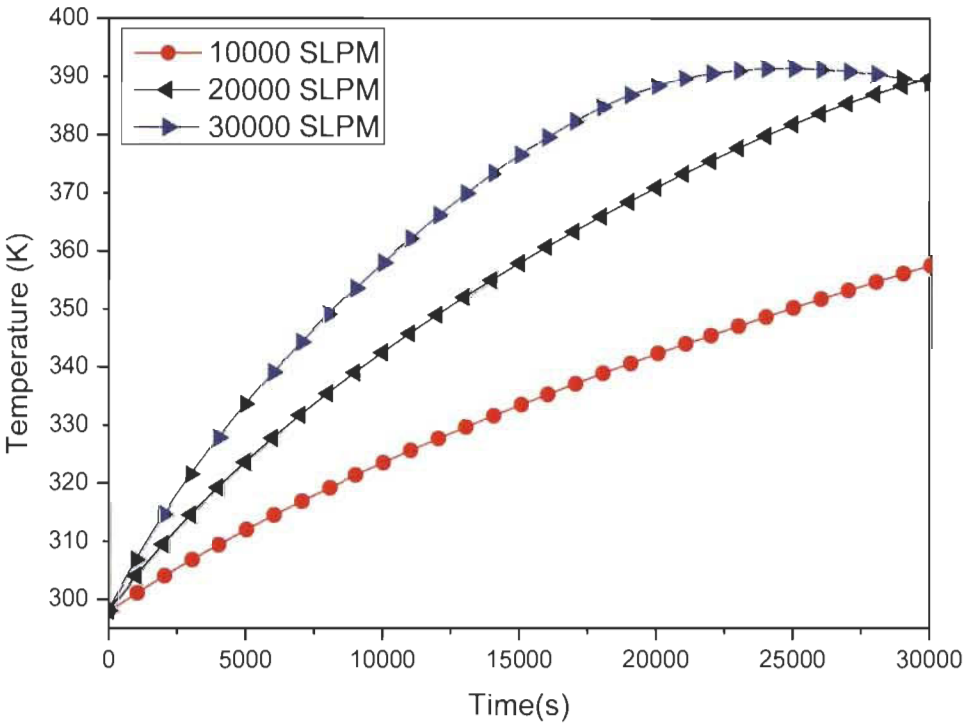

b

Fig.2.3 Pressure (a) and temperature at T6 histories (b) under different charging flow rates

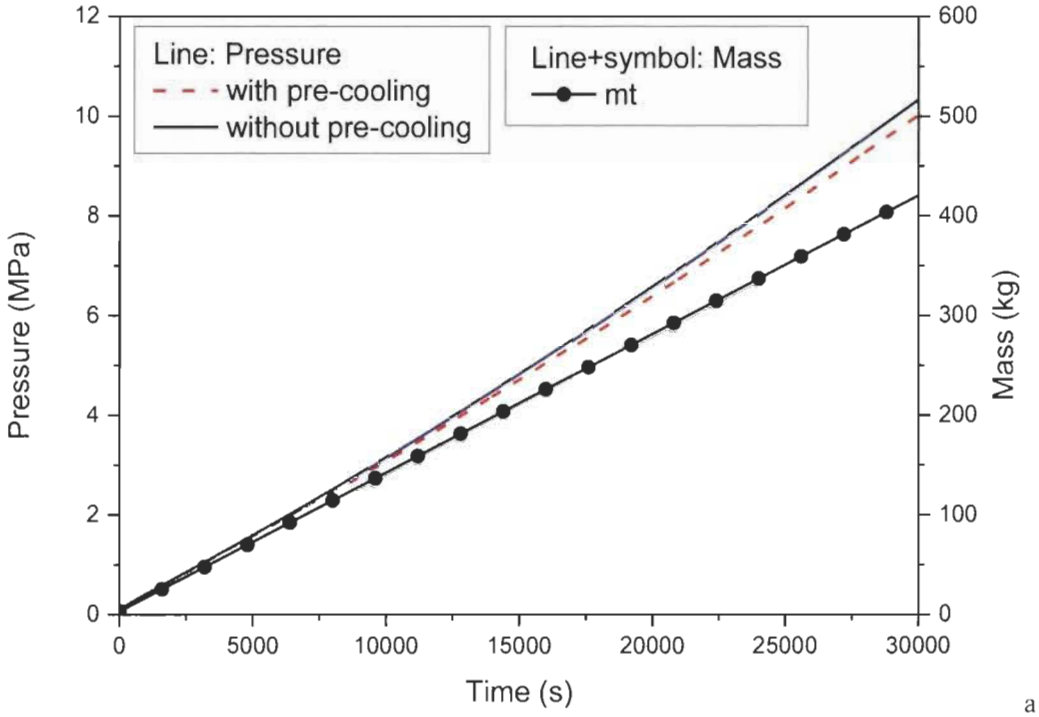

a

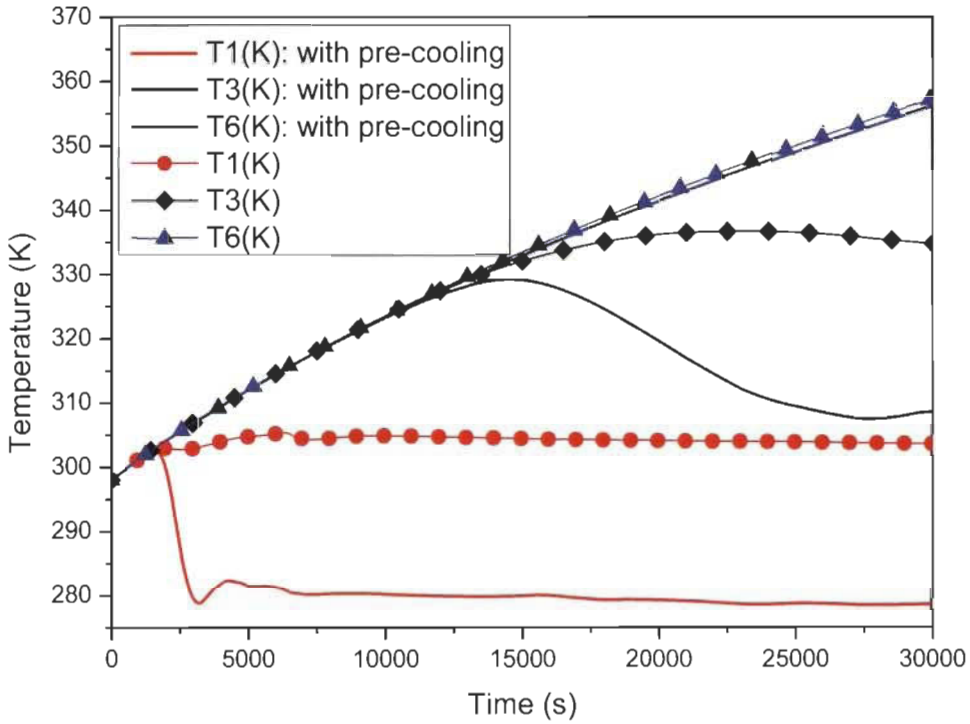

b

Fig.2.4 Pressure and mass of hydrogen in the storage tank with and without pre-cooling (a) and temperature at T1, T3 and T6 with and without pre-cooling (b)

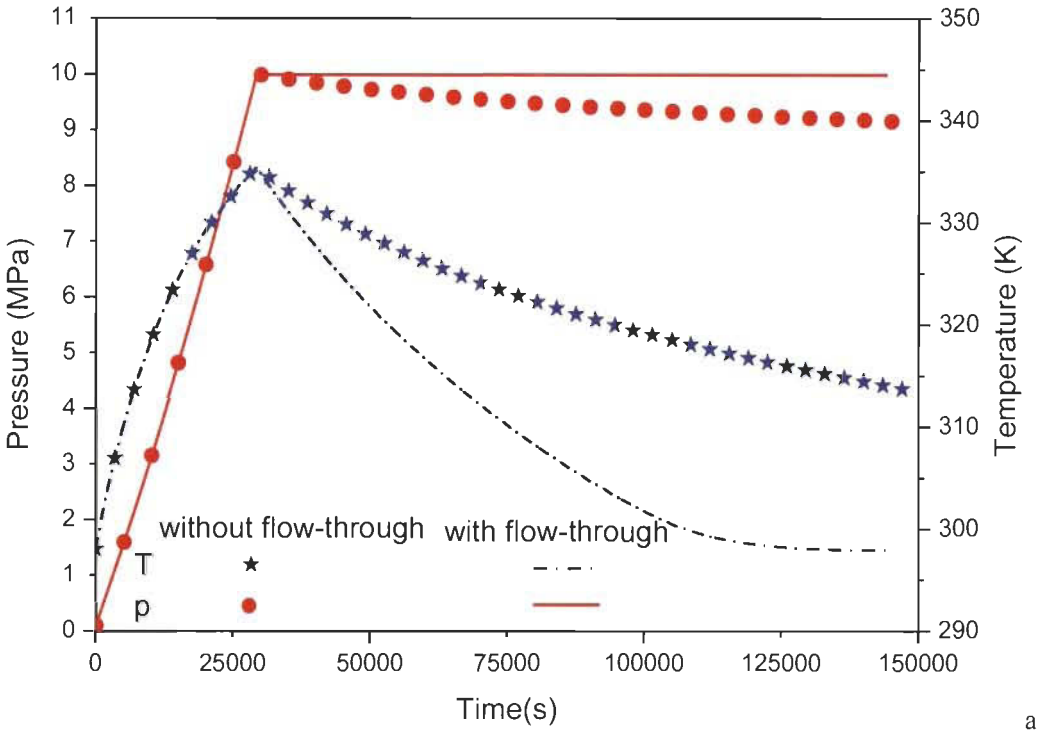

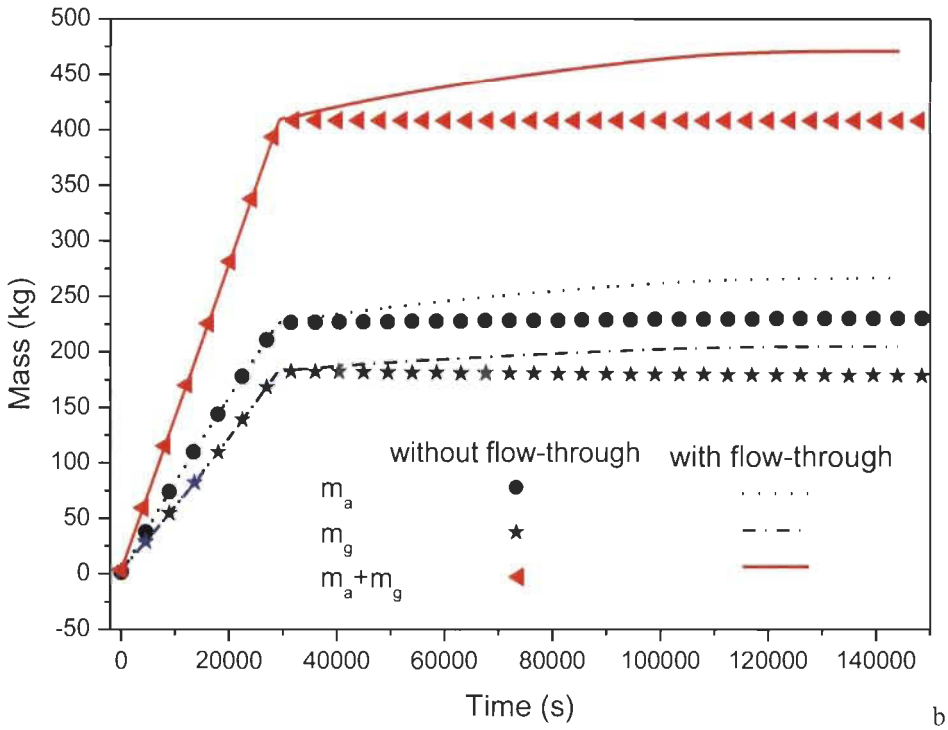

Fig.2.5 Pressure in the storage tank and average temperature variation with and without flow-through cooling (a), and mass of hydrogen in the storage tank with and without flow-through cooling (b)

2.4.3 Effect of flow-through cooling

The effect of flow-through cooling is discussed in this section. The hydrogen storage capacity is dependent on the temperature of activated carbon bed and pressure in the tank. In order to improve the efficiency of hydrogen storage, the temperature of the activated carbon bed can decrease by flow-through cooling after the charging process. Fig.2.1d displays the mesh of hydrogen storage and delivery tank with flow-through cooling, which includes an inlet and an outlet. The outlet is closed during the charging process until the pressure in the tank rises up to 10 MPa. Then, the boundary condition of this outlet is set to flow-through at a constant of 10 MPa. It takes about 114 420 s to decrease the average temperature of the system to about 298 K. And a case without flow-through during dormancy is also taken into consideration for making a comparison.

Fig.2.5a shows the variations of pressure in the storage tank and average temperature variation with and without flow-through cooling. The low-temperature hydrogen cools the activate carbon bed to some degree, and this is a promising way to enhance the hydrogen storage capacity of absorbent. Fig.2.5b presents the mass of hydrogen in the storage tank with and without flow-through cooling. When the temperature in the activated carbon tank decreases to about 298 K, the total mass of hydrogen stored in the tank is approximately equal to 469 kg, which increases about 60 kg (about 15%) than that of the other case without flow-through cooling.

2.4.4 Effect of flow-through cooling with pre-cooling

During the flow-through cooling process, the effects of charging flow rate and pre-cooling are taking into consideration in this section. Fig.2.6 displays the average temperature variation and mass of hydrogen in the storage tank under different conditions with flow-through cooling. It takes a relatively large amount of time to cool the activated carbon bed to 298 K with the charging flow rate of 5000SLPM while there is no obvious improvement of the hydrogen storage capacity. And the pre-cooling of feeding hydrogen during the flow-through process can significantly reduce the cooling time and improve the efficiency of cooling. When the average temperature in the tank reaches 298 K, the hydrogen mass for the case of flow-through cooling combined with

pre-cooling is about 3 kg more than other cases. Furthermore, the difference between these cases will increase with the decrease in average temperature in the tank.

At the same pressure, the lower the temperature, the higher the hydrogen storage capacity. Based on the above analysis, the flow-through cooling combined with pre-cooling can be considered as an effective way to transfer the heat generated and increase the hydrogen storage capacity of the system.

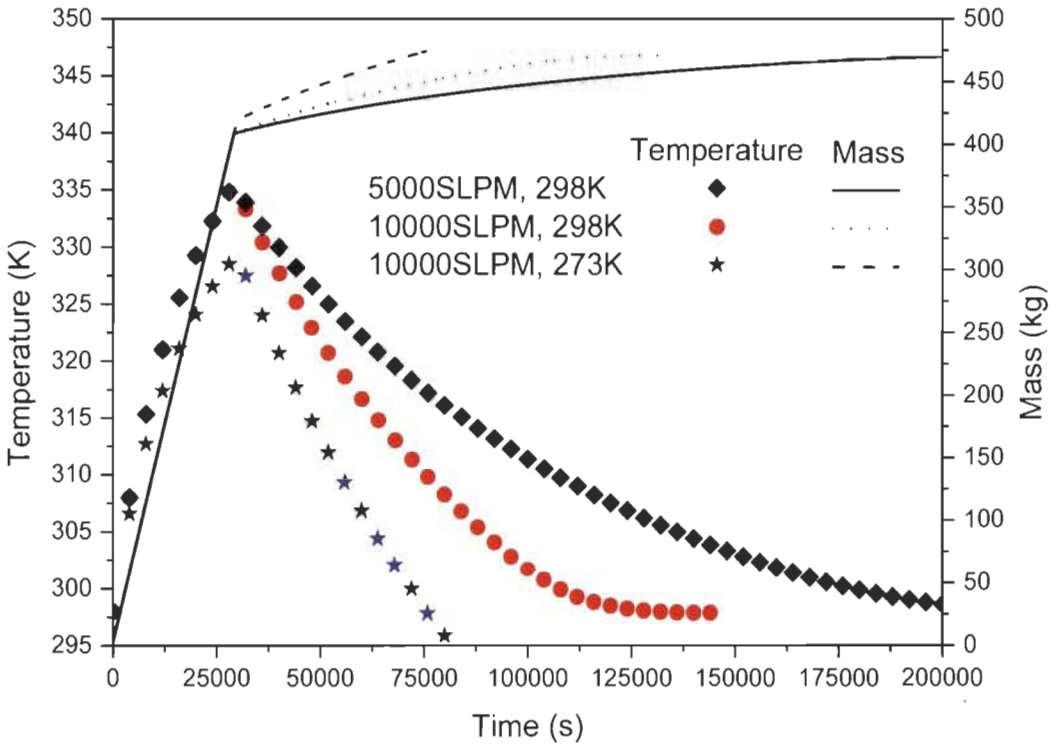

Fig.2.6 Average temperature variation and mass of hydrogen in the tank during flow-through cooling process with pre-cooling and different mass flow rates

2.5 Conclusion

Based on mass, momentum, energy conservation equations and the modified Dubinin-Astakov isotherm, a two-dimensional axisymmetric model is achieved by Comsol. The simulation results show that the temperature of the central position is much higher than those of other regions and the temperature of the front position is obviously lower than that of the rear position during the charging process. The effect of charging flow rate, pre-cooling and flow-through cooling on the filling process has been taken into consideration in order to improve the efficiency of hydrogen storage. The pre-cooling

has a great influence on the temperature near the inlet. The effect of pre-cooling on the hydrogen storage capacity depends on the temperature difference. The method of flow-through cooling is performed, and as a result, it can improve the hydrogen storage capacity by about 15%. The flow-through cooling combined with pre-cooling takes less time to cool adsorbent material than other cases, and can be considered as an effective way to transfer the heat generated during adsorption process and increase the hydrogen storage capacity of the hydrogen delivery tank.

Chapter 3 Thermodynamic analysis for hydrogen storage system using metal hydride

This section has been published in: Xiao J S, Tong L, Bénard P, et al. Thermodynamic analysis for hydriding-dehydriding cycle of metal hydride system. Energy 2019. https://doi.org/10.1016/j.energy.2019.116535.

My specific contributions in this work was to obtain analytical solutions of thermodynamic model for metal hydride system, which can be used as a basic benchmarks to validate numerical models.

In general, a mathematical model can be a lumped parameter model (0-dimensional in space, expressed as an ordinary differential equation on time) or a distributed parameter model (1-, 2- or 3-dimensional in space, expressed as a partial differential equation on time and space), and they can be solved numerically and sometimes analytically. Among them, the lumped parameter model has more possibilities to be solved analytically.

A numerical model is a mathematical model whose solution relies on numerical methods and algorithms, such as the Euler method or Runge-Kutta method for ordinary differential equation (ODE) model, finite difference method or finite element method for partial differential equation (PDE) model. A numerical model, either a lumped parameter model or a distributed parameter model, can be validated by analytical solutions under simplified boundary conditions and material properties. Considering an example of heat conduction of a metal hydride reactor, a distributed parameter model will reduce to a lumped parameter model when a uniform boundary condition and an infinity thermal conductivity is applied to the reactor. From the point of engineering applications, the numerical model should be further validated by experiments.

The analytical solutions are solved from the thermodynamic model based on the principles of mass conservation and energy conservation under certain assumptions of

conditions. Although these analytical solutions are applicable for ideal or theoretical problems only and not for real engineering problems, they are exactly correct under the assumed conditions and they can be used to validate numerical models by comparing the numerical solutions of the numerical models for the same problems with same conditions. Analytical solutions are valid under the assumptions they are obtained and do not need to be validated experimentally,especially since the idealized conditions required for their solution are difficult to reproduce in experiments.

We have developed validated lumped parameter models to study the performances of hydrogen storage and purification systems using metal hydrides [60]. In addition, some thermodynamics models and analytical solutions for the compressed and adsorptive hydrogen storage systems were developed and studied in previous works [13, 14]. The metal hydride hydrogen storage system is based on the hydriding-dehydriding chemical reaction, which is more complicated than the compressed and adsorptive hydrogen storage systems. The analytical solutions for the metal hydride hydrogen storage system are important to understand the hydriding-dehydriding process and the basic theory. The analytical solutions can be considered as a benchmark to validate lumped parameter or distributed parameter numerical models, reducing the need for extensive sets of experimental data required for validation.

In this section, based on the mass and energy balance equations, the thermodynamic analyses for the hydriding-dehydriding cycle of metal hydride hydrogen storage system are carried out for various processes, including hydriding, dormancy and dehydriding processes. The analytical solutions for the metal hydride hydrogen storage system are obtained from the thermodynamic model.

3.1 Thermodynamic model of metal hydride system

The thermodynamic model for the metal hydride hydrogen storage system includes the mass conservation equation, the reaction kinetics equation, the equilibrium pressure equation, the energy conservation equation, and the equation of state for ideal gas, as shown below. The source terms of metal hydride in the mass conservation equations are related to the reaction kinetics equation and the equilibrium pressure equation.

3.1.1 Mass balance

The alloy $LaNi_5$ is selected as the material for hydrogen storage in this work. The hydriding-dehydriding reaction equation can be written as $LaNi_5 + 3H_2 \leftrightarrow LaNi_5H_6 + Q$. There are generally gaseous hydrogen and solid materials in the metal hydride hydrogen storage reactor. The solid materials include the alloy $LaNi_5$ and the metal hydride $LaNi_5H_6$ in this reactor, as presented in Eq.(3.1). The mass of alloy m_M decreases and the mass of metal hydride m_{MH} increases during hydriding. In contrast, the alloy mass m_M increases and the metal hydride mass m_{MH} decreases during dehydriding. As a whole, the solid mass m_s increases during hydriding and decreases during dehydriding.

$$m_s = m_M + m_{MH} \tag{3.1}$$

The saturated mass of solid materials is defined as m_s^{sat}. When the whole alloy is completely reacted with hydrogen, the metal hydride mass reaches its maximal value m_{MH}^{max}.

$$m_s^{sat} = 0 + m_{MH}^{max} \tag{3.2}$$

The solid mass also can be written as the sum of the initial mass $(m_{0M} + m_{0H})$ and the hydrogen mass absorbed into the metal hydride , as described in Eq.(3.3). m_{0M} and m_{0H} mean the initial alloy mass and the initial adsorbed hydrogen mass, respectively. When there is only alloy in the solid materials at the initial state, the mass of adsorbed hydrogen m_{0H} can be set as 0. Of course, the initial mass $(m_{0M} + m_{0H})$ can be considered to be constant, and the mass of absorbed hydrogen m_H is variable, which increases during hydriding and decreases during dehydriding.

$$m_s = m_{0M} + m_{0H} + m_H \tag{3.3}$$

The saturated mass of solid materials also can be presented as the sum of the initial alloy mass m_{0M} and the maximal value of absorbed hydrogen mass m_H^{max}, shown as

follows:

$$m_s^{sat} = m_{0M} + m_H^{max} \tag{3.4}$$

The relationship between the mass of absorbed hydrogen m_H and the mass of metal hydride m_{MH} is presented as:

$$m_H = m_{MH} \psi M_{H_2} / M_{MH} \tag{3.5}$$

where the alphabet ψ is defined as the stoichiometric coefficient of hydrogen per metal hydride. M_{MH} and M_{H_2} are the molecular weight of metal hydride and hydrogen, respectively.

A general form of mass balance equation for a lumped parameter model can be expressed as:

$$\frac{dm}{dt} = \dot{m} + \dot{S} \tag{3.6}$$

where $\dot{m}$ is the net mass flow rate and $\dot{S}$ is the net mass generation rate or the mass source term. The mass balance equation can be used for metal hydride, gaseous hydrogen and solid materials in the metal hydride hydrogen storage system.

$$\frac{dm_{MH}}{dt} = \dot{S}_{MH} \tag{3.7}$$

$$\frac{dm_{H_2}}{dt} = \dot{m}_{H_2} + \dot{S}_{H_2} \tag{3.8}$$

$$\frac{dm_s}{dt} = -\dot{S}_{H_2} \tag{3.9}$$

The mass source term of metal hydride $\dot{S}_{MH}$ is a positive quantity during absorption and negative quantity during desorption. As for the gaseous hydrogen in the reactor, the mass source term $\dot{S}_{H_2}$ is a negative quantity during absorption and is a positive quantity during desorption. The hydrogen mass flow rate $\dot{m}_{H_2}$ is equal to the difference between the mass inflow rate $\dot{m}_{H_2in}$ and the mass outflow rate $\dot{m}_{H_2out}$, and the subscript in/out refers to the inflow/outflow stage. We assume that $\dot{m}_{H_2out} = 0$ during hydriding

and $\dot{m}_{\mathrm{H_2in}} = 0$ during dehydriding.

The relational expression between the metal hydride mass source term $\dot{S}_{\mathrm{MH}}$ and the hydrogen mass source term $\dot{S}_{\mathrm{H_2}}$ can be written as $\dot{S}_{\mathrm{MH}} = -\dot{S}_{\mathrm{H_2}} M_{\mathrm{MH}} / \left(\psi M_{\mathrm{H_2}}\right)$. The mass source term of the metal hydride is related to the reaction kinetics equation of metal hydride and the equilibrium pressure equation.

3.1.2 Reaction kinetics and equilibrium pressure

During absorption and desorption, the mass source terms of metal hydride can be written as:

$$\dot{S}_{\mathrm{MH}} = C_a \mathrm{e}^{-E_a/(RT)} \ln\left(p_{\mathrm{H_2}} / p_{\mathrm{eq}a}\right)\left(m_{\mathrm{s}}^{\mathrm{sat}} - m_{\mathrm{MH}}\right), \text{ for } p_{\mathrm{H_2}} > p_{\mathrm{eq}a} \tag{3.10a}$$

$$\dot{S}_{\mathrm{MH}} = C_d \mathrm{e}^{-E_d/(RT)} \left[\left(p_{\mathrm{H_2}} - p_{\mathrm{eq}d}\right) / p_{\mathrm{eq}d}\right] m_{\mathrm{MH}}, \text{ for } p_{\mathrm{H_2}} < p_{\mathrm{eq}d} \tag{3.10b}$$

where $m_{\mathrm{s}}^{\mathrm{sat}}$ is the saturated mass of solid materials and it is equal to $m_{\mathrm{MH}}^{\max}$. E means the activated energy, and the subscript a/d refers to the absorption/desorption stage. The hydrogen pressure $p_{\mathrm{H_2}}$ is above the equilibrium pressure $p_{\mathrm{eq}a}$ during hydriding and below the equilibrium pressure $p_{\mathrm{eq}d}$ during dehydriding. The mass source term of metal hydride $\dot{S}_{\mathrm{MH}}$ is set as 0 when $p_{\mathrm{H_2}}$ is between $p_{\mathrm{eq}a}$ and $p_{\mathrm{eq}d}$. Based on Eqs. (3.10a) and (3.10b), the mass source term of metal hydride $\dot{S}_{\mathrm{MH}}$ is a positive quantity and the metal hydride mass m_{MH} increases during hydriding, whereas $\dot{S}_{\mathrm{MH}}$ is a negative quantity and m_{MH} decreases during dehydriding.

The equilibrium pressure $p_{\mathrm{eq}a/d}$ is presented as:

$$\ln\left(\frac{p_{\mathrm{eq}a/d}}{p_0}\right) = -\frac{\Delta H_{a/d}}{RT} + \frac{\Delta S_{a/d}}{R} + k_{\mathrm{p}}\left(\frac{m_{\mathrm{MH}}}{m_{\mathrm{s}}^{\mathrm{sat}}} - \frac{1}{2}\right) \tag{3.11}$$

where the reference pressure p_0 is set as 0.1 MPa. The reaction enthalpy ΔH and the reaction entropy ΔS are set as positive quantities in this work. The symbol k_{p} is the plateau slope coefficient.

3.1.3 Energy balance

The heat exchangers can be used to improve the heat transfer efficiency of the metal hydride reactor. For simplification, the metal hydride reactor without a heat exchanger is studied in this section. The wall of the metal hydride reactor is ignored. The energy balance equation of the metal hydride hydrogen storage system is shown as:

$$\frac{\mathrm{d}\left(m_{\mathrm{H_2}}c_v T + m_{\mathrm{s}}c_{\mathrm{s}}T\right)}{\mathrm{d}t} = \dot{m}_{\mathrm{H_2}}c_p T_\infty + a_f A_{\mathrm{s}}\left(T_f - T\right) - \frac{\dot{S}_{\mathrm{H_2}}\Delta H_{a/d}}{M_{\mathrm{H_2}}} \tag{3.12}$$

where $m_{\mathrm{H_2}}$ means the mass of gaseous hydrogen in metal hydride reactor, c_{s} is the specific heats of solid material; T_∞ is the inflow or outflow temperature; a_f is the heat transfer coefficient; A_{s} is the surface area of the reactor; the ambient temperature T_f is set as the cooling/heating water temperature. The left term of Eq. (3.12) means the rate of internal energy of the metal hydride reactor. Based on Eqs. (3.8) and (3.9), the left term can be transformed as $\left(m_{\mathrm{H_2}}c_v + m_{\mathrm{s}}c_{\mathrm{s}}\right)\mathrm{d}T/\mathrm{d}t + c_v T\left(\dot{m}_{\mathrm{H_2}} + \dot{S}_{\mathrm{H_2}}\right) - c_{\mathrm{s}}T\dot{S}_{\mathrm{H_2}}$. The effects of the enthalpy change caused by the inflow/outflow hydrogen, the heat transfer between the ambient environment and the metal hydride reactor, and the reaction heat on the metal hydride hydrogen storage system are taken into consideration in the right terms of Eq. (3.12). The heat source term is written as $\dot{S}_{\mathrm{MH}}\Delta H_{a/d}\Psi_{\mathrm{H_2}}/M_{\mathrm{MH}}$ or $-\dot{S}_{\mathrm{H_2}}\Delta H_{a/d}/M_{\mathrm{H_2}}$, and it is positive during absorption and negative during desorption. The energy conservation equation of this system is transformed as:

$$\begin{aligned}&\left(m_{\mathrm{H_2}}c_v + m_{\mathrm{s}}c_{\mathrm{s}}\right)\frac{\mathrm{d}T}{\mathrm{d}t} = \\ &\dot{m}_{\mathrm{H_2}}\left(c_p T_\infty - c_{\mathrm{v}}T\right) + a_f A_{\mathrm{s}}\left(T_f - T\right) - \dot{S}_{\mathrm{H_2}}\left[\left(c_v - c_{\mathrm{s}}\right)T + \Delta H_{a/d}/M_{\mathrm{H_2}}\right]\end{aligned} \tag{3.13}$$

3.1.4 Equation of state for hydrogen gas

Geseous hydrogen gas in the metal hydride reactor is considered as the ideal gas:

$$m_{\mathrm{H_2}} = p_{\mathrm{H_2}}V_{\mathrm{g}}M_{\mathrm{H_2}}/\left(RT\right) \tag{3.14}$$

where $p_{\mathrm{H_2}}$ is the hydrogen pressure; V_{g} is the volume for the gas phase in the metal

hydride reactor; R is the universal gas constant, it is set as 8.314 J/mol/K.

3.2 Analytical solutions of the thermodynamic model

The analytical solutions can be solved from the above thermodynamic model for the metal hydride hydrogen storage system. The mass flow rate can be set as constant through a mass flow controller in the experiment. When the mass flow rate is fixed, the reaction rate of metal hydride is almost constant [52] . Therefore, we can assume that the associated mass source terms in the mass balance equations of the metal hydride and hydrogen are constant. The variable reaction rate has been considered into the lumped parameter model in the following section, whose value is proved to be approximately constant. In this section, the reaction rate is assumed as constant in order to solve the analytical solutions for the lumped temperature of the metal hydride reactor. The mass source term is set as constant. The analytical solutions are discussed during hydriding, dormancy and dehydriding processes in various conditions, where the inflow/outflow temperature T_∞ is considered to be constant or variable in the analytical solutions.

Table 3.1 Definitions of parameters used in analytical solutions

	Constant inflow/outflow temperature	Variable inflow/outflow temperature	Dormancy process
α	$a_f A_s / \left(\dot{m}_{H_2} c_v\right)$		-
γ	c_p / c_v		-
t^*	$\frac{m_{0H_2} c_v + m_{0M} c_s + m_{0H} c_s}{\dot{m}_{H_2} c_v + \dot{S}_{H_2} c_v - \dot{S}_{H_2} c_s}$		$\frac{m_{0H_2} c_v + m_{0M} c_s + m_{0H} c_s}{a_f A_s}$
β	$\dot{S}_{H_2} / \dot{m}_{H_2}$		-
$T_{a/d}$	$-\beta \Delta H_{a/d} / \left(M_{H_2} c_v\right)$		-
τ		t / t^*	
T^*	$\frac{\gamma T_\infty + \alpha T_f + T_{a/d}}{\alpha + 1 + \beta - \beta c_s / c_v}$	$\frac{\alpha T_f + T_{a/d}}{\alpha - \gamma + 1 + \beta - \beta c_s / c_v}$	T_f

3.2.1 Constant inflow/outflow temperature during hydriding/dehydriding processes

The inflow/outflow temperature T_∞ is assumed to be constant. Considering the mass flow rate and the mass source term are set as constants, Eqs. (3.8) and (3.9) can be transformed as $m_{\mathrm{H}_2} = m_{0\mathrm{H}_2} + \left(\dot{m}_{\mathrm{H}_2} + \dot{S}_{\mathrm{H}_2}\right)t$ and $m_{\mathrm{s}} = m_{0\mathrm{M}} + m_{0\mathrm{H}} - \dot{S}_{\mathrm{H}_2}t$, respectively. So Eq. (3.13) becomes:

$$\begin{aligned}&\left[m_{0\mathrm{H}_2}c_v + m_{0\mathrm{M}}c_{\mathrm{s}} + m_{0\mathrm{H}}c_{\mathrm{s}} + \left(\dot{m}_{\mathrm{H}_2}c_v + \dot{S}_{\mathrm{H}_2}c_v - \dot{S}_{\mathrm{H}_2}c_{\mathrm{s}}\right)t\right]\frac{\mathrm{d}T}{\mathrm{d}t} = \\ &\dot{m}_{\mathrm{H}_2}c_pT_\infty + a_fA_{\mathrm{s}}T_f - \frac{\dot{S}_{\mathrm{H}_2}\Delta H_{a/d}}{M_{\mathrm{H}_2}} - T\left(a_fA_{\mathrm{s}} + \dot{m}_{\mathrm{H}_2}c_v + \dot{S}_{\mathrm{H}_2}c_v - \dot{S}_{\mathrm{H}_2}c_{\mathrm{s}}\right)\end{aligned} \tag{3.15}$$

Divided by $\dot{m}_{\mathrm{H}_2}c_v + \dot{S}_{\mathrm{H}_2}c_v - \dot{S}_{\mathrm{H}_2}c_{\mathrm{s}}$, Eq. (3.15) is transformed as:

$$\begin{aligned}&\left(\frac{m_{0\mathrm{H}_2}c_v + m_{0\mathrm{M}}c_{\mathrm{s}} + m_{0\mathrm{H}}c_{\mathrm{s}}}{\dot{m}_{\mathrm{H}_2}c_v + \dot{S}_{\mathrm{H}_2}c_v - \dot{S}_{\mathrm{H}_2}c_{\mathrm{s}}} + t\right)\frac{\mathrm{d}T}{\mathrm{d}t} = \\ &\frac{\dot{m}_{\mathrm{H}_2}c_pT_\infty + a_fA_{\mathrm{s}}T_f - \dot{S}_{\mathrm{H}_2}\Delta H_{a/d}/M_{\mathrm{H}_2} - T\left(a_fA_{\mathrm{s}} + \dot{m}_{\mathrm{H}_2}c_v + \dot{S}_{\mathrm{H}_2}c_v - \dot{S}_{\mathrm{H}_2}c_{\mathrm{s}}\right)}{\dot{m}_{\mathrm{H}_2}c_v + \dot{S}_{\mathrm{H}_2}c_v - \dot{S}_{\mathrm{H}_2}c_{\mathrm{s}}}\end{aligned} \tag{3.16}$$

The characteristic time t^* is assumed as $\left(m_{0\mathrm{H}_2}c_v + m_{0\mathrm{M}}c_{\mathrm{s}} + m_{0\mathrm{H}}c_{\mathrm{s}}\right)/\left(\dot{m}_{\mathrm{H}_2}c_v + \dot{S}_{\mathrm{H}_2}c_v - \dot{S}_{\mathrm{H}_2}c_{\mathrm{s}}\right)$, $\gamma = c_p/c_v$, $\beta = \dot{S}_{\mathrm{H}_2}/\dot{m}_{\mathrm{H}_2}$, $\alpha = a_fA_{\mathrm{s}}/\left(\dot{m}_{\mathrm{H}_2}c_v\right)$ and $T_{a/d} = -\beta\Delta H_{a/d}/\left(M_{\mathrm{H}_2}c_v\right)$. Extracting $\dot{m}_{\mathrm{H}_2}c_v$ in the right term of Eq. (3.16), the energy equation becomes:

$$\begin{aligned}&\left(t^* + t\right)\frac{\mathrm{d}T}{\mathrm{d}t} = \\ &\left[\gamma T_\infty + \alpha T_f + T_{a/d} - T\left(\alpha + 1 + \beta - \frac{\beta c_{\mathrm{s}}}{c_v}\right)\right]\dot{m}_{\mathrm{H}_2}c_v/\left(\dot{m}_{\mathrm{H}_2}c_v + \dot{S}_{\mathrm{H}_2}c_v - \dot{S}_{\mathrm{H}_2}c_{\mathrm{s}}\right)\end{aligned} \tag{3.17}$$

Defining $T^* = \left(\gamma T_\infty + \alpha T_f + T_{a/d}\right)/\left(\alpha + 1 + \beta - \beta c_{\mathrm{s}}/c_v\right)$, reducing $\dot{m}_{\mathrm{H}_2}c_v$ and $1 + \beta - \beta c_{\mathrm{s}}/c_v$ in the right term of Eq. (3.17), then the above equation is simplified as:

$$\left(t^* + t\right)\frac{\mathrm{d}T}{\mathrm{d}t} = \left(1 + \frac{\alpha}{1 + \beta - \beta c_{\mathrm{s}}/c_v}\right)\left(T^* - T\right) \tag{3.18}$$

Solving Eq. (3.18), using $\tau = t/t^*$, we obtain

$$\frac{T^* - T}{T^* - T_0} = \left(\frac{1}{1+\tau}\right)^{1+\alpha/(1+\beta-\beta c_s/c_v)} \tag{3.19}$$

$$\text{or } T = T^* - \frac{T^* - T_0}{(1+\tau)^{[1+\alpha/(1+\beta-\beta c_s/c_v)]}} \tag{3.20}$$

3.2.2 Variable inflow/outflow temperature during hydriding/dehydriding processes

The inflow/outflow temperature T_∞ is set as a variable in this section, so the energy balance equation is presented as:

$$\begin{aligned}&\left[m_{0\mathrm{H}_2}c_v + m_{0\mathrm{M}}c_s + m_{0\mathrm{H}}c_s + \left(\dot{m}_{\mathrm{H}_2}c_v + \dot{S}_{\mathrm{H}_2}c_v - \dot{S}_{\mathrm{H}_2}c_s\right)t\right]\frac{\mathrm{d}T}{\mathrm{d}t} = \\ &\left(\dot{m}_{\mathrm{H}_2}c_p - \dot{m}_{\mathrm{H}_2}c_v - \dot{S}_{\mathrm{H}_2}c_v + \dot{S}_{\mathrm{H}_2}c_s - a_f A_s\right)T + a_f A_s T_f - \dot{S}_{\mathrm{H}_2}\Delta H_{a/d}/M_{\mathrm{H}_2}\end{aligned} \tag{3.21}$$

Divided by $\dot{m}_{\mathrm{H}_2}c_v + \dot{S}_{\mathrm{H}_2}c_v - \dot{S}_{\mathrm{H}_2}c_s$, then Eq.(3.21) becomes:

$$\begin{aligned}&\left(\frac{m_{0\mathrm{H}_2}c_v + m_{0\mathrm{M}}c_s + m_{0\mathrm{H}}c_s}{\dot{m}_{\mathrm{H}_2}c_v + \dot{S}_{\mathrm{H}_2}c_v - \dot{S}_{\mathrm{H}_2}c_s} + t\right)\frac{\mathrm{d}T}{\mathrm{d}t} = \\ &\frac{\left(\dot{m}_{\mathrm{H}_2}c_p - \dot{m}_{\mathrm{H}_2}c_v - \dot{S}_{\mathrm{H}_2}c_v + \dot{S}_{\mathrm{H}_2}c_s - a_f A_s\right)T + a_f A_s T_f - \dot{S}_{\mathrm{H}_2}\Delta H_{a/d}/M_{\mathrm{H}_2}}{\dot{m}_{\mathrm{H}_2}c_v + \dot{S}_{\mathrm{H}_2}c_v - \dot{S}_{\mathrm{H}_2}c_s}\end{aligned} \tag{3.22}$$

The characteristic time t^*, the dimensionless heat transfer coefficient α, the absorption/desorption contributed temperature $T_{a/d}$, the specific heat ratio γ and the ratio of hydrogen mass source term to mass flow rate β are defined in the former section. Extracting $\dot{m}_{\mathrm{H}_2}c_v$ in the right term of Eq. (3.22), then the above equation becomes:

$$\begin{aligned}&\left(t^* + t\right)\frac{\mathrm{d}T}{\mathrm{d}t} = \\ &\left[\left(\gamma - 1 - \beta + \beta c_s/c_v - \alpha\right)T + \alpha T_f + T_{a/d}\right]\dot{m}_{\mathrm{H}_2}c_v / \left(\dot{m}_{\mathrm{H}_2}c_v + \dot{S}_{\mathrm{H}_2}c_v - \dot{S}_{\mathrm{H}_2}c_s\right)\end{aligned} \tag{3.23}$$

Reducing $\dot{m}_{\mathrm{H}_2}c_v$ and $1+\beta-\beta c_s/c_v$, Eq. (3.23) is simplified as:

$$\left(t^{*}+t\right)\frac{\mathrm{d}T}{\mathrm{d}t}=\left(1+\frac{\alpha-\gamma}{1+\beta-\beta c_{\mathrm{s}}/c_{v}}\right)\left(T^{*}-T\right) \tag{3.24}$$

where the characteristic temperature $T^{*}=\left(\alpha T_{f}+T_{a/d}\right)/\left(\alpha-\gamma+1+\beta-\beta c_{\mathrm{s}}/c_{v}\right)$.

Defining $\tau=t/t^{*}$, the solution of Eq.(3.24) is obtained as

$$\frac{T^{*}-T}{T^{*}-T_{0}}=\left(\frac{1}{1+\tau}\right)^{1+(\alpha-\gamma)/(1+\beta-\beta c_{\mathrm{s}}/c_{v})} \tag{3.25}$$

or $T=T^{*}-\left(T^{*}-T_{0}\right)/\left(1+\tau\right)^{[1+(\alpha-\gamma)/(\beta+1-\beta c_{\mathrm{s}}/c_{v})]}$ (3.26)

3.2.3 Temperature during dormancy process

The mass flow rate $\dot{m}_{\mathrm{H_2}}$ is set as 0, and the source terms, including $\dot{S}_{\mathrm{H_2}}$ and $\dot{S}_{\mathrm{MH}}$, are neglected during dormancy. The energy balance equation, which only takes the heat transfer between metal hydride reactor and ambient environment into consideration, is written as:

$$\left(m_{0\mathrm{H_2}}c_{v}+m_{0\mathrm{M}}c_{\mathrm{s}}+m_{0\mathrm{H}}c_{\mathrm{s}}\right)\mathrm{d}T/\mathrm{d}t=a_{f}A_{\mathrm{s}}\left(T_{f}-T\right) \tag{3.27}$$

We assume that the characteristic time $t^{*}=\left(m_{0\mathrm{H_2}}c_{v}+m_{0\mathrm{M}}c_{\mathrm{s}}+m_{0\mathrm{H}}c_{\mathrm{s}}\right)/\left(a_{f}A_{\mathrm{s}}\right)$, and the characteristic temperature $T^{*}=T_{f}$. Then Eq. (3.27) becomes,

$$\mathrm{d}T/\mathrm{d}t=\left(T^{*}-T\right)/t^{*} \tag{3.28}$$

Solving Eq. (3.28), using $\tau=t/t^{*}$, we get:

$$T=T^{*}-\left(T^{*}-T_{0}\right)\exp\left(-\tau\right) \tag{3.29}$$

3.3 Application of analytical solutions

The analytical solutions can be considered as a reference to validate the numerical model. In this section, the numerical solutions of the lumped parameter model with constant mass source term are compared with the analytical solutions. Various analytical solutions using different inflow/outflow temperature are discussed. The

analytical solution in the present work is compared with the reduced model proposed in the reference.

3.3.1 Description of hydrogen storage system

Based on a metal hydride reactor compacted with $LaNi_5$, the above analytical solutions are used to validate a numerical model. The numerical model is the lumped parameter thermodynamic model or the zero-dimensional model, which is developed on the Matlab/Simulink platform. There are three stages in a hydriding-dehydriding cycle, including absorption, dormancy and desorption processes. The metal hydride reactor is cooled by circulating water during the absorption process, and heated in the dormancy and desorption stages. The lumped temperature of the metal hydride reactor during dormancy increases since the reactor is heated by the circulating water, and relatively high temperature in metal hydride reactor is good for the dehydriding reaction. Talaganis et al. have simulated absorption-desorption cyclic processes and presented detailed parameters in their cases. The total alloy mass m_{0M} is 109.3 kg, and we suppose that a section of the alloy (23kg) has been transformed as metal hydride at the beginning in our case. The parameters used in our model are obtained from Ref.[52], as shown in Table 3.2.

3.3.2 Validation of numerical model by analytical solution

A lumped parameter model can be solved numerically and sometimes analytically. The analytical solution can be considered as a simple benchmark to validate the lumped parameter numerical model. For simplification, the hydrogen mass source term $\dot{S}_{H_2}$ in each stage is set as constant in the numerical model and the analytical solution.The mass flow rate used in the present work refers to that in Case 2 from Ref.[52] in order to maintain a hydrogen production of 2 kg_{H2}/h. The time of an absorption-desorption cycle in Case 2 [52] is 3600s. The hydrogen is produced during desorption (about 720s), and the mass outflow rate is about 1.389g/s in the dehydriding process. The absolute values of the mass flow rate and the hydrogen mass source term are both assumed as 1.389 g/s during hydriding and dehydriding. The ratio of the hydrogen mass source term to the mass flow rate is assumed as -1. The hydriding/dehydriding reaction is

ignored during dormancy. The mass flow rate is a positive quantity and the hydrogen mass source term is a negative quantity during hydriding. On the contrary, the mass flow rate is a negative quantity and the hydrogen mass source term is a positive quantity during dehydriding. The inflow temperature is assumed as constant while the outflow temperature is variable.

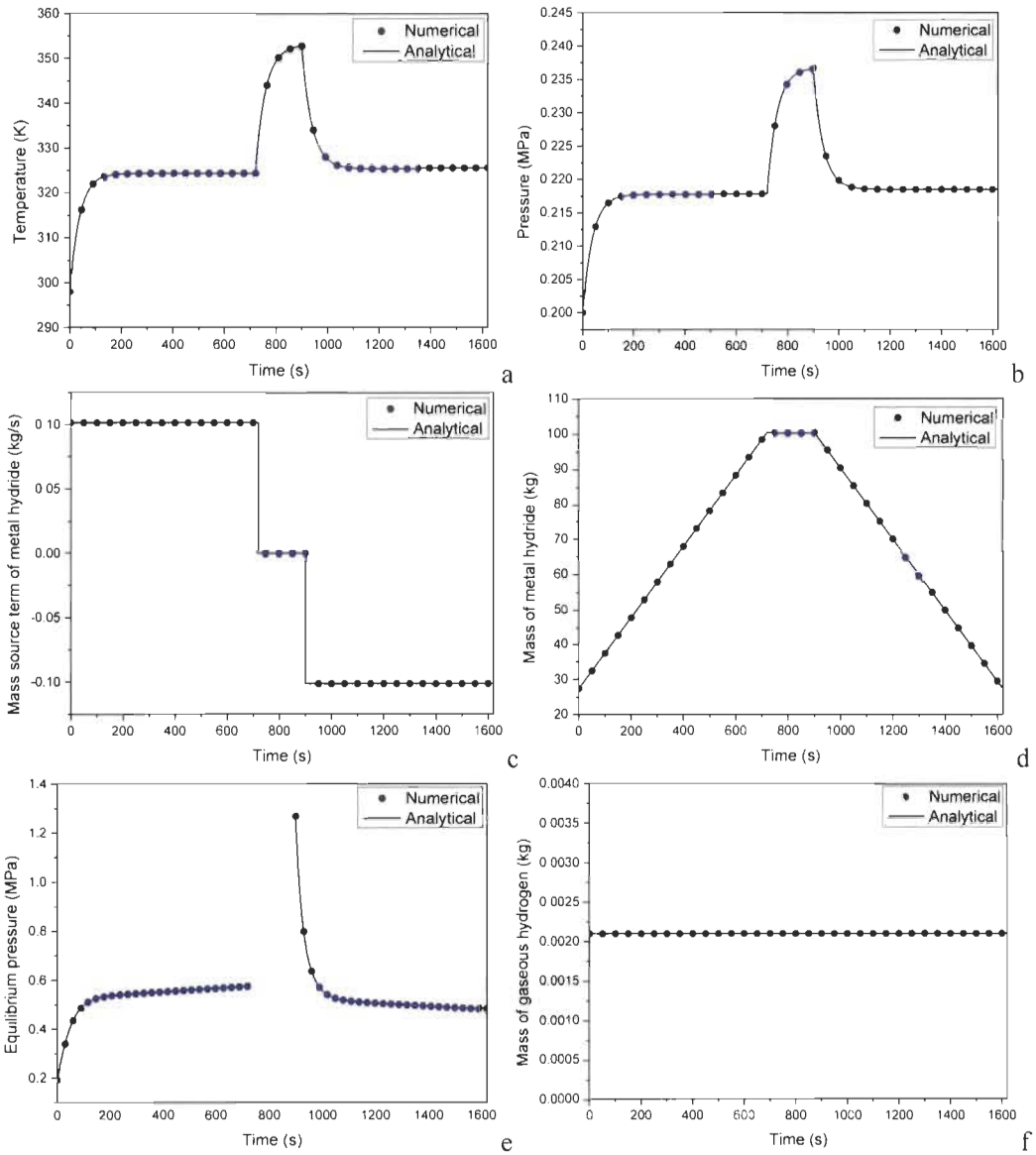

Fig.3.1 Validation of numerical model by analytical solutions: (a) lumped temperature, (b) pressure, (c) mass source term of metal hydride, (d) mass of metal hydride, (e) equilibrium pressure and (f) mass of gaseous hydrogen.

Table 3.2 Values of parameters used in Matlab/Simulink numerical model and analytical solution

Parameter	Value	Parameter	Value	Parameter	Value
A_s [m^2]	4.147	E_a [J/mol]	21170	R [J/mol/K]	8.314
V_g [m^3]	0.012	E_d [J/mol]	16420	$\Delta S_{a/d}$ [J/mol/K]	108
a_f [W/m^2/K]	243	C_a [1/s]	59.2	k_p [1]	0.13
m_{0M} [kg]	109.3	C_d [1/s]	9.6	p_0 [MPa]	0.1
T_∞ [K]	290	c_s [J/kg/K]	355	t_a [s]	720
$T_{f\text{cooling}}$ [K]	298	c_p [J/kg/K]	14.3e3	t_d [s]	720
$T_{f\text{heating}}$ [K]	353	c_v [J/kg/K]	10.3e3	t_{dormancy} [s]	180
M_{H_2} [kg/mol]	0.002	T_{initial} [K]	298	ΔH_a [J/mol]	30478
M_{MH} [kg/mol]	0.438	p_{initial} [MPa]	0.2	ΔH_d [J/mol]	30800

Table 3.3 Description of four cases with different inflow/outflow temperature

Case	Absorption stage	Desorption stage
1	Constant inflow temperature, $T_\infty = Const$	Variable outflow temperature, $T_\infty = T$
2	Constant inflow temperature, $T_\infty = Const$	Constant outflow temperature, $T_\infty = Const$
3	Variable inflow temperature, $T_\infty = T$	Constant inflow temperature, $T_\infty = Const$
4	Variable inflow temperature, $T_\infty = T$	Variable inflow temperature, $T_\infty = T$

Fig.3.1 shows the comparisons between the Matlab/Simulink numerical solutions and the analytical solutions, including the variations of the lumped temperature, the pressure, the mass source term of metal hydride, the mass of metal hydride, the equilibrium pressure and the mass of gaseous hydrogen, in order to validate the lumped parameter numerical model. In general, the numerical solutions of the lumped parameter model with constant mass source term agree well with the analytical solutions. The lumped temperature of the metal hydride reactor increases during hydriding and decreases during dehydriding. The temperature increases during dormancy since the reactor is heated, which is good for the dehydriding reaction. The metal hydride mass increases during hydriding and decreases during dehydriding. The sum of the mass flow rate and the hydrogen mass source is 0, and the mass of gaseous hydrogen in the metal hydride reactor is a fixed value. The variation curve of pressure

is as same as that of lumped temperature, which is according to the equation of state in the assumed conditions. The equilibrium pressure is presented in Fig.1e, which is calculated by Eq. (11). The equilibrium pressure is related to the lumped temperature and the mass of metal hydride, and the effect of the lumped temperature on the equilibrium pressure is more obvious than that of the mass of metal hydride. The equilibrium pressure shows the same trend as the lumped temperature.

3.3.3 Comparison among different analytical solutions

The analytical solutions using different inflow/outflow temperature are discussed. Then, the deduced model proposed in Ref.[52] is compared with the above analytical solutions in this section. The mass flow rate in the analytical solutions is assumed to be constant, the case using a variable mass flow rate is not considered in this work. Any of hydrogen inflow and outflow temperatures can be assumed as constant or variable, which results in analytical solutions under four different inflow/outflow conditions. The detailed information on the combinations is presented in Table 3.3.

Fig.3.2a shows the comparison of lumped temperature among the analytical solutions with different inflow/outflow temperature. When the inflow temperature is set as constant, the lumped temperature is about 0.7 K lower than that of others during hydriding. The lumped temperature in Case 2 and Case 3, where the outflow temperature is set as constant, is about 0.7 K higher than the others during dehydriding. The effect of the inflow/outflow temperature on the lumped temperature is not obvious due to a large amount of reaction heat.

A reduced model has been introduced and its usefulness has been confirmed in Ref.[52], where the hydrogen specific heat capacity and the enthalpy change caused by the hydrogen inflow are ignored. Based on these assumptions, the energy balance equation Eq. (3.12) becomes:

$$\mathrm{d}\left(m_s c_s T\right)/\mathrm{d}t = a_f A_s \left(T_f - T\right) - \Delta H_{a/d} \dot{S}_{\mathrm{H}_2} / M_{\mathrm{H}_2} \tag{3.30}$$

Solving Eq.(3.30), we obtain:

$$T = T^* + \left(T_0 - T^*\right)\exp\left[-a_f A_s t / \left(m_s c_s\right)\right] \tag{3.31}$$

where the characteristic time T^* is equal to $T_f - \Delta H_{a/d} \dot{S}_{\mathrm{H}_2} / \left(a_f A_s M_{\mathrm{H}_2}\right)$.

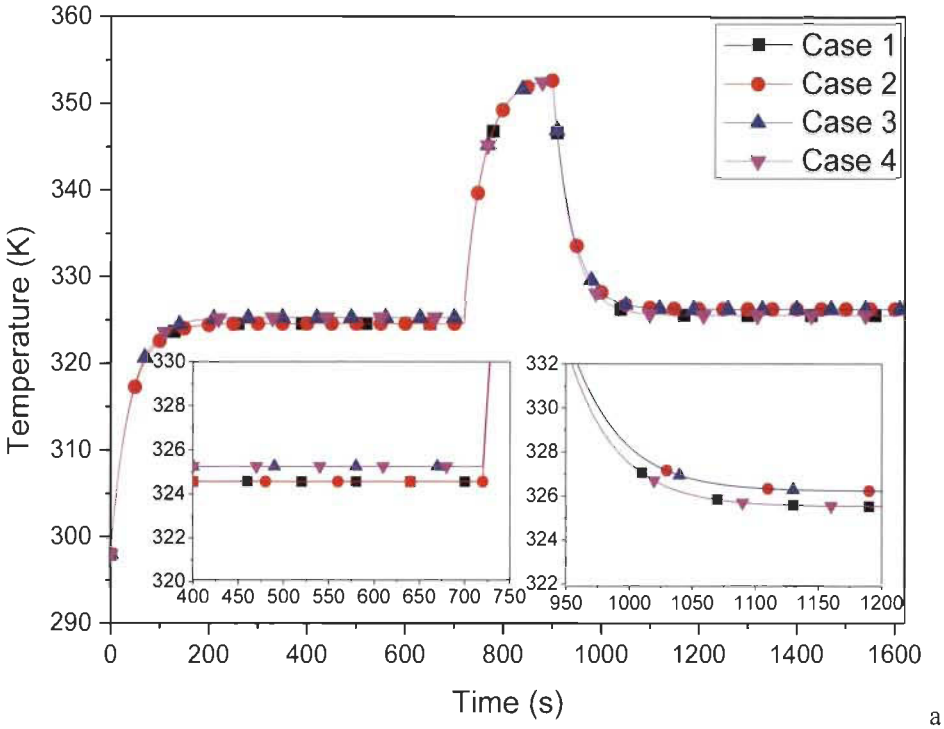

a

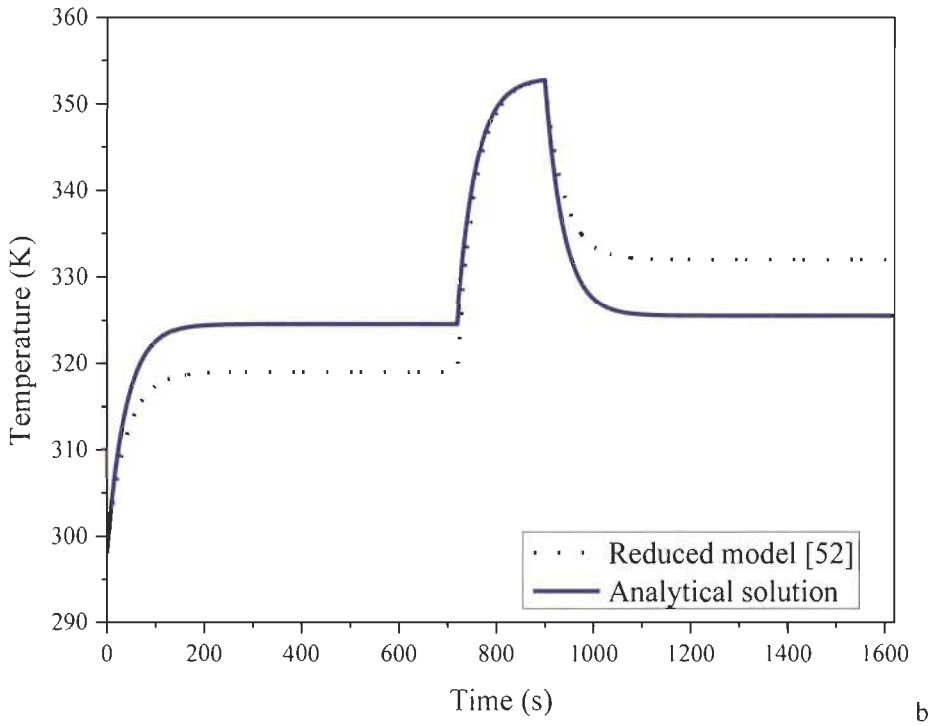

b

Fig.3.2 Temperature comparison of analytical solutions under different conditions: (a) variable/constant inflow/outflow temperature, (b) reduced model [52]

Based on the same parameters and conditions, we compare the lumped temperature of the analytical solutions with that of the reduced model results. Fig.3.2b shows that the lumped temperature of analytical solutions is about 5.5 K higher than that of the reduced model during hydriding. The results calculated by the reduced model is about 6.5 K higher than the other during dehydriding. The analytical solutions in the present work show more accurate than the reduced model.

3.4 Parametric study by numerical solution

The lumped parameter numerical model with constant source term has been validated by the analytical solutions. Then, the validated lumped parameter numerical model is used for parametric study in this section. The variable source term is easily and widely used in numerical models to simulate the hydriding-dehydriding cycle. The effect of variable mass source term on the numerical results of the lumped parameter model is discussed. The simulation results of the lumped parameter numerical model with variable mass source term are compared with those with constant mass source term. The effect of the mass flow rate on the metal hydride system is studied to exam the upper limit of the analytical solutions. Matlab/Simulink is used for numerical solutions.

3.4.1 Effect of variable mass source term

The effect of variable mass source term on the numerical solutions of the lumped parameters model is studied. The variable metal hydride source terms during hydriding and dehydriding can be calculated by Eq. (3.10a) and Eq. (3.10b). The mass source term is set as 0 when the hydrogen pressure p_{H_2} is between p_{eqa} and p_{eqd}. The variable mass source term means the variable reaction rate. The numerical solutions using the variable mass source term are compared with the numerical solutions using the constant mass source term.

Fig.3 shows the effects of the variable mass source term on the numerical solutions, including the lumped temperature, the pressure, the mass source term of metal hydride, the mass of metal hydride, the equilibrium pressure and the mass of gaseous hydrogen. As for the lumped temperature, the metal hydride mass and the equilibrium pressure, the results of the numerical model using variable mass term agree well with the other

in Fig.3.3a, Fig.3.3d and Fig.3.3e. Fig.3.3c shows that the mass source term of metal hydride during hydriding and dehydriding can be considered roughly as constant, which confirms that the constant mass source term used in the analytical solution gives reasonable approximated results. The value of variable mass source term is below that of constant mass source term due to a relative lower temperature at the beginning of the hydriding process.

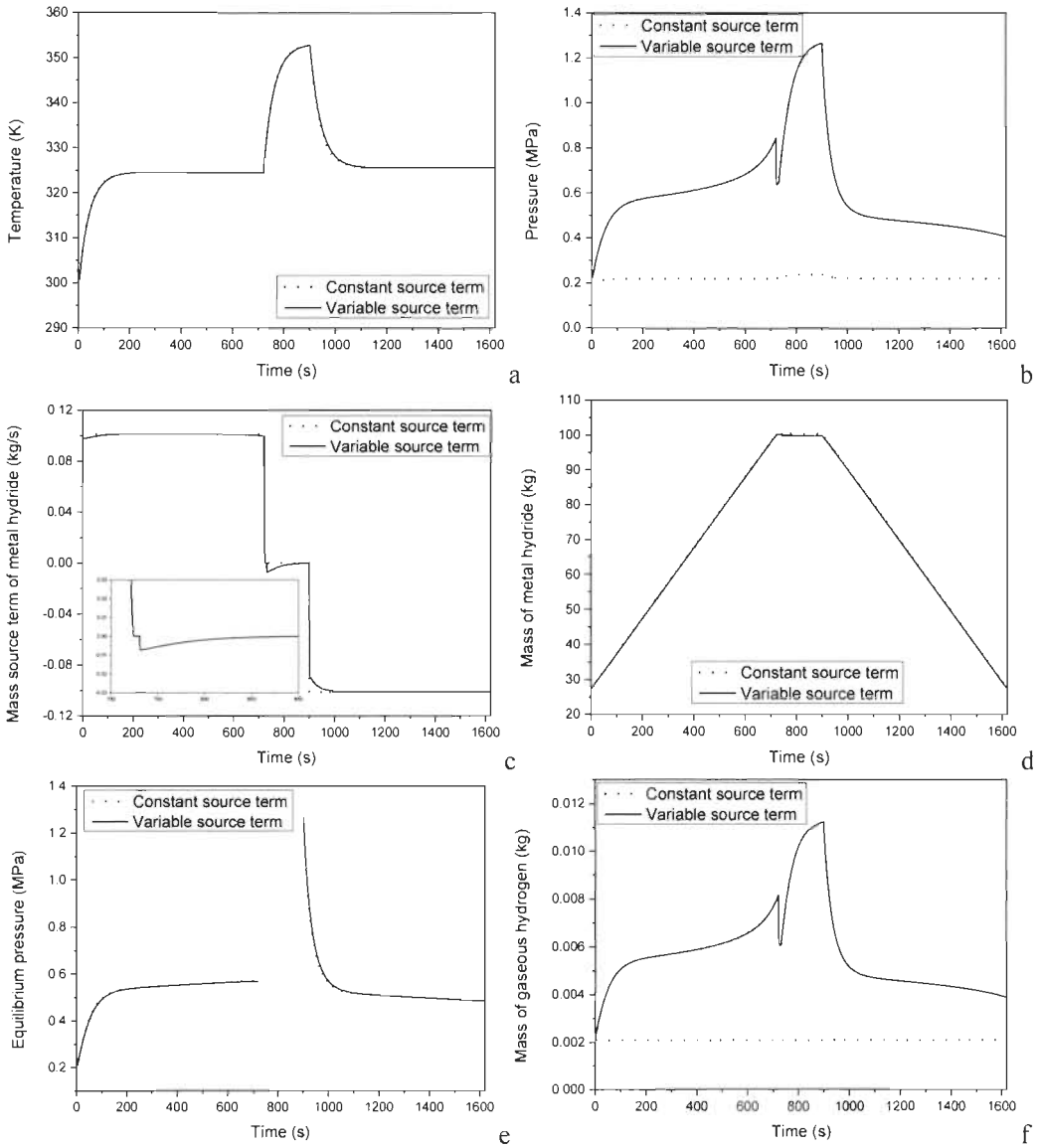

Fig.3.3 Comparison for cases using lumped parameter numerical model with constant/variable source term: (a) lumped temperature, (b) pressure, (c) mass source term of metal hydride, (d) mass of metal hydride, (e) equilibrium pressure and (f) mass of gaseous hydrogen.

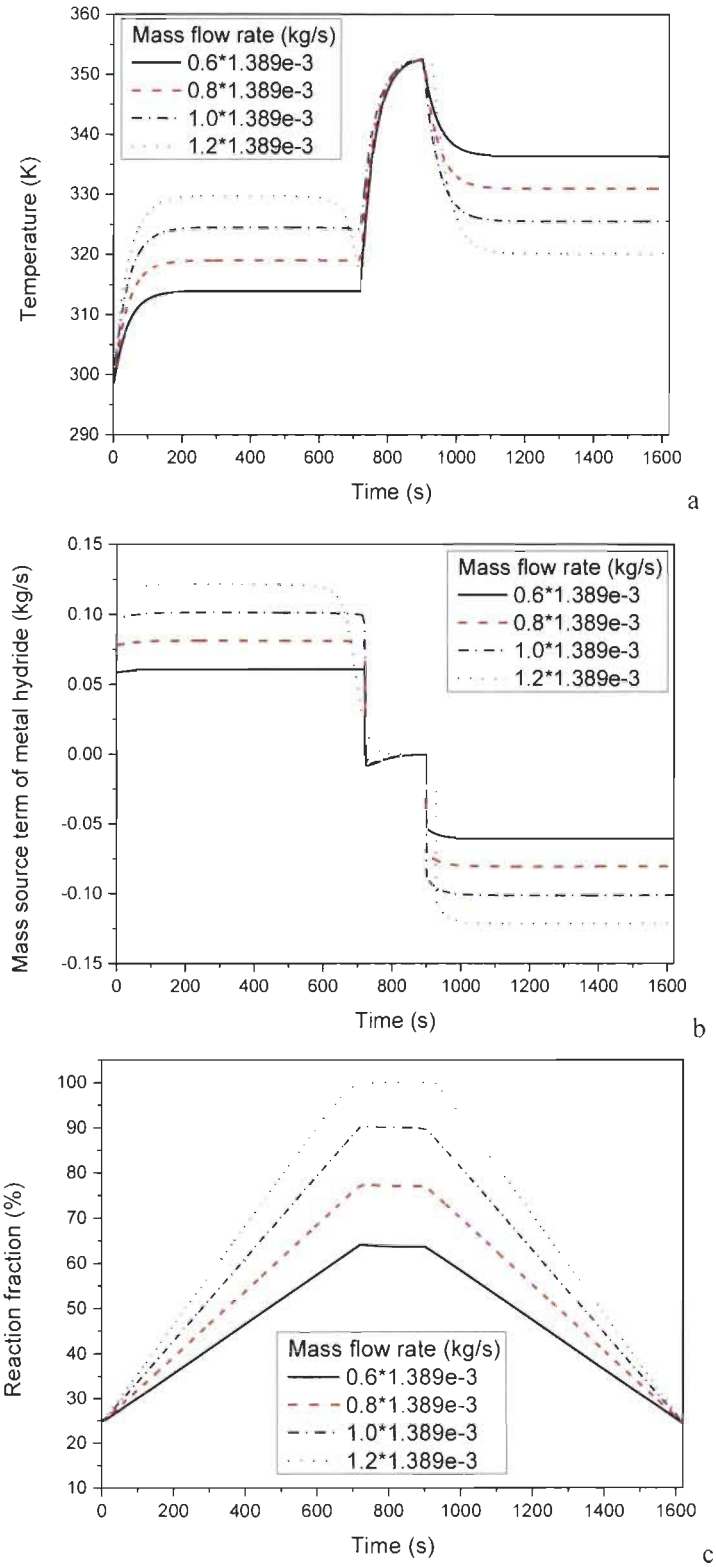

Fig.3.4 Comparison for cases using lumped parameter numerical model with different mass flow rates: (a) lumped temperature, (b) mass source term of metal hydride and (c) reaction fraction.

As for the pressure and the gaseous hydrogen mass, the difference between two numerical solutions is obvious. The pressure and the gaseous hydrogen mass in the metal hydride reactor are related to the source term. The ratio of the hydrogen mass source term to the mass flow rate is assumed as -1 in the numerical model with the constant mass source, which makes the mass of gaseous hydrogen in the metal hydride reactor to be constant. Therefore, the pressure calculated by the model with constant source term is approximately constant. As for the numerical model with variable source term, the metal hydride mass source term $\dot{S}_{\mathrm{MH}}$ is a negative quantity after about 731s during dormancy in Fig.3.3c. Thus, the hydrogen mass source term $\dot{S}_{\mathrm{H_2}}$ is a positive quantity and the gaseous hydrogen mass increases in that process, which causes the increase of the hydrogen pressure $p_{\mathrm{H_2}}$ during the later dormancy in Fig.3.3b. Due to the similar reason, the hydrogen pressure $p_{\mathrm{H_2}}$ decreases during the earlier dormancy. Considering the gaseous hydrogen mass in the reactor is a relatively small quantity, the effect of gaseous hydrogen mass on the numerical results is not significant. In general, the numerical model with a variable source term is more accurate than the other to predict the hydriding-dehydriding cycle process.

3.4.2 Effect of mass flow rate

Based on the Matlab/Simulink numerical model using the variable source term, the effect of the mass inflow rate on the metal hydride system is taken into consideration. The absolute value of the mass inflow rate is equal to that of the mass outflow rate. Four cases with different mass flow rates are discussed in this section, and the absolute values of the mass flow rate are presented in Fig.3.4. The reaction fraction X is defined as the ratio of the metal hydride mass m_{MH} to the saturated solid material mass m_s^{sat}. The reaction fraction X is about 100% when the hydrogen storage capacity of the metal hydride system approaches the limited capacity.

Fig.3.4 shows the comparison of the numerical solutions among four cases with different mass flow rates, including the lumped temperature, the mass source term of metal hydride and the reaction fraction. Fig.3.4a shows the lumped temperature during hydriding generally rises with the increase of mass inflow rate, and the lumped

temperature during dehydriding decreases with the increase of mass outflow rate. Fig.3.4b shows the metal hydride source term $\dot{S}_{MH}$ during hydriding and dehydriding can be considered roughly as constant in the cases with a relatively small mass flow rate. Fig.3.4c shows the maximum reaction fractions in four cases are about 64.1%, 77.2%, 90.3% and 100%. It takes less time to approach the limited capacity by taking a relatively large mass flow rate.

As for the case with the maximum mass flow rate, the metal hydride source term $\dot{S}_{MH}$ decreases when the reaction fraction is beyond about 90% during hydriding, and the lumped temperature reduces due to the decrease of reaction heat and the heat transfer from the metal hydride bed to the cooling water. The analytical solution is solved from the thermodynamic model based on the assumption that both the mass flow rate and the mass source term are constant. The metal hydride source term or the reaction rate during hydriding is almost constant when the reaction fraction is below about 90% during hydriding, as shown in Fig.3.4b and Fig.3.4c. When the hydriding reaction is close to the saturation condition, the metal hydride source term or the reaction rate decreases and cannot be considered roughly as constant. In this article, we exactly solved the model to give the analytical solutions under different conditions. The model used for analytical solutions is an approximate model when the hydrogen storage capacity of the metal hydride system is above about 90% of its limited capacity.

3.5 Conclusion

The thermodynamic model for the hydrogen storage system using metal hydride, including the mass and energy balance equations, reaction kinetics equation, equilibrium pressure equation and equation of state for the ideal gas, has been presented in detail. The analytical solutions of lumped temperature are obtained from the thermodynamic model in various processes, including hydriding, dormancy and dehydriding processes. A lumped parameter numerical model is developed on the Matlab/Simulink platform. The analytical solutions are applied to validate the numerical model with a constant reaction rate. Further, the analytical solution can be used as a reference for more detailed two-dimensional or three-dimensional models.

Any of hydrogen inflow and outflow temperatures can be assumed as constant or variable, which results in analytical solutions under four different inflow/outflow conditions. Four cases under constant/variable inflow/outflow temperature conditions are analytically studied, the results show that the effect the *variable* inflow/outflow temperature condition on the lumped temperature in metal hydride system is not obvious compared to the *constant* inflow/outflow temperature condition. The analytical solution for the hydriding-dehydriding cycle is compared with the result of a reduced model proposed in the reference, the comparison shows that the analytical solution is more accurate than the reduced model. Then, the variable mass source term is taken into consideration in the validated lumped parameter numerical model. The lumped temperature of the metal hydride system, the mass of metal hydride and the equilibrium pressure in the numerical solutions using variable mass source term agree well with those in the numerical model using constant mass source term. The effect of mass flow rate on the metal hydride hydrogen storage system is discussed, the results show that the lumped temperature rises during hydriding and decreases during dehydriding with the increase of mass inflow rate. It takes less time to approach the limited capacity by taking a relatively large mass flow rate. The metal hydride source term during hydriding can be considered roughly as constant, which is true when the hydrogen storage capacity of the metal hydride system is not beyond about 90% of its limited capacity

Chapter 4 Hydrogen Storage based on Metal Hydride with Coiled Tube Heat Exchanger

This section has been published in: Tong L, Xiao J S, Yang T Q, et al. Complete and reduced models for metal hydride reactor with coiled-tube heat exchanger. International Journal of Hydrogen Energy, 2019, 30(44):15907-15916.

My specific contributions in this work was to design coiled-tube and straight pipe as heat exchangers to enhance heat transfer in the metal hydride hydrogen storage tank. Reduced 2D model for coiled-tube heat exchanger was developed, which can well approximate complete 3D model.

Metal hydride can be considered as a safe and effective method to store hydrogen. A large amount of heat is generated during hydriding while a lot of heat is absorbed in the dehydriding process. The thermal effects during hydriding/dehydriding have a significant influence on the performance of metal hydride reactor. The geometry of the metal hydride reactor and the structure of the heat exchanger should be carefully designed for better performance.

4.1 Mathematical model of metal hydride system

The mathematical model of metal hydride hydrogen storage system is based on the governing equations, including mass and momentum conservation equation, energy conservation equation, equation of reaction kinetics, equilibrium pressure equation and equation of state. The effect of the reactor wall on the metal hydride hydrogen storage system is neglected in the mathematical model. The mass conservation equation for gaseous hydrogen in the reactor can be expressed as:

$$\frac{\partial}{\partial t}\left(\varepsilon_{\mathrm{b}}\rho_{\mathrm{g}}\right)+\nabla\cdot\left(\rho_{\mathrm{g}}\vec{v}\right)=S_{\mathrm{H_2}} \tag{4.1}$$

where ε_{b} is the porosity of metal hydride bed, ρ_{g} (kg/m^3) is the density of hydrogen, $\vec{v}$ (m/s) is the Darcy velocity and $S_{\mathrm{H_2}}$ is the mass source term of hydrogen. The mass

source term S_{H_2} is negative during hydriding and positive during dehydriding. The Darcy velocity $\vec{v}$ is presented as:

$$\vec{v} = -\frac{\kappa}{\mu}\nabla p \tag{4.2}$$

where κ (m^2) is the permeability, μ (Pa s) is the dynamic viscosity and ∇p (Pa/m) is the pressure gradient.

The solid materials include the alloy and the metal hydride. As for the solid materials, the mass conservation equation can be considered as:

$$\left(1-\varepsilon_b\right)\frac{\partial \rho_s}{\partial t} = S_s \tag{4.3}$$

where ρ_s (kg/m^3) is the solid material density. S_s is the mass source term of solid materials, the relationship between S_s and S_{H_2} can be written as $S_{H_2} = -S_s$.

The energy conservation equation of the metal hydride system is described as:

$$\left(\rho c_p\right)_{\text{eff}}\frac{\partial T}{\partial t} + \rho c_p \vec{v}\cdot\nabla T = \nabla\cdot\left(k_{\text{eff}}\nabla T\right) + S_s\left[\Delta H + T\left(c_{pg} - c_s\right)\right] \tag{4.4}$$

The effective heat capacity $\left(\rho c_p\right)_{\text{eff}}$ is $\varepsilon\rho_g c_{pg} + \left(1-\varepsilon_b\right)\rho_s c_s$, and the effective thermal conductivity k_{eff} is $\varepsilon k_g + \left(1-\varepsilon_b\right)k_s$. The porosity ε_b is assumed as constant during hydriding. The local thermal equilibrium is assumed to be valid between the solid phase and the gaseous phase, and the gaseous phase temperature is equal to the solid phase temperature in our model. The mass source term of solid materials S_s is relative with the reaction kinetics equation of metal hydride and the equilibrium pressure [22, 23, 25].

$$S_s = C_a e^{-E_a/(RT)}\ln\left(p_{H_2}/p_{eqa}\right)\left(\rho_s^{\text{sat}} - \rho_s\right), \text{ for } p_{H_2} > p_{eqa} \tag{4.5a}$$

$$S_s = -C_d e^{-E_d/(RT)}\left[\left(p_{eqd} - p_{H_2}\right)/p_{eqd}\right]\left(\rho_s - \rho_s^{\text{emp}}\right), \text{ for } p_{H_2} < p_{eqd} \tag{4.5b}$$

where $C_{a/d}$ (1/s) is kinetics constant, $E_{a/d}$ (J/mol) is activation energy, $p_{eqa/d}$ (Pa) is equilibrium pressure, T (K) is temperature, the subscript a/d refers to the absorption/desorption process. ρ_s^{sat} (kg/m^3) is the saturated density of solid materials and the alloy is fully transformed to the metal hydride in the saturated condition. ρ_s^{emp}

(kg/m^3) is the density of solid materials when all of the metal hydrides has transformed into the alloy and the hydrogen. The equilibrium pressure equation can be described as[25]:

$$\ln\left(p_{eqa/d} / p_{ref}\right) = A_{a/d} - B_{a/d} / T \tag{4.6}$$

where p_{ref} (MPa) is the reference pressure and set as 1MPa. In this work, the gaseous hydrogen is considered as the ideal gas. The hydrogen storage capacity of the metal hydride reactor can be written as follows:

$$\text{wt} = \frac{m_s - m_s^{emp}}{m_s^{emp}} \times 100\% \tag{4.7}$$

where m_s (kg) is the mass of solid materials in the metal hydride reactor. In general, the solid materials include the alloy and the metal hydride. m_s^{emp} (kg) is known as the emptied mass of solid materials, and it is equal to the solid material mass when the whole of metal hydride in the reactor is converted as alloy and hydrogen. m_s^{sat} (kg) is the saturated mass in the metal hydride reactor when the whole of alloy reacts with hydrogen and transforms as the metal hydride. The value of solid material mass m_s changes between the emptied mass m_s^{emp} and the saturated mass m_s^{sat}.

4.2 Model parameters

4.2.1 Geometric model

There are six types of metal hydride reactors packed with $LaNi_5$ in this work. Six structures are designed for simulation cases: Case A to F, as shown in Fig.4.1. The metal hydride reactors of Case A and B are two-dimensional (2D) axisymmetric models, Case C, D and E are complete three-dimensional (3D) models, Case F is a reduced model of the complete three-dimensional model Case C.

4.2.2 Material properties

In order to validate the mathematical model of metal hydride reactor, its simulation results were compared with other data from Refs.[25, 26]. The effect of the tank wall on the metal hydride system is ignored. The temperature of circulating cooling water

is set as constant. The parameters of metal hydride and hydrogen properties used in the simulation are shown in Table 4.1 [24, 25].

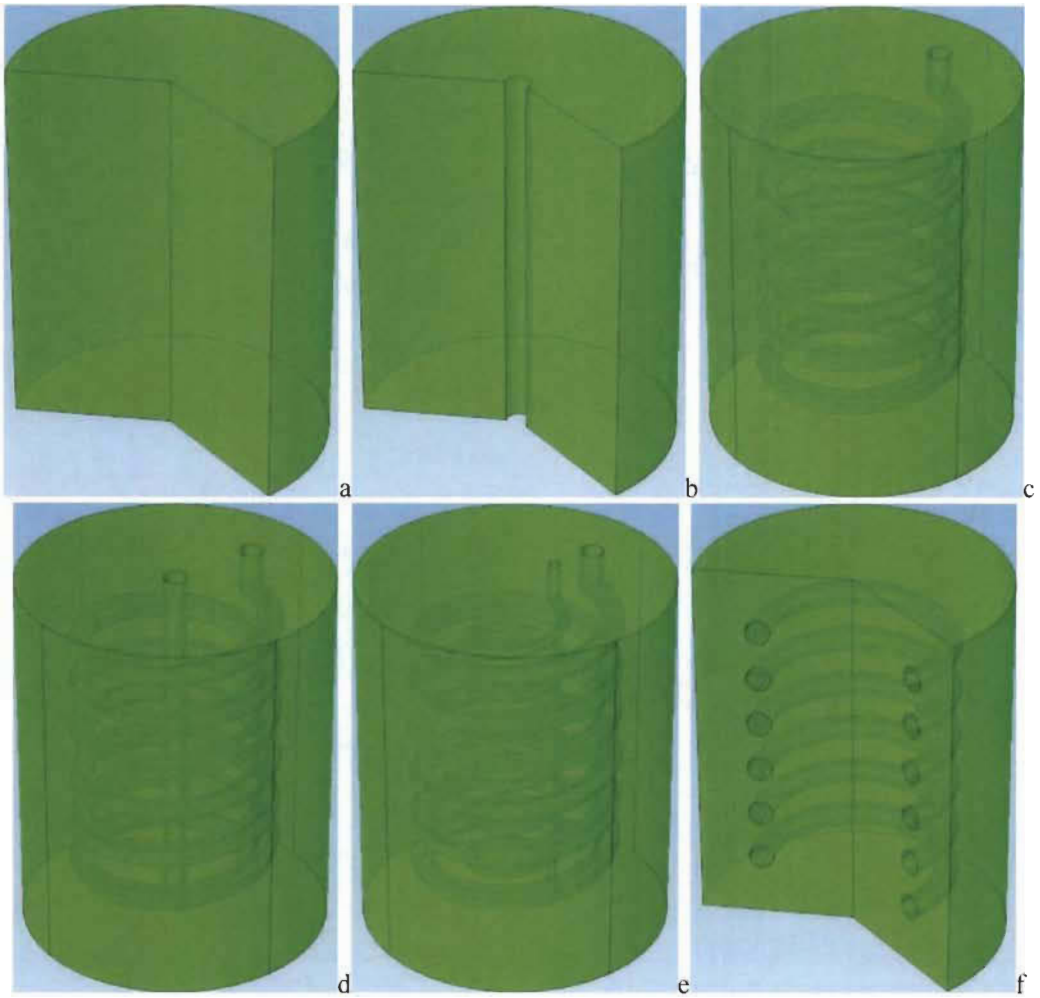

Fig.4.1 Diagram of different metal hydride reactor (a) without heat exchanger, (b) with straight pipe heat exchanger, (c) with coiled-tube heat exchanger, (d) with coiled-tube heat exchanger and straight pipe heat exchanger, (e) with dual coiled-tube heat exchangers and (f) with parallel ring tube heat exchanger.

4.2.3 Boundary and initial conditions

The metal hydride reactor is cooled by the circulating cooling water during hydriding. The ambient temperature is set as the same as the cooling water temperature. There are three kinds of boundary conditions in the 2D axisymmetric model, including pressure boundary condition, heat flux and axis. The inlet is set as the pressure boundary condition. The initial pressure in the tank is 0.143MPa. We suppose that the pressure increases linearly from initial pressure to constant pressure (0.8MPa) in the first 100s,

and maintains at the constant pressure [25]. The outer boundaries of metal hydride reactor are set as heat flux, and the heat transfer coefficient h_j between the metal hydride reactor and the ambient environment is constant. The initial temperature in the tank is assumed to be the ambient temperature T_j.

Table 4.1 Parameters of metal hydride and hydrogen properties

Parameter	Values	Parameter	Values	Parameter	Values
ε_b [1]	0.5	E_a [J/mol]	21179.6	A_a [1]	10.7
ρ_{emp} [kg/m^3]	7164	E_d [J/mol]	16473	B_a [1/K]	3704.6
ρ_{sat} [kg/m^3]	7259	C_a [1/s]	59.187	R [J/mol/K]	8.314
h_j [W/m^2/K]	1652	C_d [1/s]	9.57	M_{H_2} [kg/mol]	2.0159e-3
κ [m^2]	10^{-8}	c_p [J/kg/K]	14890	k_s [W/m/K]	2.4
T_f [K]	293	c_s [J/g/K]	419	k_g [W/m/K]	0.1815
ΔH_a [J/kg]	1.537e7	p_{ref} [MPa]	1		

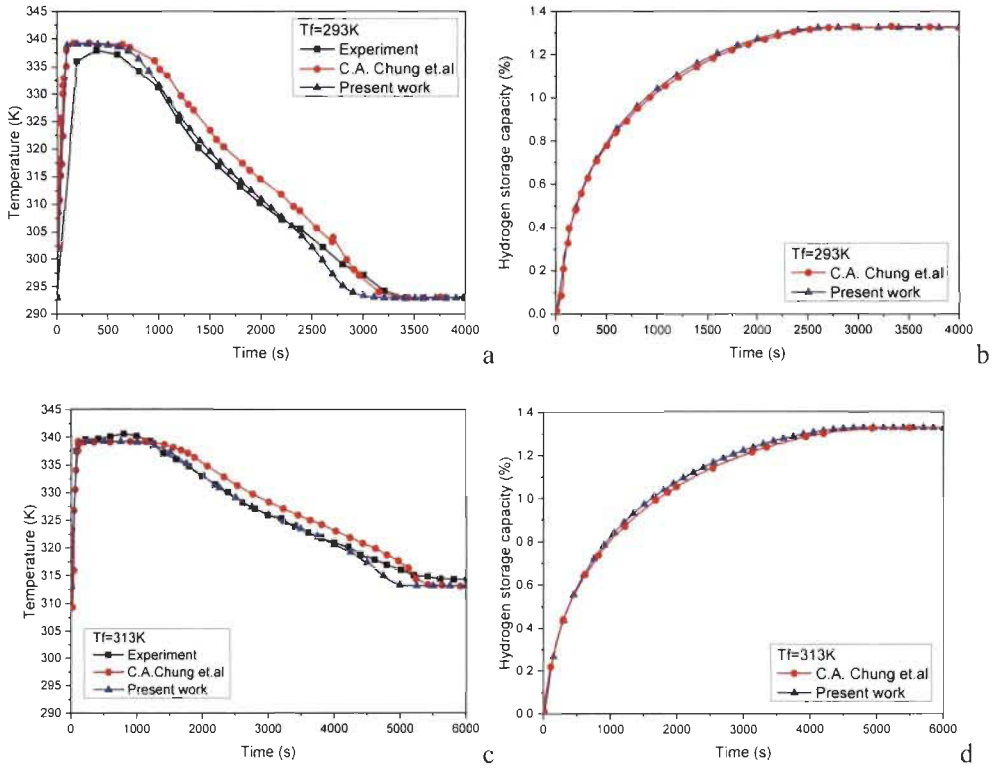

Fig.4.2 Model verification on monitor point temperature (a, c) and hydrogen storage capacity (b, d) under different ambient temperatures, using 2D model for Case A.

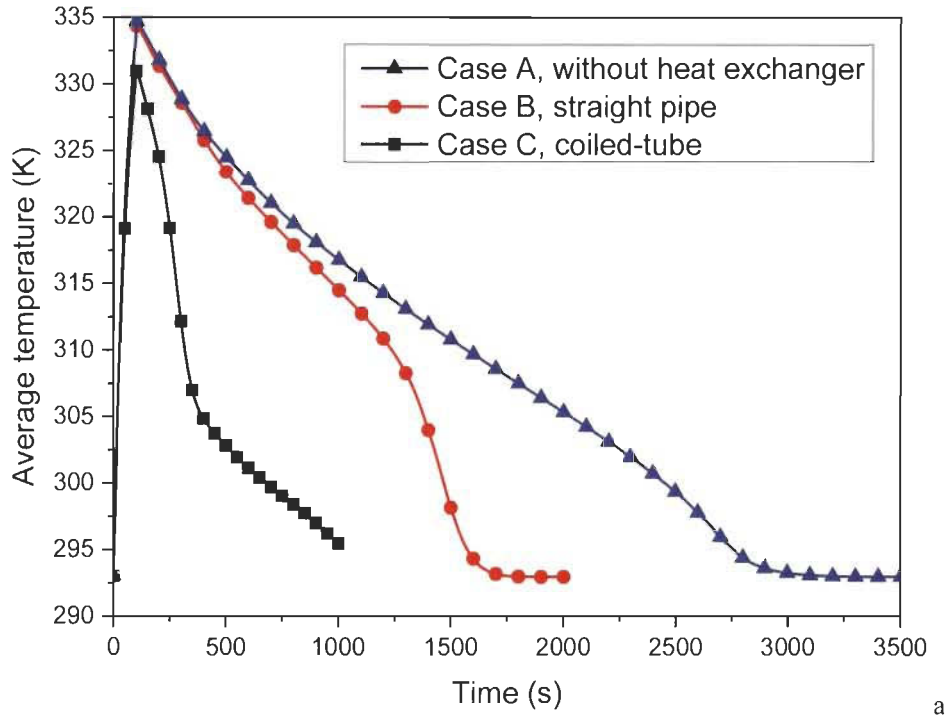

a

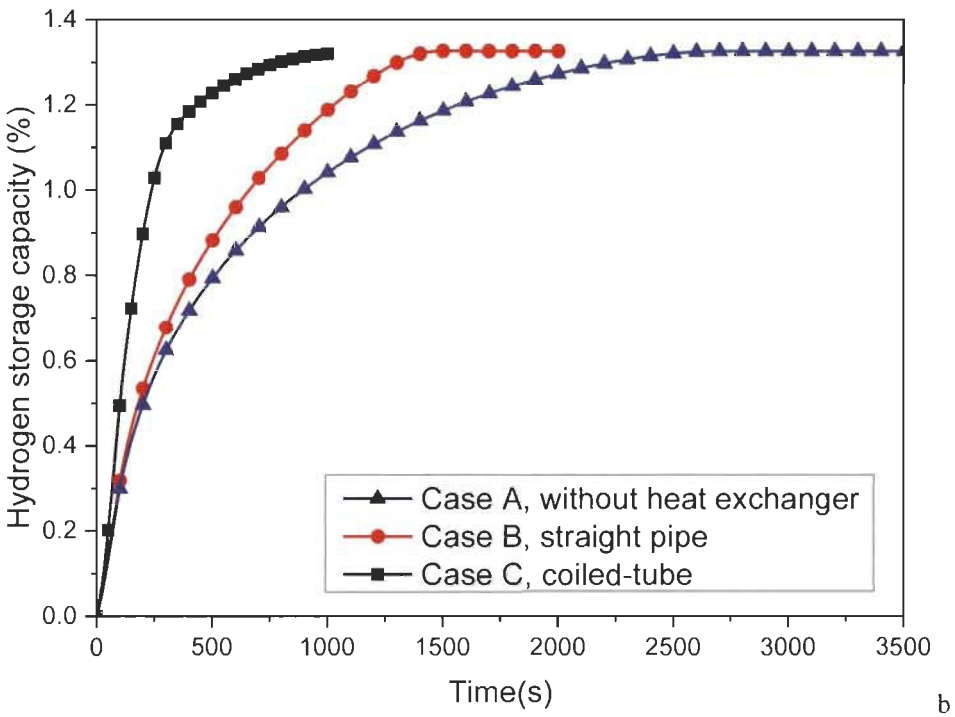

b

Fig.4.3 Simulation results of average temperature (a) and hydrogen storage capacity (b) in the reactors with straight pipe and coiled-tube heat exchangers, compared with the reactor without heat exchanger, using 2D model for Case A and B and 3D model for Case C.

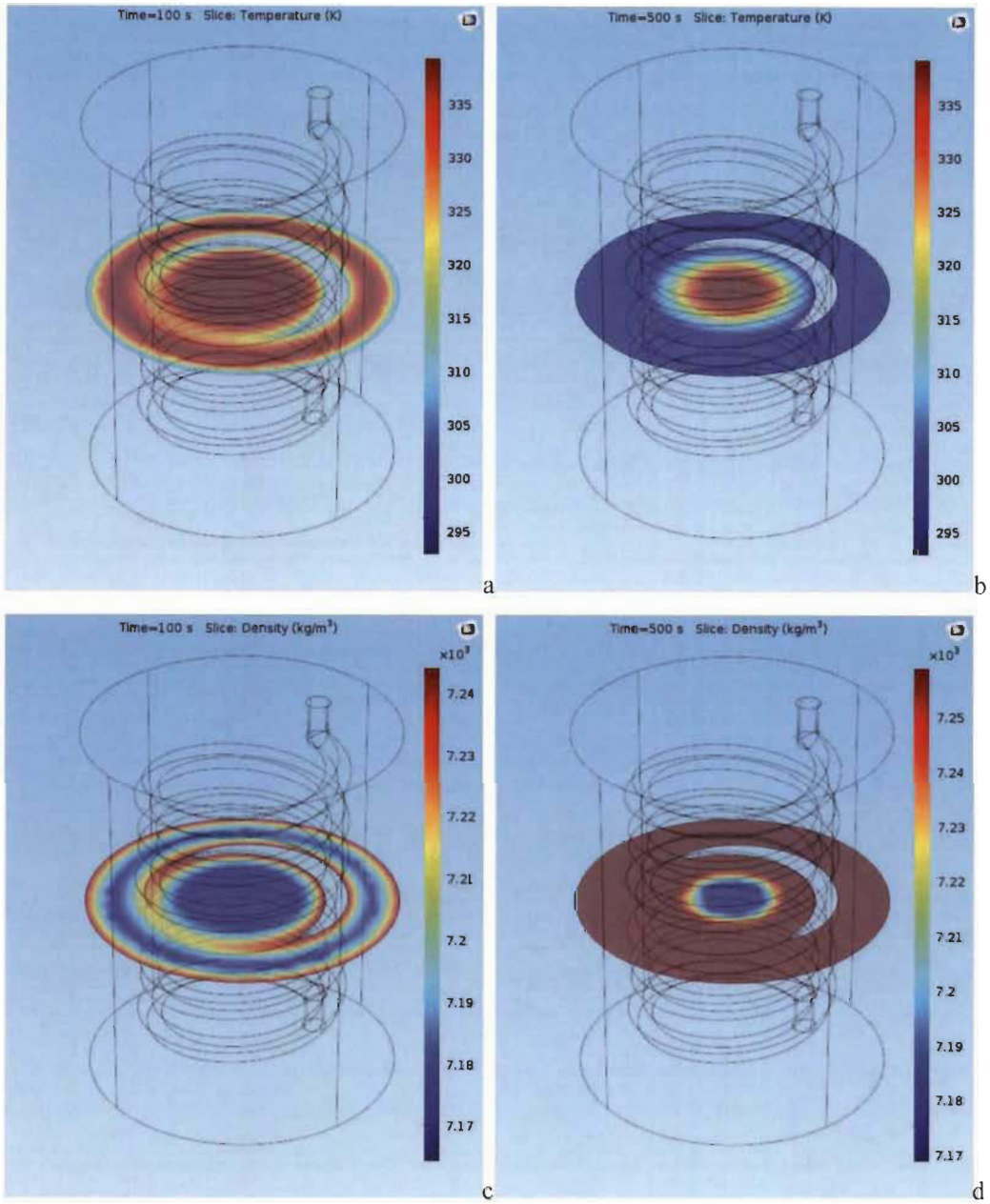

Fig. 4.4 Contours of temperature (a, b) and solid material density (c, d) in the reactor with a single coiled-tube heat exchanger at 100s (a, c) and 500s (b, d)

4.3 Results and discussions

4.3.1 Model validation

The model is developed on the Comsol software platform, its simulation results were compared with other works in the Refs.[25, 26]. The mesh sensitive analysis has been

taken into consideration. The effects of the element size of the mathematical model, including extra fine, finer, fine, normal and coarse, on the density of monitoring point (r=1.5cm, z=3.5cm) are studied. The results indicate that there is no obvious difference between extra fine and finer in Case A. The complete mesh in Case E which is the most complex model in our work consists of 403532 domain elements, 42172 boundary elements and 5187 edge elements. It has been validated and presented enough calculation precision. The temperature of monitoring point in the metal hydride hydrogen storage tank at different ambient temperature are presented in Fig.4.2a and Fig.4.2c. The hydrogen mass in metal hydride has been calculated in Ref.[25], which can be used to get the hydrogen storage capacity of the metal hydride reactor by Eq.(4.7). In general, the simulation results agreed well with other works, and the two-dimensional axisymmetric model can be considered to be validated.

4.3.2 Comparison between coiled-tube and straight pipe heat exchanger

The coiled-tube heat exchangers are used to improve hydrogen storage performance. There are three important parameters for the coiled-tube heat exchanger, including the diameter of the helical coil pipe, the helical diameter and the helical pitch [38]. In this section, the helical diameter and the helical pitch are set as 0.03m and 0.008m, respectively. The pipe diameter of two kinds of heat exchangers is both assumed as 0.004m.

The boundary conditions for the coiled-tube heat exchanger and the straight pipe heat exchanger are set as heat flux, the circulating cooling water temperature and the heat transfer coefficient between metal hydride reactor and cooling water are assumed to be constant in our work.

Fig.4.3 shows the simulation results of different designs of metal hydride reactor, including the average temperature of the metal hydride reactor and the hydrogen storage capacity. The metal hydride reactors in Case A and B are reduced as two dimensional axisymmetric models, and a complete three dimensional model is developed for Case C. The average temperature increases quickly due to the reaction heat released, and declines with the decrease of reaction rate and heat transfer from metal hydride to ambient environment through heat exchanger. The heat exchangers

have a significant effect on the whole system. The metal hydride reactor in Case A, B and C takes 1531s, 1012s and 419s to reach up to 90% of the max value of hydrogen storage capacity, respectively. The results show that the effect of the coiled-tube heat exchanger on the reaction rate of the metal hydride reactor is obviously better than that of the straight pipe heat exchanger. The single coiled-tube heat exchanger also shows better performance of heat transfer than those of straight pipe heat exchanger, and it can be used to decrease the peak value of average temperature in the reactor.

Fig.4.4 presents the contours of temperature (a, b) and solid material density (c, d) in metal hydride reactor with a single coiled-tube heat exchanger at 100s (a, c) and 500s (b, d). Fig.4.4a shows that the temperature of the area near the heat exchanger is lower than others due to the heat transfer between the reactor and the cooling water. The temperature of the central area is higher than others in Fig.4.4b. It is difficult to transfer heat from the central area to the ambient environment. The solid material density increases during hydriding, and reaches to the saturated situation quickly in a relative lower temperature area. The density of area near heat changer reaches to the saturated situation earlier than others in Fig.4.4c.

4.3.3 Optimization of coiled-tube heat exchanger

In order to improve the performance of heat transfer in the central area, metal hydride reactors equipped with dual heat exchangers are discussed in this section. The combination of coiled-tube and straight pipe is taken into consideration in Fig.4.1d. The diameter of the straight pipe is the same as that of coiled-tube. Fig.4.1e shows dual coiled-tube heat exchangers, the diameter of the inner helical coil pipe and the helical diameter are set as 0.002m and 0.015m, respectively.

Fig.4.5 shows the comparison results among the metal hydride reactors with different coiled-tube heat exchangers, including average temperature (a) and hydrogen storage capacity (b). The difference in average temperature among the three cases is not obvious in the first 100s. The dual coiled-tube heat exchangers show better heat transfer performance than others in the latter process. There is no significant difference in the average temperature between Case C and D in about first 350s. The average temperature in Case D decreases faster than that in Case C after about 350s. However,

the effect of various coiled-tube heat exchangers on the hydrogen storage capacity of metal hydride reactor is clearly different. The metal hydride reactors in Case C, D and E take 419s, 323s and 271s to reach up to 90% of the max value of hydrogen storage capacity, respectively. It takes relatively little time to reach the limited value of hydrogen storage capacity in the reactor equipped with dual coiled-tube heat exchangers in Fig.4.5b.

Fig.4.6 presents the contours of temperature (a, b) and solid material density (c, d) in the reactor with dual coiled-tube heat exchangers at 100s (a, c) and 400s (b, d). Fig.4.6b shows that the high-temperature area is smaller than that in Fig.4.4b. It takes relatively little time to reach the saturated situation in the reactor with dual coiled-tube heat exchangers. The rotation direction of the inner coiled-tube heat exchanger is also taken into consideration. When the rotation direction of the inner coiled-tube heat exchanger is the opposite of the outer coiled-tube heat exchanger, the difference of their average temperatures is slight, and hydrogen storage capacity is almost unchanged.

The inserted heat exchanger can increase the heat transfer performance of the metal hydride reactor. The metal hydride reactor in the above five cases takes 1531s, 1012s, 419s, 323s and 271s to reach up to 90% of the max value of hydrogen storage capacity. However, the inserted heat exchanger also decreases the hydrogen capacity for the system. The initial solid material mass in Case A, B, C, D and E is 0.42199kg, 0.41659kg, 0.39548kg, 0.39231kg and 0.39166kg. When the alloy is converted into the metal hydride, the stored hydrogen qualities of the five cases are 5.60g, 5.52g, 5.24g, 5.20g and 5.19g. Considering the effect of the inserted heat exchanger on the hydrogen storage quality is not significant, the inserted heat exchanger can be regarded as an effective method to improve the performance of the metal hydride reactor.

4.3.4 Reduced model of coiled-tube heat exchanger

In order to decrease the computing time of the complete 3D model, the reduced 2D model is applied for the metal hydride tank with the coiled-tube heat exchanger, as shown in Fig.4.1f. We suppose that the heat in the metal hydride reactor transfers only from the coiled-tube heat exchanger to the ambient environment, and the outer surfaces of the metal hydride reactor are set to be adiabatic for simplification.

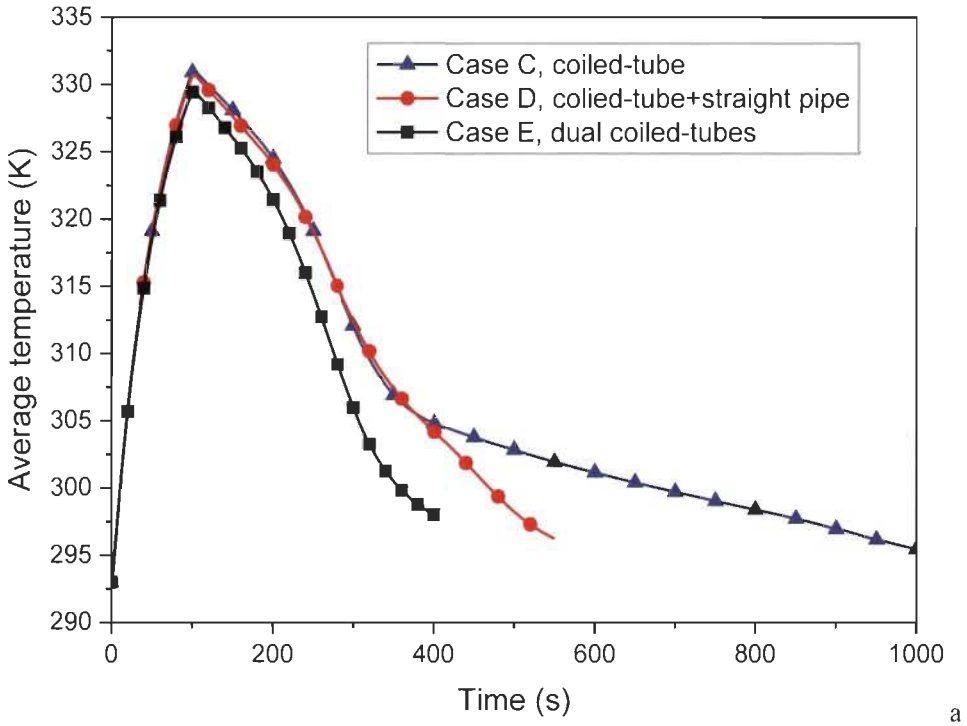

a

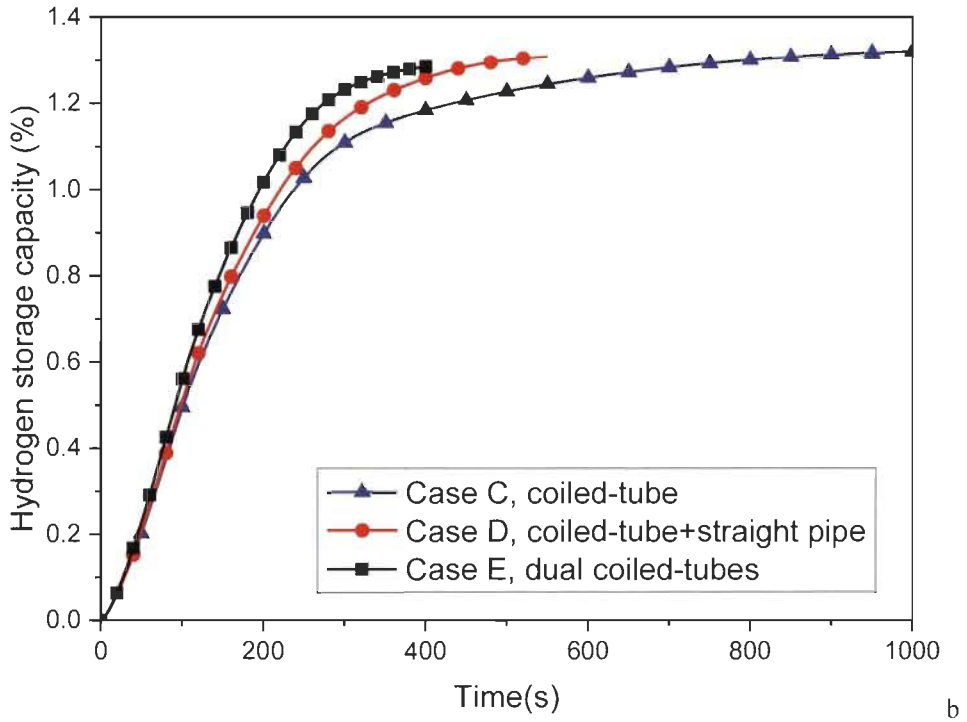

b

Fig.4.5 Simulation results of optimization of coiled-tube heat exchanger, including average temperature (a) and hydrogen storage capacity (b), using 3D model for Case C, D and E.

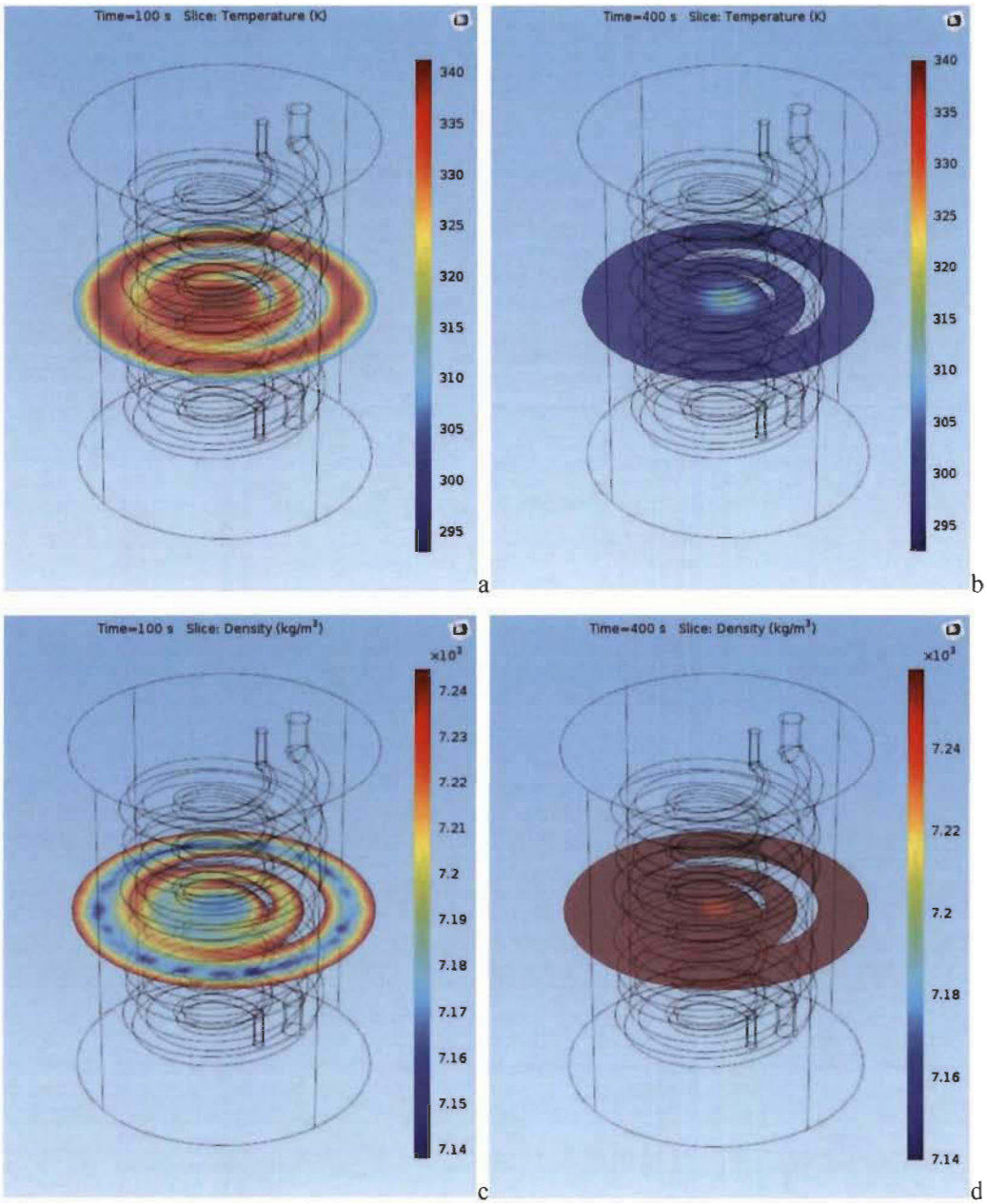

Fig.4.6 Contours of temperature (a, b) and solid material density (c, d) in the reactor with dual coiled-tube heat exchangers at 100s (a, c) and 400s (b, d)

The coiled-tube heat exchanger is simplified as parallel ring tubes heat exchanger, then the 3D model can be deduced as a 2D axisymmetric model. The boundary conditions for all parallel ring tubes are set to be the same in the current simulation, which can be varied according to the overall heat transfer situation.

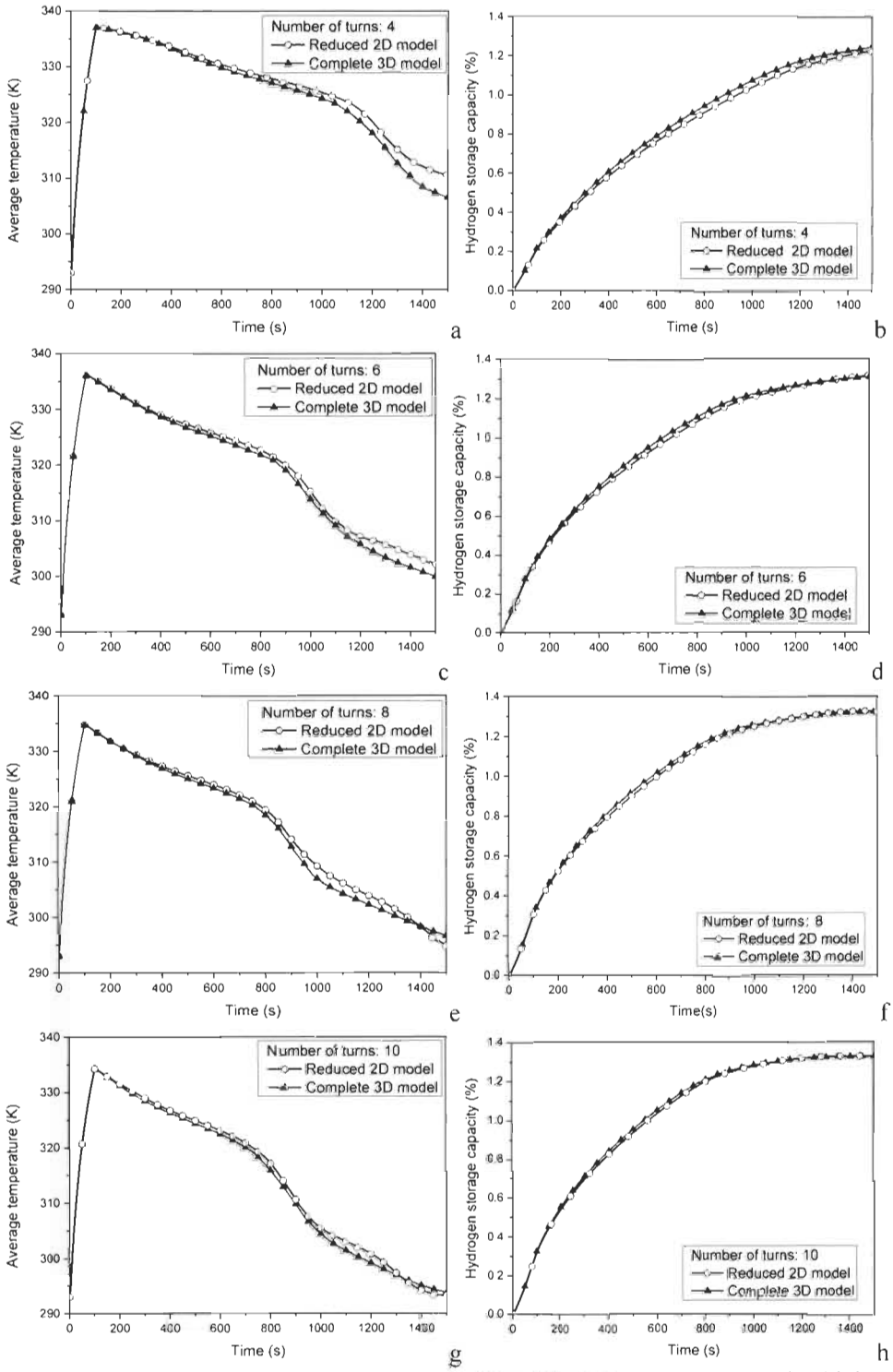

Fig.4.7 Comparison of average temperature (left) and hydrogen storage capacity (right) between complete 3D model (Case C) and reduced 2D model (Case F) for coiled-tube heat exchanger with different numbers of coil turns.

Fig.4.7 shows the comparison of simulation results, including the average temperature and the hydrogen storage capacity, between the reduced 2D model and the complete 3D model for the reactor with a coiled-tube heat exchanger under a different number of coil turns. The average temperatures of the reduced 2D model are slightly higher than those of the complete 3D model. This is due to that the reduced 2D model has slightly smaller heat transfer surface area than the complete 3D model when the spiral coiled-tubes simplified to parallel ring tubes. The hydrogen storage capacities of the reduced 2D model agree well with those of the 3D model. In general, the effectiveness of the reduced 2D model has been validated by the complete 3D model. The reduced 2D model can well approximate the complete 3D model for the case with more turns of coiled-tube.

4.4 Conclusion

The two-dimensional axisymmetric model is developed on the Comsol platform in order to study the thermal effects of the metal hydride hydrogen storage system. The model is validated by comparing its simulation results with other works. The straight pipe heat exchanger and the coiled-tube heat exchanger are taken into consideration in the design of the metal hydride reactor. The complex 3D models are used to study the metal hydride reactor equipped with the coiled-tube heat exchanger. It is an effective method to improve the hydrogen storage efficiency of the metal hydride reactor by equipping with heat exchanger. The coiled-tube heat exchanger presents better heat transfer performance than the straight pipe heat exchanger. Dual heat exchangers, including the combination of the coiled-tube heat exchanger and straight pipe heat exchanger and the dual coiled-tube heat exchangers, are discussed. It takes relatively little time to reach the saturated situation in the reactor equipped with dual coiled-tube heat exchangers. As for the metal hydride hydrogen storage reactor equipped with the coiled-tube heat exchanger, the reduced 2D model is taken into consideration in order to decrease the computing time. The effectiveness has been validated by comparing the simulation results of the reduced model with those of the complete three-dimensional model. The reduced 2D model can well approximate the complete 3D model for the case with more turns of coiled-tube.

Chapter 5 Hydrogen Storage based on Metal Hydride with Phase Change Materials

This section has been published in: Tong L, Xiao J S, Bénard P, et al. Thermal management of metal hydride hydrogen storage reservoir using phase change materials. International Journal of Hydrogen Energy, 2019, 38(44):21055-21066.
My specific contributions in this work was to combine metal foam with phase change material to increase effective thermal conductivity and improve hydrogen storage efficiency in metal hydride system.

Phase change materials can be applied to the metal hydride hydrogen storage system in order to improve system performance. The phase change materials can be used as a kind of heat exchanger to store the heat released during hydriding and provide the heat to a metal hydride bed during dehydriding. In this research, we have developed a new system combining metal hydride, phase change materials and metal foam. The external size of phase change material (PCM) zone is studied by well-validated model. Metal foam (MF) is composited into PCM to increase effective thermal conductivity. Metal hydride (MH) thermally coupled with MF composited PCM forms MF-PCM-MH system. The MF-PCM-MH system shows improved heat transfer and hydrogen storage efficiency. Copper foam shows better performance of MF-PCM-MH system than that with aluminium.

5.1 Mathematical model

The metal hydride hydrogen storage system equipped with phase change exchanger mainly includes the metal hydride bed zone and the phase change material zone. The effect of the reactor wall on the system is neglected for simplification. The mathematical model for metal hydride zone has been presented in the previous section. The mathematical model for the phase change material zone is presented as follows. The commercial paraffin RT35 is used as the phase change material. The convection of the liquid phase change materials is negligible. The energy conservation equation

for the phase change materials is written as

$$\left(\rho c_p\right)_{\text{eff,PCM}} \frac{\partial T}{\partial t} = \nabla \cdot \left(k_{\text{eff,PCM}} \nabla T\right) \tag{5.1}$$

The phase change materials change from solid phase to liquid phase when it stores the reaction heat during hydriding. The metal foam can be used to increase the effective thermal conductivity of the system. The effective thermal conductivity $k_{\text{eff,PCM}}$ can be calculated by Eq.(5.2a) for the case without metal foam and Eq.(5.2b) for the case with metal foam.

$$k_{\text{eff,PCM}} = \left(1-\theta\right) k_{\text{solid,PCM}} + \theta k_{\text{liquid,PCM}} \tag{5.2a}$$

$$k_{\text{eff,PCM}} = \left(1-\varepsilon_{\text{foam}}\right) k_{\text{foam}} + \varepsilon_{\text{foam}} \left[\left(1-\theta\right) k_{\text{solid,PCM}} + \theta k_{\text{liquid,PCM}}\right] \tag{5.2b}$$

The effective heat capacity of the phase change material zone $\left(\rho c_p\right)_{\text{eff,PCM}}$ in Eq.(5.1) is related to the heat capacities of the phase change materials and the metal foam, which can be calculated by Eq.(5.3a) for the case without metal foam and Eq.(5.3b) for the case with metal foam.

$$\left(\rho c_p\right)_{\text{eff,PCM}} = \left(1-\theta\right) \rho_{\text{solid,PCM}} c_{p,\text{solid,PCM}} + \theta \rho_{\text{liquid,PCM}} c_{p,\text{liquid,PCM}} + \rho_{\text{PCM}} L \frac{\partial a}{\partial T} \tag{5.3a}$$

$$\left(\rho c_p\right)_{\text{eff,PCM}} = \left(1-\varepsilon_{\text{foam}}\right) \rho_{\text{foam}} c_{p,\text{foam}} +$$

$$\varepsilon_{\text{foam}} \left[\left(1-\theta\right) \rho_{\text{solid,PCM}} c_{p,\text{solid,PCM}} + \theta \rho_{\text{liquid,PCM}} c_{p,\text{liquid,PCM}} + \rho_{\text{PCM}} L \frac{\partial a}{\partial T}\right] \tag{5.3b}$$

where L means the latent heat from the solid phase to the liquid phase, θ is the melting fraction, the density of phase change materials ρ_{PCM} can be written as $\left(1-\theta\right) \rho_{\text{solid,PCM}} + \theta \rho_{\text{liquid,PCM}}$ and the variable a is defined as $\left[\theta \rho_{\text{liquid,PCM}} - \left(1-\theta\right) \rho_{\text{solid,PCM}}\right] / \left(2 \rho_{\text{PCM}}\right)$ [44]. The last term in Eq.(5.3a) and Eq.(5.3b) can be described as the distribution of latent heat, which is equal to 0 before transformation and after transformation.

5.2 Model parameters

The metal hydride hydrogen storage reactor equipped with phase change materials is

simplified as a two-dimensional axisymmetric model. Fig.5.1 showed the diagram (a) and computational mesh (b) of the metal hydride hydrogen storage system. The computational domain includes the metal hydride zone and the phase change material zone. The phase change material zone has been divided into two sections in order to simplify the mesh generation. The radius and the height of the metal hydride bed are 0.02 m and 0.06 m, respectively. As for the total reservoir, the radius and the height are 0.045 m and 0.08 m, respectively.

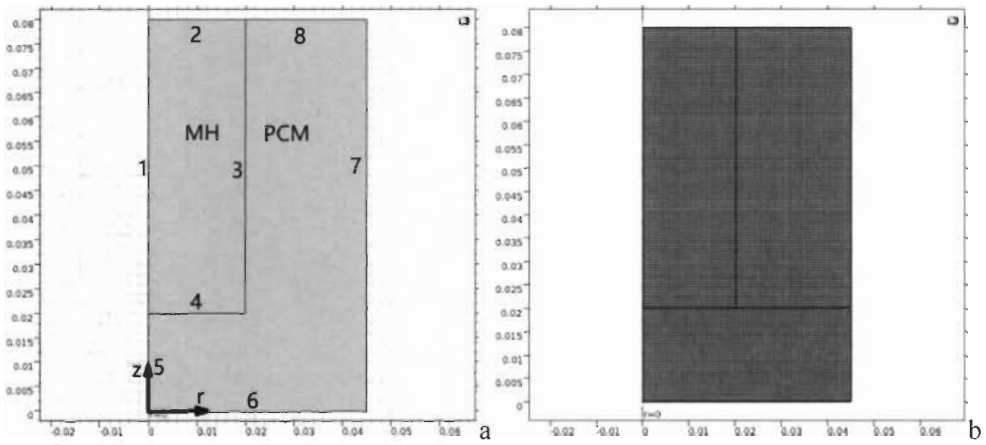

Fig.5.1 Diagram (a) and finite element mesh (b) of metal hydride hydrogen storage reactor with phase change materials.

The parameters of metal hydride, hydrogen, phase change materials and metal foam properties used in the simulation of the hydrogen storage system are shown in Table 5.1 [24, 25, 43, 50]. The commercial paraffin RT35 is selected as the phase change material, its melting temperature is 308.15K and the range of transition temperature is 3K.

The metal hydride reactor is surrounded by phase change materials. The boundary 2 is an inlet and set as the pressure boundary condition. The initial pressure in the reservoir is 0.143MPa. The initial temperature in the tank is assumed as 293K. We suppose that the pressure increases linearly from an initial pressure to constant pressure (0.8MPa) in the first 100s, and maintains at the constant pressure[25] . The boundary 1 and 5 are both set as the symmetric axis. The boundary 6, 7 and 8 are set as thermal insulation condition.

5.3 Results and discussions

5.3.1 Performance of metal hydride reservoir with phase change materials

The model for metal hydride tank without phase change material was validated in the previous section. Performances of metal hydride reservoir using phase change materials were predicted in this section. Fig.5.2 showed the evolution of hydrogen storage capacity of metal hydride bed and the melting fraction of phase change materials (a) and the average temperature of the metal hydride bed and the phase change materials (b). These average values were calculated based on the surface average method. The heat transferred from the metal hydride bed to the phase change materials, the average temperature of metal hydride bed decreased and the average temperature of phase changer materials increased, then the phase change materials transformed from solid phase to liquid phase. At last, the average temperature of metal hydride bed and phase change materials tended to be the same value.

Fig.5.3 presented the distribution of the temperature (a, d, g, j), the density of metal hydride bed (b, e, h, k) and the melting fraction of phase change materials (c, f, i, l) at 500s (a, b, c), 2500s (d, e, f), 9000s (g, h, i) and 30000s (j, k, l). In Fig.5.3a, 5.3d and 5.3g, the red zone means a relatively high temperature area and the blue zone means relatively low temperature area. The heat transferred from a high-temperature zone to a low-temperature zone, and the temperature of each position tended to be the same finally in Fig.5.3j. In Fig.5.3b, 5.3e and 5.3h, the density of the peripheral area near the phase change materials was higher than those of the central region. In other words, the density of metal hydride bed in the high-temperature area was less than that in the low-temperature area. In Fig.5.3c, 5.3f, 5.3i and 5.3l, the red zone can be regarded as the liquid phase. The reaction heat released during hydriding transferred from the metal hydride bed to the phase change materials. When the phase change materials in solid-state absorbed the heat, its temperature increased up to the melting point. Then the phase change materials transformed from the solid state to the liquid state, and its temperature was almost constant during the transformation. The phase change materials in the liquid state continued to absorb the heat and its temperature increased up to the temperature equilibrium state. Finally, the whole phase change materials were in a liquid state, and the temperature difference between metal hydride bed and phase change materials tended to be zero.

5.3.2 Effects of thermal conductivity, mass and latent heat of phase change materials on hydrogen storage performance

The effects of the thermal conductivity, the mass and the latent heat of fusion of the phase change materials on the metal hydride system were studied. The value of thermal conductivity of phase change materials was increased up to its 5, 10 and 15 times (about 1W/m/K, 2 W/m/K and 3 W/m/K) for parametric studies. The phase change materials can be composited with various metal foams in order to increase its effective thermal conductivity. The mass of phase change materials around metal hydride bed is related to its external sizes. In Table 5.2, the external sizes in five cases were presented. The mass of phase change materials was calculated based on the formula of cylindrical volume and its external sizes. As for given phase change materials, the latent heat of fusion is constant. There were four cases with the different latent heat of fusion (increased by about 50 kJ/kg in turn) in the parametric studies. Based on these results, an appropriate phase change material can be selected in future research.

Table 5.1 Properties of materials used in simulation

Parameter	Values	Parameter	Values	Parameter	Values
c_p [J/kg/K]	14890	$\rho_{solid,PCM}$ [kg/m^3]	880	ρ_{Al} [kg/m^3]	2700
c_s [J/kg/K]	419	$\rho_{liquid,PCM}$ [kg/m^3]	760	$c_{p,Al}$ [J/kg/K]	963
k_s [W/m/K]	2.4	$c_{p,solid,PCM}$ [J/kg/K]	1800	L [kJ/kg]	157
k_g [W/m/K]	0.1815	$c_{p,liquid,PCM}$ [J/kg/K]	2400	ρ_{Cu} [kg/m^3]	8920
R [J/mol/K]	8.314	$k_{liquid,PCM}$ [W/m/K]	0.2	k_{Cu} [W/m/K]	400
$c_{p,Cu}$ [J/kg/K]	383	$k_{solid,PCM}$ [W/m/K]	0.2	k_{Al} [W/m/K]	121.1

Table 5.2 Parameters of the system equipped with different mass of phase change materials

Case	r_{MH} [m]	h_{MH} [m]	m_{LaNi5} [kg]	r_{PCM} [m]	h_{PCM} [m]	m_{PCM} [kg]	$m_{LaNi5}/(m_{LaNi5}+m_{PCM})$
1	0.02	0.06	0.27	0.04	0.075	0.265	0.504
2	0.02	0.06	0.27	0.0425	0.0775	0.321	0.457
3	0.02	0.06	0.27	0.045	0.08	0.382	0.414
4	0.02	0.06	0.27	0.0475	0.0825	0.448	0.376
5	0.02	0.06	0.27	0.05	0.085	0.521	0.341

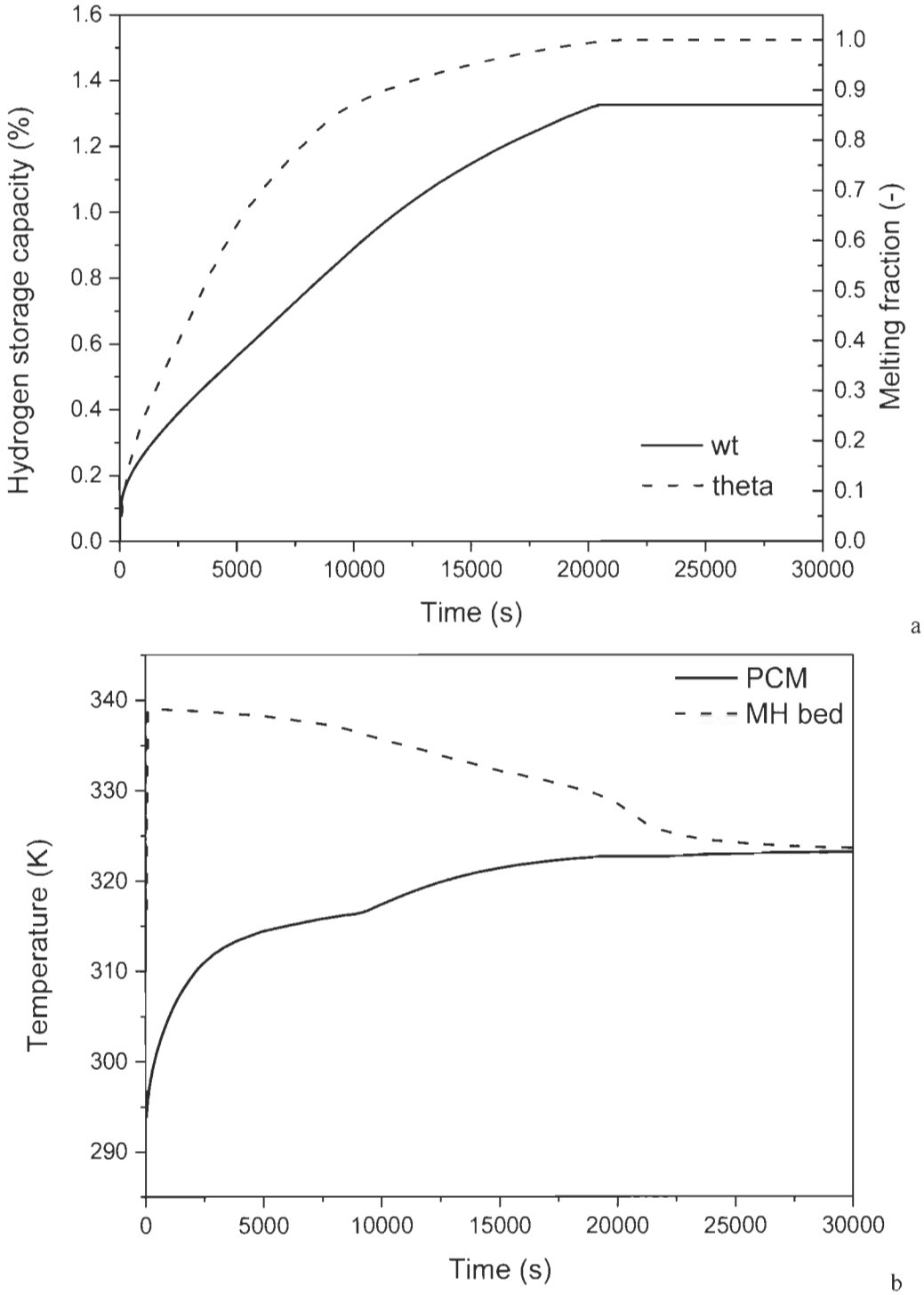

Fig.5.2 Evolution of the hydrogen storage capacity and the melting fraction(a) and the average temperature of metal hydride bed and phase change materials (b).

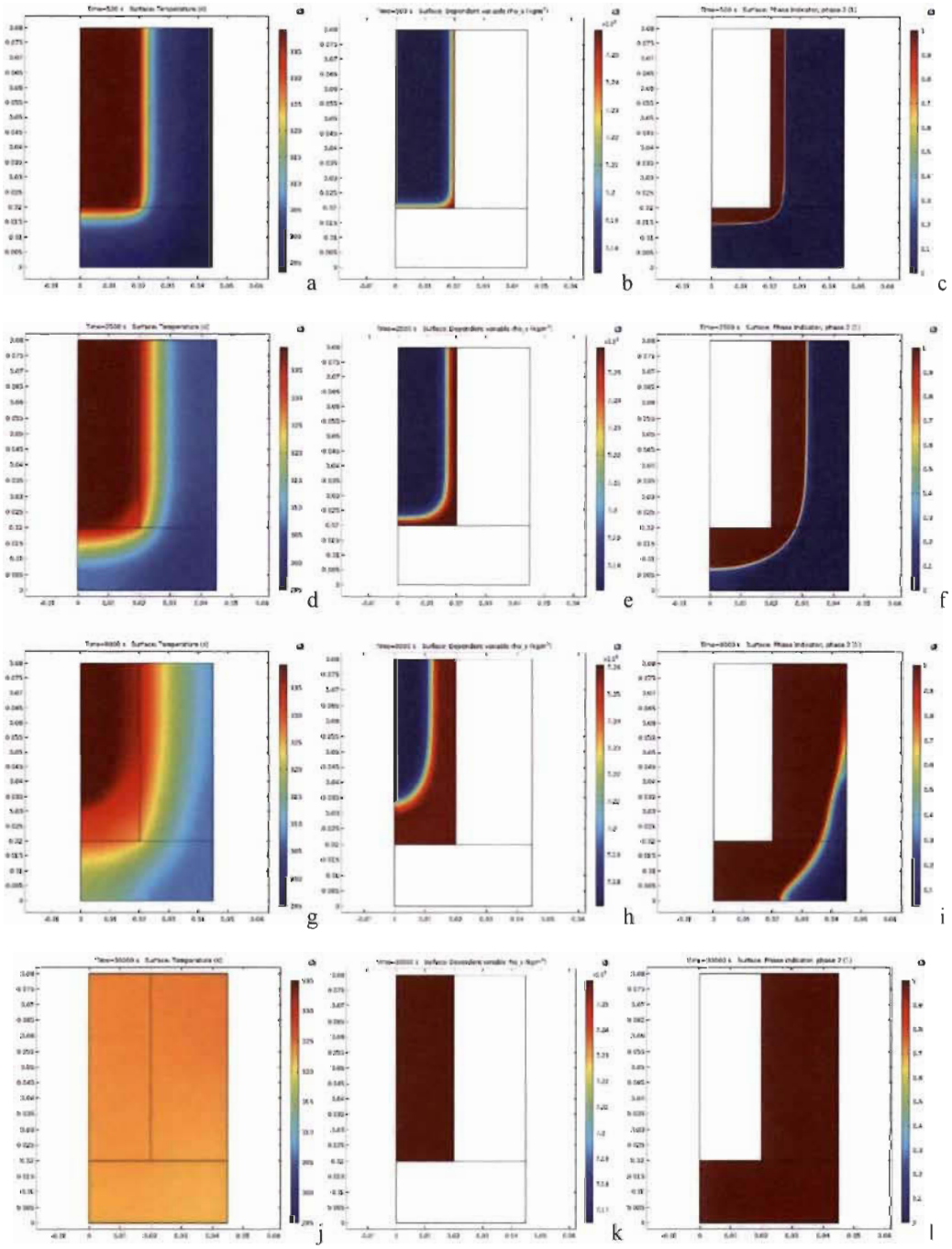

Fig.5.3 Distribution of the temperature(a, d, g, j), the density of metal hydride bed(b, e, h, k) and the melting fraction of phase change materials(c, f, i, l) at 500s(a, b, c), 2500s(d, e, f), 9000s(g, h, i) and 30000s(j, k, l).

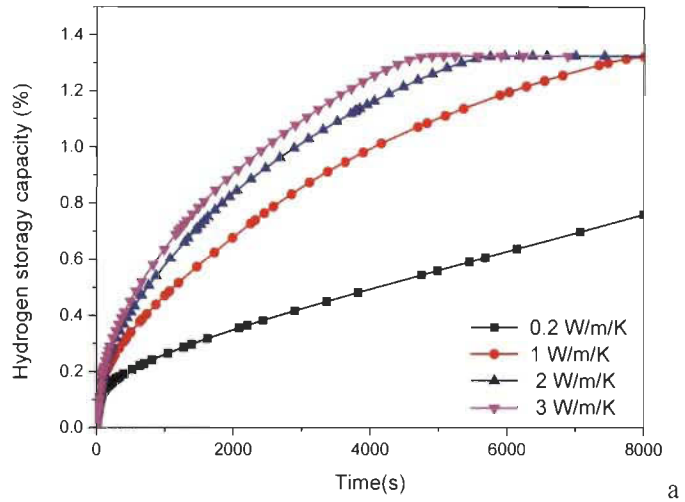

a

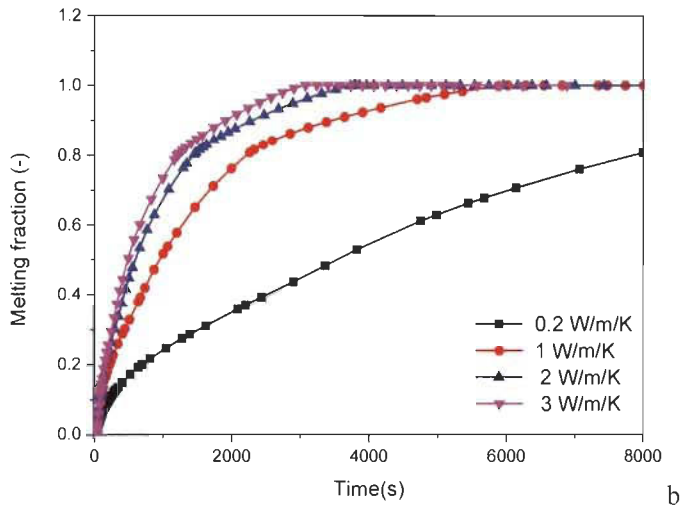

b

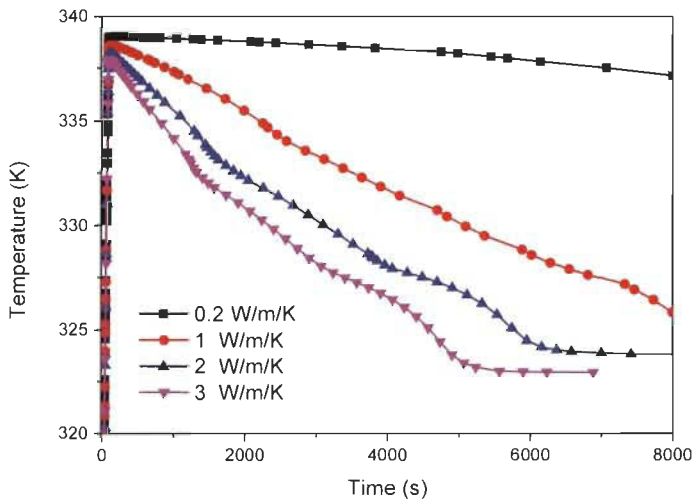

c

Fig.5.4 Effect of thermal conductivity on hydrogen storage capacity (a) and melting fraction (b) and average temperature of metal hydride bed (c).

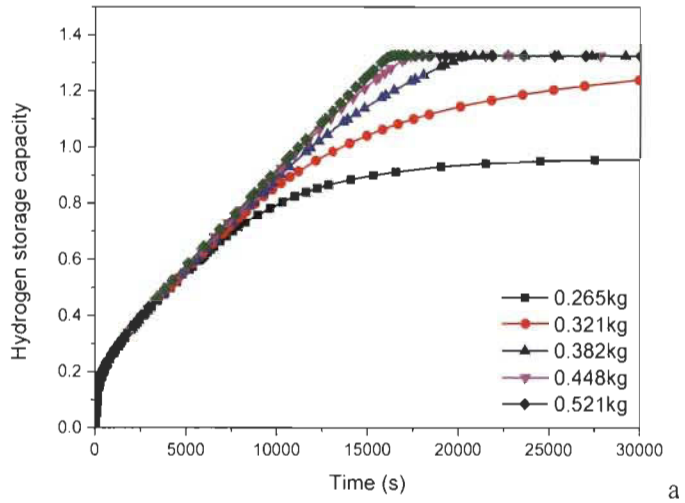

a

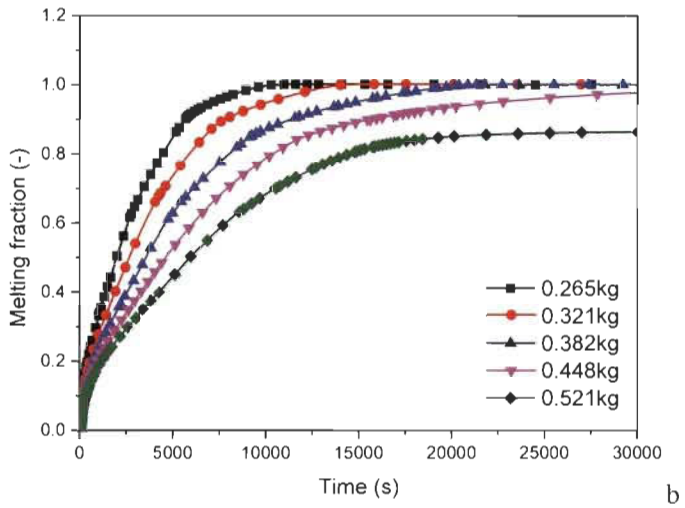

b

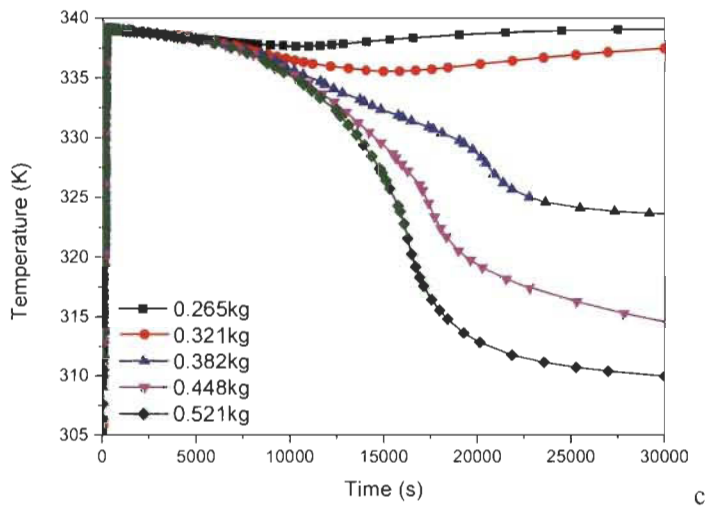

c

Fig.5.5 Effect of the mass of phase change materials on hydrogen storage capacity (a) and melting fraction (b) and average temperature of metal hydride bed (c).

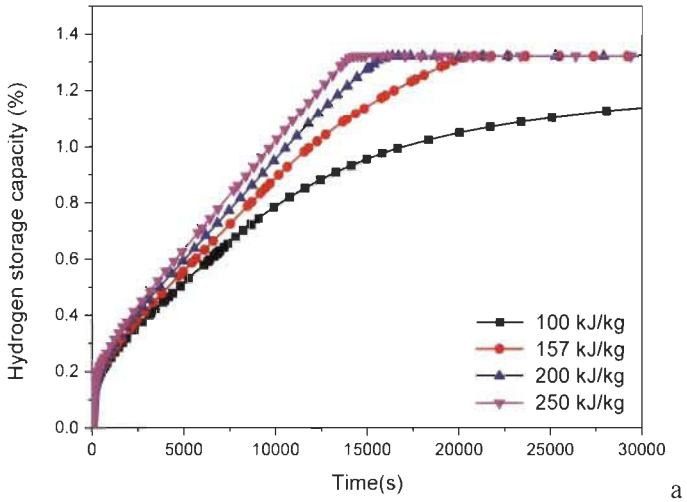

a

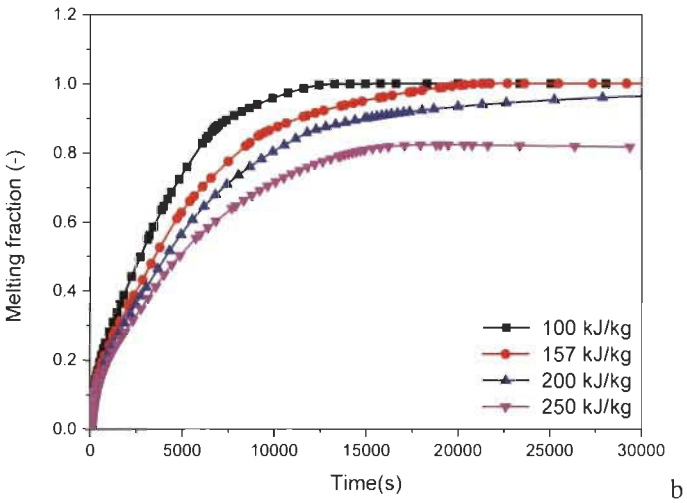

b

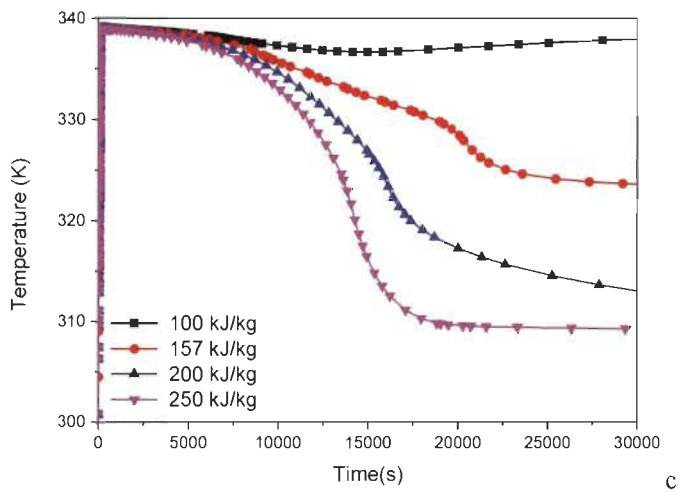

c

Fig.5.6 Effect of the latent heat of fusion on hydrogen storage capacity (a) and melting fraction (b) and average temperature of metal hydride bed (c).

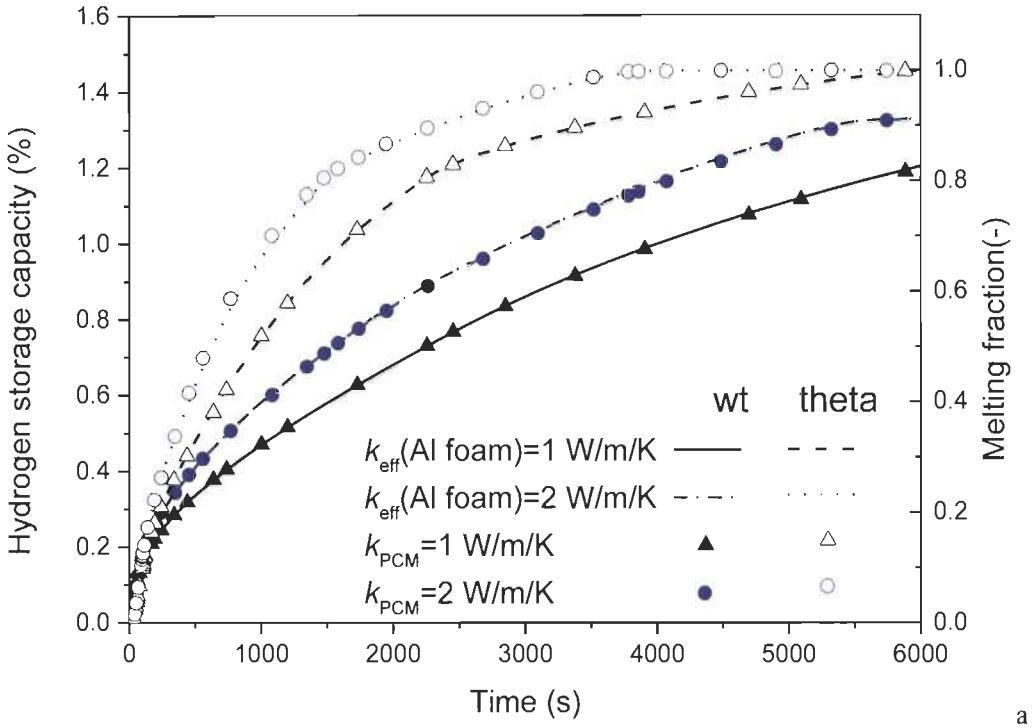

a

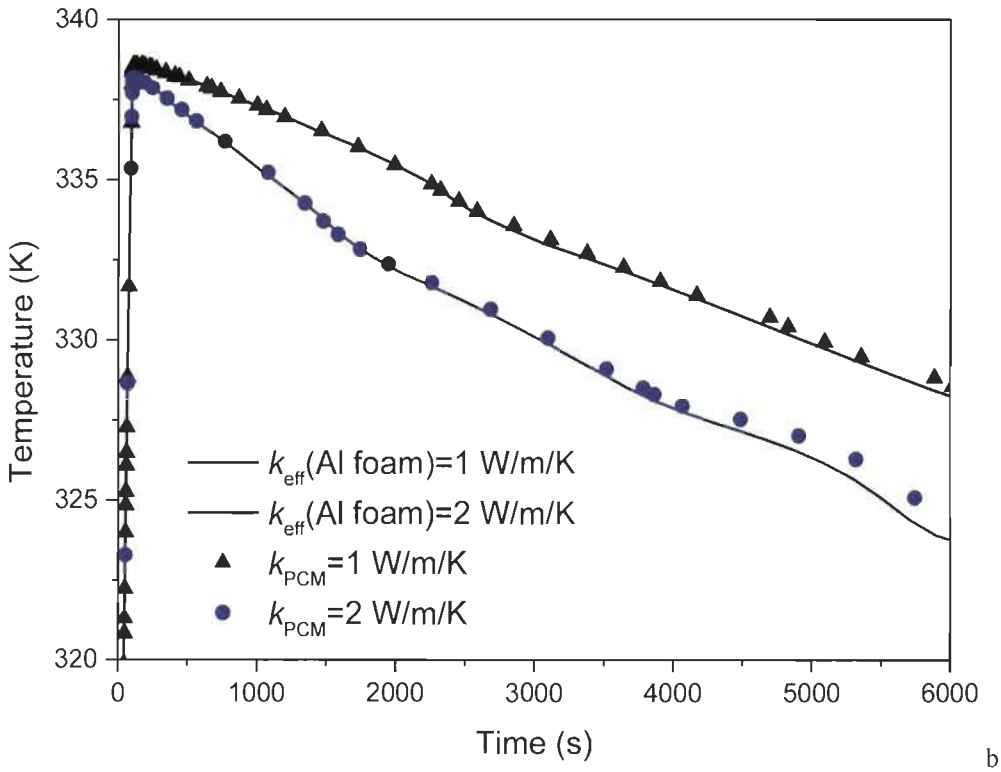

b

Fig.5.7 Effect of Al foam on hydrogen storage capacity and melting fraction (a) and average temperature of metal hydride bed (b).

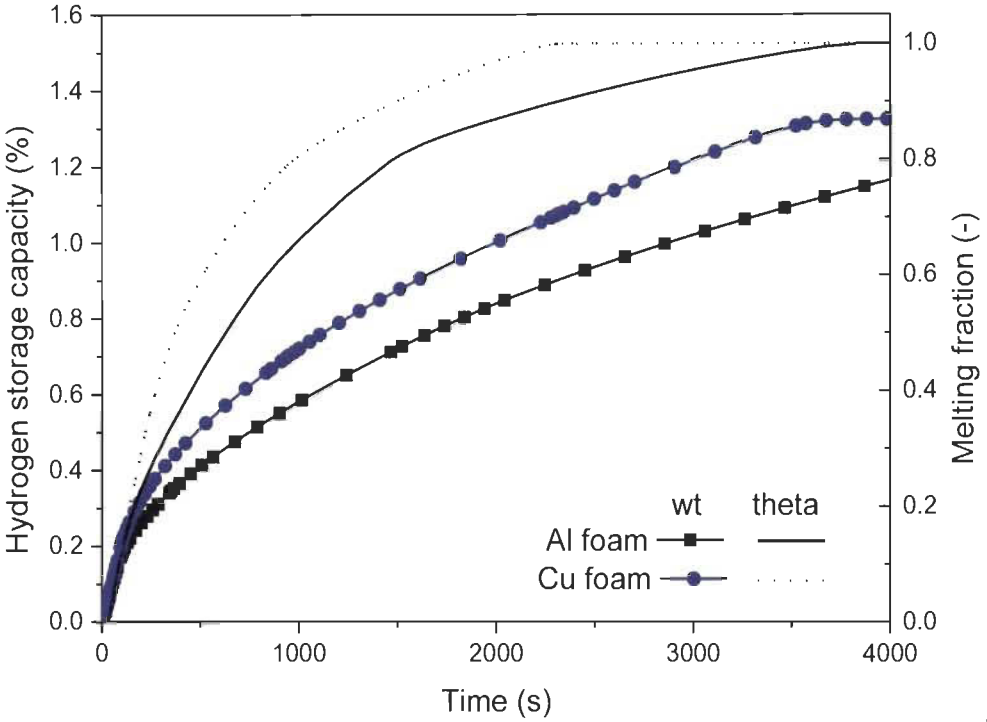

a

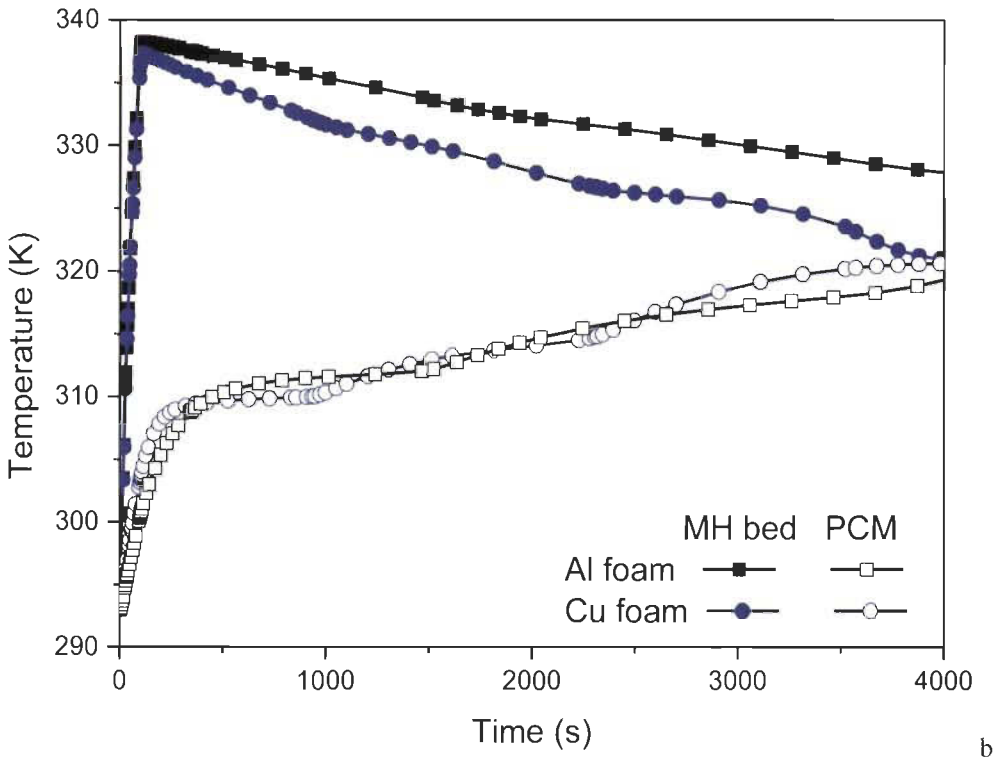

b

Fig.5.8 Effect of different metal foams on hydrogen storage capacity and melting fraction (a) and average temperature of metal hydride bed and phase change materials (b).

Fig.5.4 showed the effect of the thermal conductivity of phase change materials on the hydrogen storage capacity of metal hydride bed (a) and the melting fraction of phase change materials (b) and the average temperature of metal hydride bed (c). It takes relatively little time to reach the limited hydrogen storage capacity of metal hydride bed with relatively large thermal conductivity of phase change materials.

Some metal hydride reservoirs equipped with different qualities of phase change materials were studied. The results showed that the mass of phase change materials had a significant influence on the system performance in Fig.5.5. The hydrogen storage capacity rose and the melting fraction decreased with the increase of mass of phase change materials in Fig.5.5a and Fig.5.5b. The greater the mass of phase change materials, the larger quantity of heat energy it can store. When the hydrogen storage capacity of the metal hydride bed reached to the saturated situation, the average temperature of metal hydride bed was relatively low in the case with a relatively great mass of phase change materials in Fig.5.5c. The mass of phase change materials should be carefully designed in order to optimize the system.

In order to study the effect of the latent heat of fusion on the system, the variation of the hydrogen storage capacity, the melting fraction and the average temperature of metal hydride bed were presented in Fig.5.6. The hydrogen storage capacity rose and the average temperature of metal hydride bed decreased with the increase of the latent heat of fusion. It is a feasible method to improve the system efficiency by selecting the phase change materials with the relatively large latent heat of fusion.

5.3.3 Thermal management using phase change materials composited with metal foam

It is difficult to change the physical properties of the phase change materials, such as the thermal conductivity and the latent heat of fusion. However, we can improve the heat transfer performance of the system by equipping the metal foam in the phase change heat exchanger. Assuming the effective thermal conductivity was set as the same value, the performance of the case with Al foam was compared with the other where the thermal conductivity was set as 1W/m/K or 2W/m/K directly. In Fig.5.7, the cases equipped with the Al foam showed a similar performance as the others. It is a good way to increase the effective thermal conductivity of the phase change material

zone by means of metal foam. Phase change materials composited with metal foam can be used to improve the hydrogen storage efficiency of the metal hydride reservoir.

The physical properties of various metal foams are different, which have influences on the effective thermal conductivity and the effective heat capacity of the composited phase change materials. Fig.5.8 presented the effects of different metal foams on hydrogen storage capacity and the melting fraction (a) and the average temperature of metal hydride bed and phase change materials (b). We supposed the foam porosity was set as the same value. It took relatively little time to reach the saturated situation of the metal hydride bed in the case equipped with copper foam. The copper foam showed better heat transfer performance than that of the Al foam. In the case equipped with copper foam, the phase changes materials could transfer from the solid form to liquid form quickly and the average temperature of metal hydride bed decreases fast.

5.4 Conclusion

In this section, the phase change material heat exchanger composited with the metal foam has been introduced to the hydrogen storage system using metal hydride.

Effects of the thermal conductivity, the mass and the latent heat of phase change materials on the system performance, including the hydrogen storage capacity of metal hydride bed, the melting fraction of phase change materials and the average temperature of the metal hydride bed, were investigated. When the thermal conductivity of phase change materials increased up to 2 W/m/K, the hydrogen storage capacity of metal hydride bed and the melting fraction of phase change materials were improved obviously.

Metal foams, including Al foam and copper foam, were composited with phase change materials in order to increase the effective thermal conductivity of phase change materials and improve the hydrogen storage efficiency of metal hydride reservoir. Compared with the system equipped with Al foam, the system equipped with copper foam showed about 34% improvement of the time when the hydrogen storage capacity reached up to the maximum value.

Chapter 6 Hydrogen Purification using Pressure Swing Adsorption

This section has been submitted to Applied Energy: Tong L, Xiao J S, Bénard P, et al. Optimization of a six-step two-bed pressure swing adsorption system for hydrogen purification based on extended Langmuir-Freundlich isotherm and artificial neural network, Ms. Ref. No.: APEN-D-19-11530.

My specific contributions in this work was to use trained artificial neural network model to optimize the performance of a six-step two-bed pressure swing adsorption system for hydrogen purification.

The pressure swing adsorption cycle is widely used to separate and purify hydrogen from gaseous mixtures. Zeolite 5A is an adsorbent commonly used to separate and purify gas from mixtures. Pure hydrogen can be separated and purified from the coke oven gas (H_2:CH_4:CO:N_2:CO_2=56.4:26.6:8.4:5.5:3.1 mol%) through a pressure swing adsorption process. Hydrogen and methane are the major components in coke oven gas. Hydrogen can be obtained from industrial byproducts, such as the coke oven gas, or produced from a plasma reaction involving methane. The unreacted methane is the major impurity in the gaseous mixture from the plasma reactor [89]. High purity hydrogen is required for use in the fuel cells. In this section, we present a six-step two-bed pressure swing adsorption model which was developed and implemented on the Aspen/Adsorption software platform in order to purify hydrogen from the hydrogen/methane mixture (70/30 mol%).

6.1 Adsorption isotherm and pressure swing adsorption model

6.1.1 Adsorption isotherm

In this work, the extended Langmuir equation fitted from the extended Langmuir-Freundlich isotherm has been used to predict the adsorption isothermal of hydrogen and methane on the zeolite adsorbent bed.

A well-known gas adsorption isotherm is expressed by the Langmuir equation:

$$q^* = \frac{q_m B p}{1 + Bp};\ q_m = k_1 + k_2 T,\ B = k_3 e^{k_4/T} \tag{6.1}$$

where q^* is the amount of adsorption, p is the equilibrium pressure, T is the temperature, k_1, k_2, k_3 and k_4 are the Langmuir isotherm parameters.

Adding an exponent n, which is a function of temperature, to the pressure in Eq.(6.1), the Langmuir equation becomes the Langmuir-Freundlich equation:

$$q^* = \frac{q_m B p^n}{1 + Bp^n};\ q_m = k_1 + k_2 T,\ B = k_3 e^{k_4/T},\ n = k_5 + k_6 / T \tag{6.2}$$

There are totally six isotherm parameters in this model.

Both the Langmuir model and the Langmuir-Freundlich model are used for the adsorption of pure gases. As for the adsorption of gaseous mixtures, we should use the extended Langmuir equation and the extended Langmuir-Freundlich equation, which are presented in Eq.(6.3) and Eq.(6.4), respectively:

$$q_i^* = \frac{q_{mi} B_i p_i}{1 + \sum_{j=1}^{N} B_j p_j},\ i = 1, 2, \ldots, N;\ q_m = k_1 + k_2 T,\ B = k_3 e^{k_4/T} \tag{6.3}$$

$$q_i^* = \frac{q_{mi} B_i p_i^{n_i}}{1 + \sum_{j=1}^{N} B_j p_j}, i = 1, 2, \ldots, N;\ q_m = k_1 + k_2 T,\ B = k_3 e^{k_4/T},\ n = k_5 + k_6 / T \tag{6.4}$$

Where the values of parameters are the same as in the Langmuir and Langmuir-Freundlich equations Eq.(6.1) and Eq.(6.2). The alphabet i means the component in the gaseous mixtures while the alphabet j is a variable in the operation of summing Σ in Eqs (6.3) and (6.4). When the number of components in the gaseous mixture N is reduced to 1 in Eq.(6.3) and (6.4), the extended Langmuir and Langmuir-Freundlich models can be reduced to the Langmuir or Langmuir-Freundlich models, respectively.

The extended Langmuir (EL) equation has been applied to predict the equilibrium amount adsorbed in the pressure swing adsorption model [66, 70, 71, 89]. The extended Langmuir-Freundlich model, also referred to as the loading ratio correlation (LRC) model, is used in the simulation of hydrogen purification pressure swing adsorption process using zeolite 5A as the adsorbent [61, 63-65, 67].

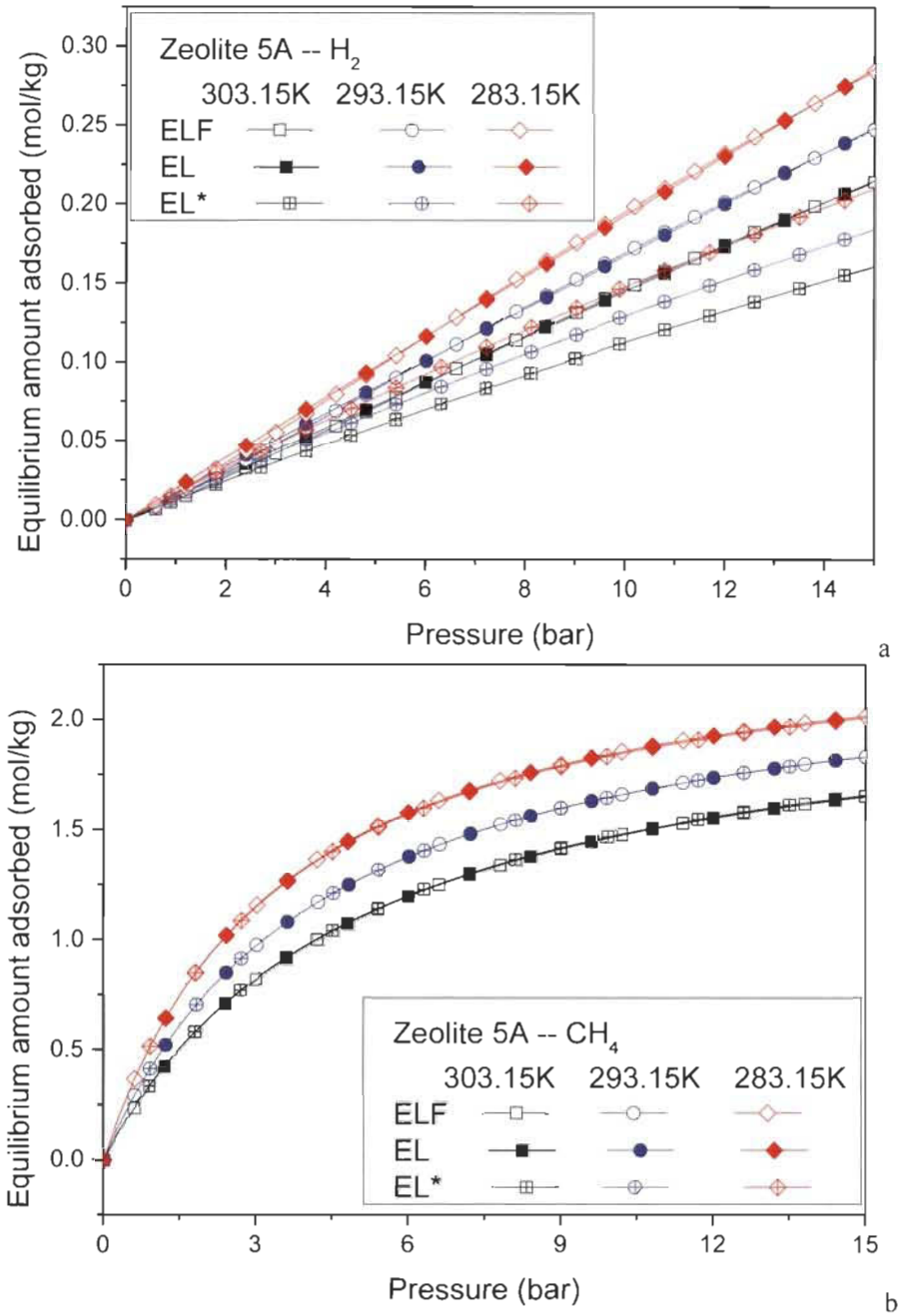

Fig.6.1 Adsorption isotherms comparison between extended Langmuir equation and extended Langmuir-Freundlich equation for H_2 (a) and CH_4 (b) on zeolite 5A adsorbent bed at 283.15K, 293.15K and 303.15K.

ELF: calculated by the extended Langmuir-Freundlich equation based on the parameters from Ref.[67];

EL: calculated by the extended Langmuir equation based on the parameters fitted extended Langmuir-Freundlich equation from Ref.[67];

EL*: calculated by the extended Langmuir equation based on the parameters from Ref.[66].

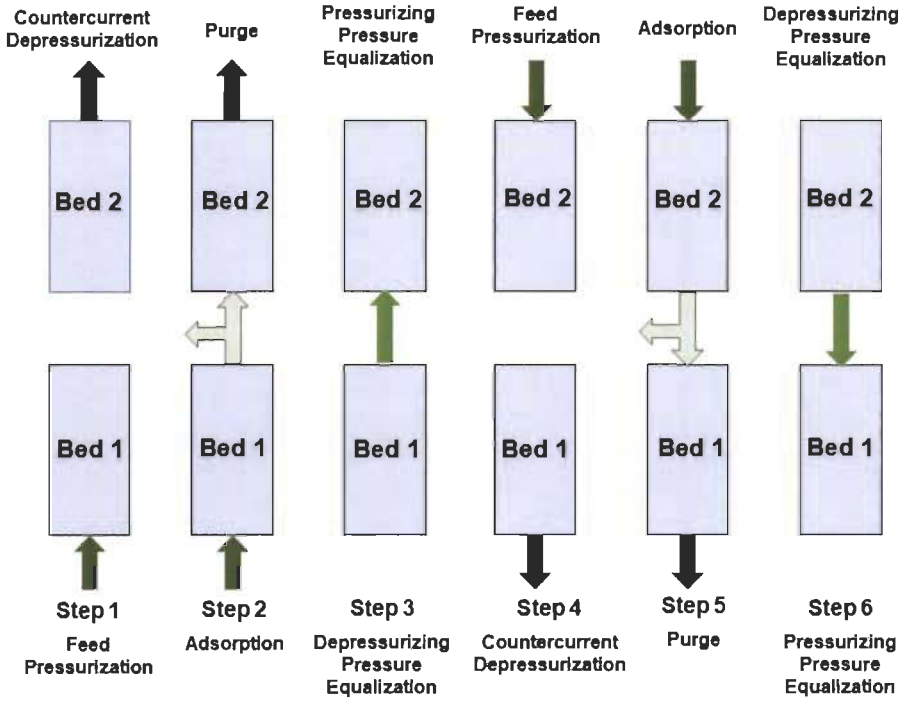

a

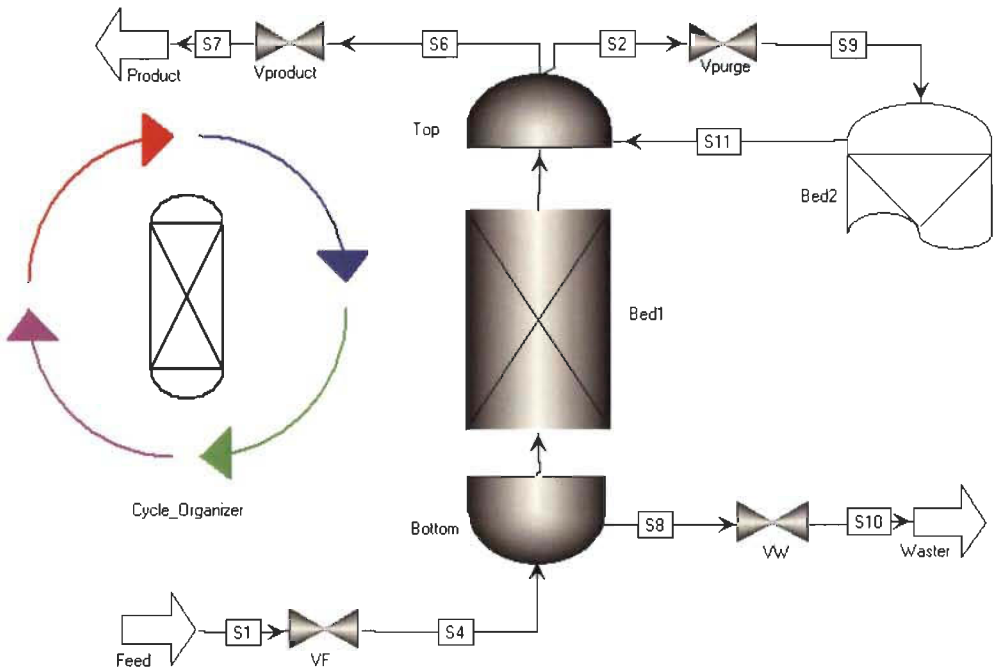

b

Fig.6.2 Process sketch of six-step two-bed pressure swing adsorption process (a) and system diagram of hydrogen purification pressure swing adsorption model (b)

The parameters used in the extended Langmuir-Freundlich (ELF) equation for predicting the equilibrium amount adsorbed of methane on zeolite adsorbent in Ref.[67]

are different from those in Ref.[61]. However, their calculation results of the equilibrium amount adsorbed are almost the same. The extended Langmuir-Freundlich model is unavailable in dynamic simulation on the Aspen/Adsorption software platform, then the extended Langmuir equation is applied in this work. The isotherm parameters used for the extended Langmuir (EL) equation in the hydrogen purification pressure swing adsorption system, which are presented in Table 6.1, are fitted from the adsorption isotherms calculated by the extended Langmuir-Freundlich equation from Ref.[67] based on the Matlab software platform. The extended Langmuir equation used in Ref.[66] is shortened as EL*, their parameters (k_1, k_2, k_3 and k_4) are as the same as those in Ref.[67].

Fig.6.1 shows the adsorption isotherms calculated by the extended Langmuir (EL) equation in present work, the extended Langmuir (EL*) equation in Ref.[66] and the extended Langmuir-Freundlich (ELF) equation in Ref.[67] at different temperatures. As for methane, the values of the term $k_5 + k_6 / T$ in Eq. (6.2) and (6.4) are about 1, thus the calculated results based on the isotherm parameters from Ref.[66] are similar to those from Ref.[67]. In general, the results of the extended Langmuir equation (EL) in the present work agree well with those of the extended Langmuir-Freundlich (ELF) equation for predicting the adsorption amount of hydrogen and methane on the zeolite 5A adsorbent bed.

Table 6.1 Isotherm parameters of extended Langmuir-Freundlich (ELF) equation [67] and fitted isotherm parameters of extended Langmuir (EL) equation for H_2 and CH_4 on zeolite 5A

Model/Gas	k_1	k_2	k_3	k_4	k_5	k_6
	[mol/kg]	[mol/kg/K]	[1/bar]	[K]	[-]	[K]
ELF/H_2	4.314	-0.0106	0.002515	458	0.986	43.03
EL/H_2	28.7	-0.07071	0.0004266	473.3	N/A	N/A
ELF/CH_4	5.833	-0.01192	0.0006507	1731	0.82	53.15
EL/CH_4	6.1	-0.01283	0.0006481	1732	N/A	N/A

6.1.2 Pressure swing adsorption model

Based on mass, momentum and energy conservation equations, extended Langmuir equation and linear driving force model, a hydrogen purification pressure swing

adsorption model has been developed on the Aspen/Adsorption software platform. This validated hydrogen purification model can be used for further optimization of the system performance.

Mass conservation equation is presented as:

$$\varepsilon_b \frac{\partial c_i}{\partial t} + \frac{\partial \left(v_g c_i\right)}{\partial z} = D_L \varepsilon_b \frac{\partial^2 c_i}{\partial z^2} - \rho_b \frac{\partial q_i}{\partial t}, i = 1, 2, \cdots, N \tag{6.5}$$

where ε_b is the porosity of zeolite 5A adsorbent bed, D_L is axial dispersion coefficient, ρ_b is the bed density or bulk density, z is the axial position in adsorption bed and t is the time.

Ergun equation used in the model is shown as:

$$-\frac{dp}{dz} = \frac{150\mu\left(1-\varepsilon_b\right)^2}{d_p^2 \varepsilon_b^3} v_g + 1.75 \frac{\rho_g \left(1-\varepsilon_b\right)}{d_p \varepsilon_b^3} v_g^2 \tag{6.6}$$

where d_p is the particle diameter, μ is the dynamic viscosity, and v_g is Darcy velocity or superficial gas velocity.

The energy conservation equations for the gas phase in the column (Eq. 6.7) , the solid phase in the column (Eq. 6.8) and the column wall (Eq. 6.9) are presented as follows, and the subscripts *g*, *s* and *w* mean the gas phase in the column, the solid phase in the column and the column wall, respectively.

$$\varepsilon_b c_g C_{pg} \frac{\partial T_g}{\partial t} + c_g C_{pg} v_g \frac{\partial T_g}{\partial z} = \varepsilon_b K_g \frac{\partial^2 T_g}{\partial z^2} - p \frac{\partial v_g}{\partial z} + a_p h_{gs} \left(T_s - T_g\right) + \frac{4h_{in}}{d_b} \left(T_w - T_g\right) \tag{6.7}$$

where c_g and C_{pg} are the gas molar fraction and specific heat capacity of the gas phase, respectively, K is the thermal conductivity, h_{in} is the heat transfer coefficient between the gas phase and the column wall.

$$\rho_b C_{ps} \frac{\partial T_s}{\partial t} + \rho_b \sum_{i=1}^{N} \left(C_{pai} q_i\right) \frac{\partial T_s}{\partial t} = K_s \frac{\partial^2 T_s}{\partial z^2} + \rho_b \sum_{i=1}^{N} \left(\Delta H_i \frac{\partial q_i}{\partial t}\right) + a_p h_{gs} \left(T_g - T_s\right) \tag{6.8}$$

where T_g and T_s are the temperature for the gas phase and solid phase in the column, respectively. h_{gs} is the gas-solid heat transfer coefficient.

$$\rho_w C_{pw} \frac{\partial T_w}{\partial t} = K_w \frac{\partial^2 T_w}{\partial z^2} + \frac{4 d_b h_{in} \left(T_g - T_w\right) - 4\left(d_b + 2\delta_w\right) h_{\text{out}} \left(T_w - T_f\right)}{\left(d_b + 2\delta_w\right)^2 - d_b^2} \tag{6.9}$$

where ρ_w and C_{pw} are the density and the specific heat capacity of the column wall, respectively. d_b is the inner diameter of the adsorbent bed, δ_w is the thickness of the column wall, h_{out} is the heat transfer coefficient between the column wall and the ambient environment.

Linear driving force model is:

$$\frac{\partial q_i}{\partial t} = \omega_i \left(q_i^* - q_i\right), i = 1, 2, \cdots, N \tag{6.10}$$

where q^* is the equilibrium adsorption amount, q is the dynamic adsorption amount and ω is the mass transfer coefficient.

The density for gas in the column is written as:

$$\rho_g = \sum_{i=1}^{N} c_i M_i = M \frac{p}{RT} \tag{6.11}$$

where the concentration for each component $c_i = \frac{n_i}{V} = \frac{p_i}{RT}, i = 1, 2, \cdots, N$.

The mass transfer coefficients for hydrogen and methane used in the linear driving force model are 0.587 1/s and 0.049 1/s, respectively. The values of adsorption heat for hydrogen and methane in zeolite 5A adsorbent bed are assumed to be constant, as presented in Table 6.2. The dispersion coefficient for gas is set as 1e-5 m^2/s. The column is assumed to be filled with pure hydrogen at the beginning of the pressure swing adsorption process. The ambient temperature and the initial temperature in the column are set to be about 298K. The heat transfer coefficient between the column wall and the ambient environment is 14.3 $W/m^2/K$. The heat transfer coefficient between gas in the column and the column wall is 36.84 $W/m^2/K$. The initial pressure in the column is equal to the average value of the adsorption pressure and the purge pressure.

The outlet boundary pressure during the purge step is set to be about 1.01 bar. The gas used in the simulation is considered as an ideal gas. Ergun equation is used in the pressure swing adsorption model. More information about the model can be found in our previous works [71, 87, 88].

The hydrogen purification system used in the present work includes two adsorbent beds. The procedures of the pressure swing adsorption cycle in this work consist of six steps, including the feed pressurization step, the adsorption step, the depressurizing pressure equalization step, the depressurization step, the purge step and the pressurizing pressure equalization step. Of course, the cycle sequence of the two adsorbent beds is different, the sketch of the six-step two-bed pressure swing adsorption system is shown in Fig.6.2a. The performances of the two adsorbent beds in the same step of the pressure swing adsorption process are assumed to be the same. Then, we can use one adsorbent bed to simulate this two-bed system. The six-step two-bed pressure swing adsorption cycle model is completed on the Aspen/Adsorption software platform, its diagram of this model is presented in Fig.6.2b.

In this work, the feed rate is set as 2 L/min, about 1.47e-6 kmol/s. The P/F ratio is defined as the ratio of the amount of gas used in the purge step to that used in the adsorption step. In general, the gas used in the purge step is considered as pure hydrogen. The parameters of adsorbent, adsorbate and column wall used in the pressure swing adsorption model are presented in Table 6.2.

The purified hydrogen discharged from the adsorbent bed includes two parts, some is used to purge another adsorbent bed, the rest is the product gas and flows out from the product outlet. The hydrogen purity is defined as the ratio of the amount of hydrogen to the amount of whole gas outflowed from the product outlet during the adsorption step, as shown in Eq. (6.12), where $\dot{n}_{H_2|\,product}$ means the flow rate of hydrogen at the product outlet, i is the index of a component in the gaseous mixture. The hydrogen recovery is defined as the ratio of the amount of hydrogen outflowed from the product outlet during the adsorption step to the amount of hydrogen inflowed from the feed inlet during the feed pressurization step and the adsorption step, as shown in Eq. (6.13).

$$\mathrm{PurH_2} = \frac{\int_0^{t_{adsorption}} \dot{n}_{H_2|\ product}\,dt}{\sum_{i=1}^{N}\int_0^{t_{adsorption}} \dot{n}_{i|\ product}\,dt} \tag{6.12}$$

$$\mathrm{RecH_2} = \frac{\int_0^{t_{adsorption}} \dot{n}_{H_2|\ product}\,dt}{\int_0^{t_{feed}+t_{adsorption}} \dot{n}_{H_2|\ feed}\,dt} \tag{6.13}$$

The hydrogen in the gaseous mixture can not be recovered fully since some hydrogen has been removed from the waster outlet of the hydrogen purification system during the depressurization step and the purge step. The hydrogen recovery is related to the amount of hydrogen flowed into the column during the feed pressurization step and the adsorption step. The pressure in the column increases during the feed pressurization step when the gaseous mixture flows into the hydrogen purification system. When the pressure in the column reaches up to the adsorption pressure at the end of the feed pressurization step, the recovery of the hydrogen purification system is lower 5-10% than that of the cases used in present work, whose pressure at the end of the feed pressurization process is lower than the adsorption pressure in the adsorption process, as shown in Fig.6.3a.

Base on the operation conditions for case 5 presented in Table 6.3, the simulation results of the pressure swing adsorption model, including the hydrogen mole fraction at the outlet in a whole pressure swing adsorption cycle, the gaseous hydrogen fraction and the amount of methane adsorbed along the axial direction of adsorption bed at the end of adsorption step, are compared with other works [61], in order to validate the validity of the PSA model. The hydrogen mole fraction at the outlet includes two parts, the one comes from the product outlet in the adsorption step and the other comes from the waster outlet in the depressurization step and the purge step.

The histories of the pressure and the molar fraction of hydrogen in a pressure swing adsorption cycle are illustrated in Fig.6.3. The simulated data is collected at the 15th pressure swing adsorption cycle, when the hydrogen purification pressure swing adsorption system is considered to be a stable state. Fig.6.3a draws the pressure profile in a whole pressure swing adsorption cycle. Fig.6.3b shows that the hydrogen mole fraction during the adsorption step agreed well with the published data [61]. The

hydrogen mole fraction during the adsorption step is closely connected with hydrogen purity of the pressure swing adsorption cycle. In general, the hydrogen mole fractions during the depressurization step and purge step are in accord with the other work, although its value is slightly bigger than published data at the end of the depressurization step. The gaseous hydrogen fraction and the amount of methane adsorbed along the axial direction of adsorption bed at the end of the adsorption step show the same trend compared with the data from Ref.[61] in Fig.6.4. The difference between the published data and the present work is acceptable. In general, the pressure swing adsorption model has been validated by comparing its simulation results with other work. Further works should be done in order to obtain better results.

6.2 Parametric study of pressure swing adsorption cycle for hydrogen purification

Effects of the adsorption pressure, the P/F ratio, the adsorption step time and the pressure equalization time on the hydrogen purity and the recovery are studied in this section. Various operation conditions used for the parametric study are presented in Table 6.3. The simulation results of these cases are compared with published data from Ref.[61], as shown in Fig.6.5. In general, the simulation results of hydrogen purity and recovery in these cases agree with other work [61].

Table 6.2 Parameters of adsorbent, adsorbate and column wall

Parameter	Value	Parameter	Value
Length of adsorption bed, [m]	1	Heat capacity of zeolite 5A, [J/kg/K]	921
Inner diameter of adsorption bed, [mm]	22	Heat capacity of wall, [J/kg/K]	502.3
Thickness of wall, [mm]	1.75	Heat capacity of H_2, [J/mol/K]	28.878
Thermal conductivity of wall, [W/m/K]	13	Heat capacity of CH_4, [J/mol/K]	36.205
Thermal conductivity of zeolite 5A, [W/m/K]	0.462	Density of wall, [kg/m^3]	7830
Intra-particle voyage of zeolite 5A, [-]	0.6432	Heat of adsorption for methane on zeolite 5A, [J/mol]	22603
Bed porosity of zeolite 5A, [-]	0.357	Heat of adsorption for hydrogen on zeolite 5A,	11720

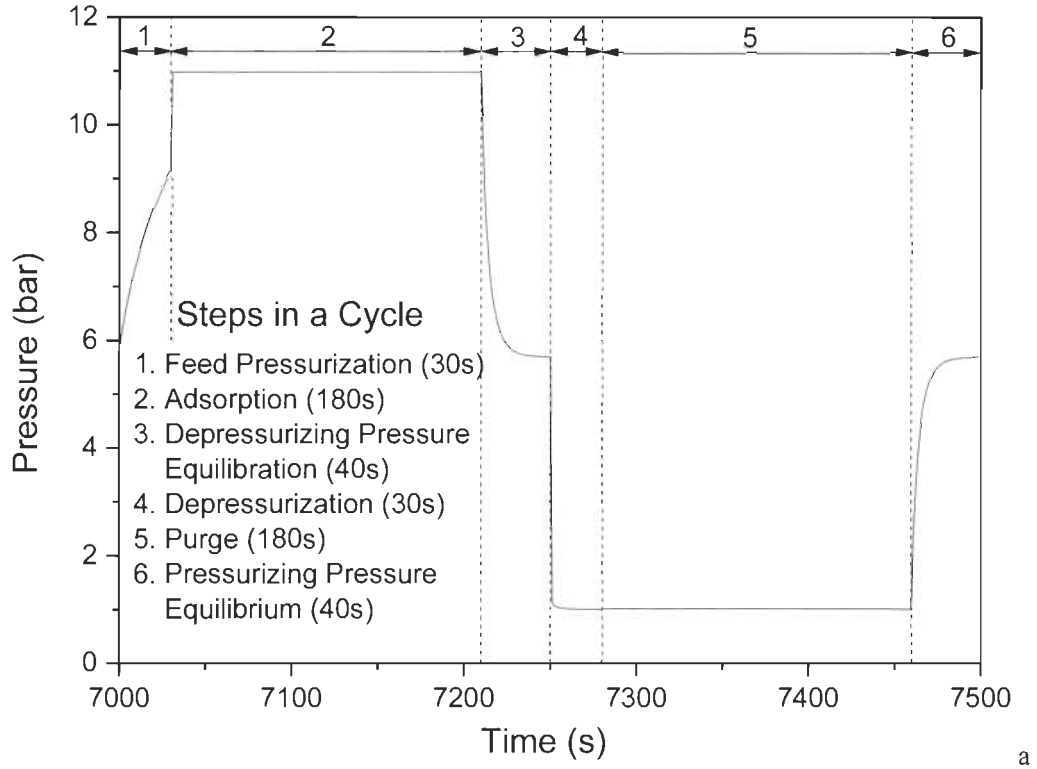

a

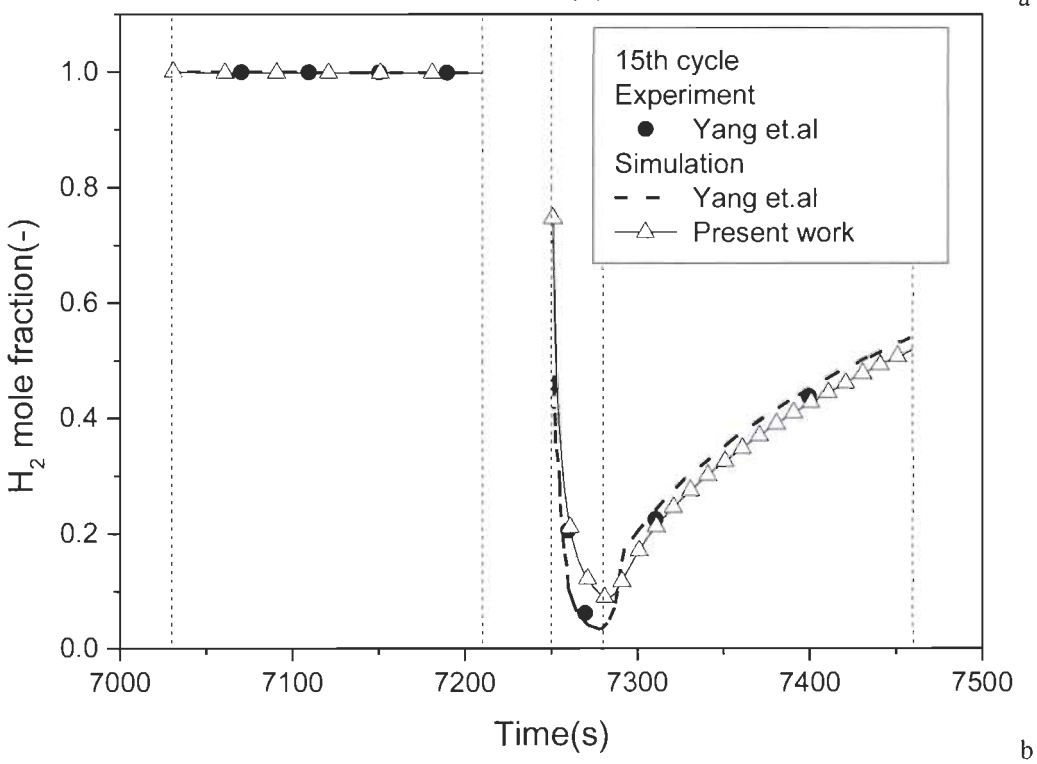

b

Fig.6.3 Pressure profile (a) and H_2 mole fraction of outlet (b) in 15th pressure swing adsorption cycle

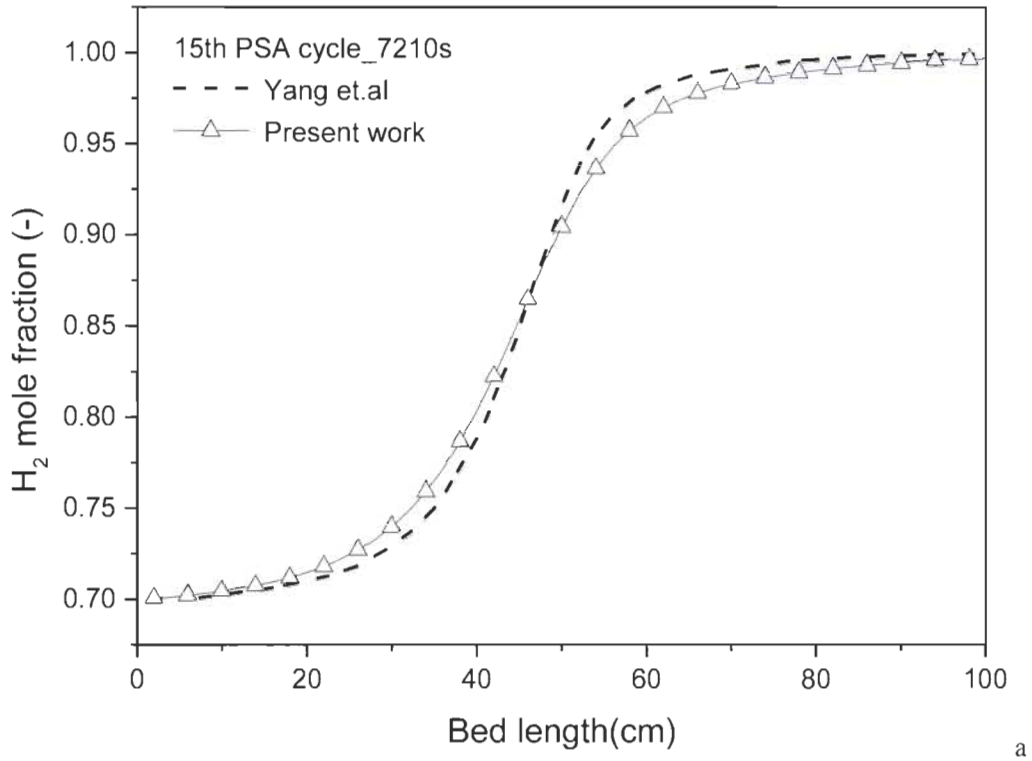

a

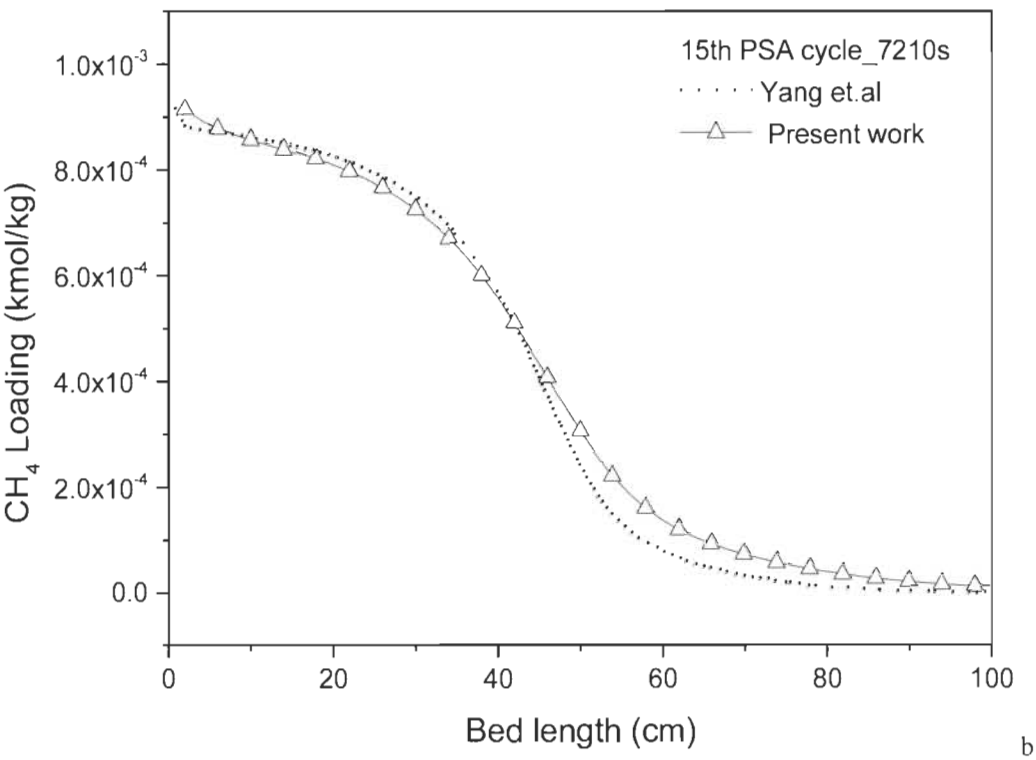

b

Fig.6.4 Axial profiles of the gaseous H_2 mole fraction (a) and the amount of adsorbed CH_4 (b) at the end of adsorption step (about 7210s) in 15th PSA cycle

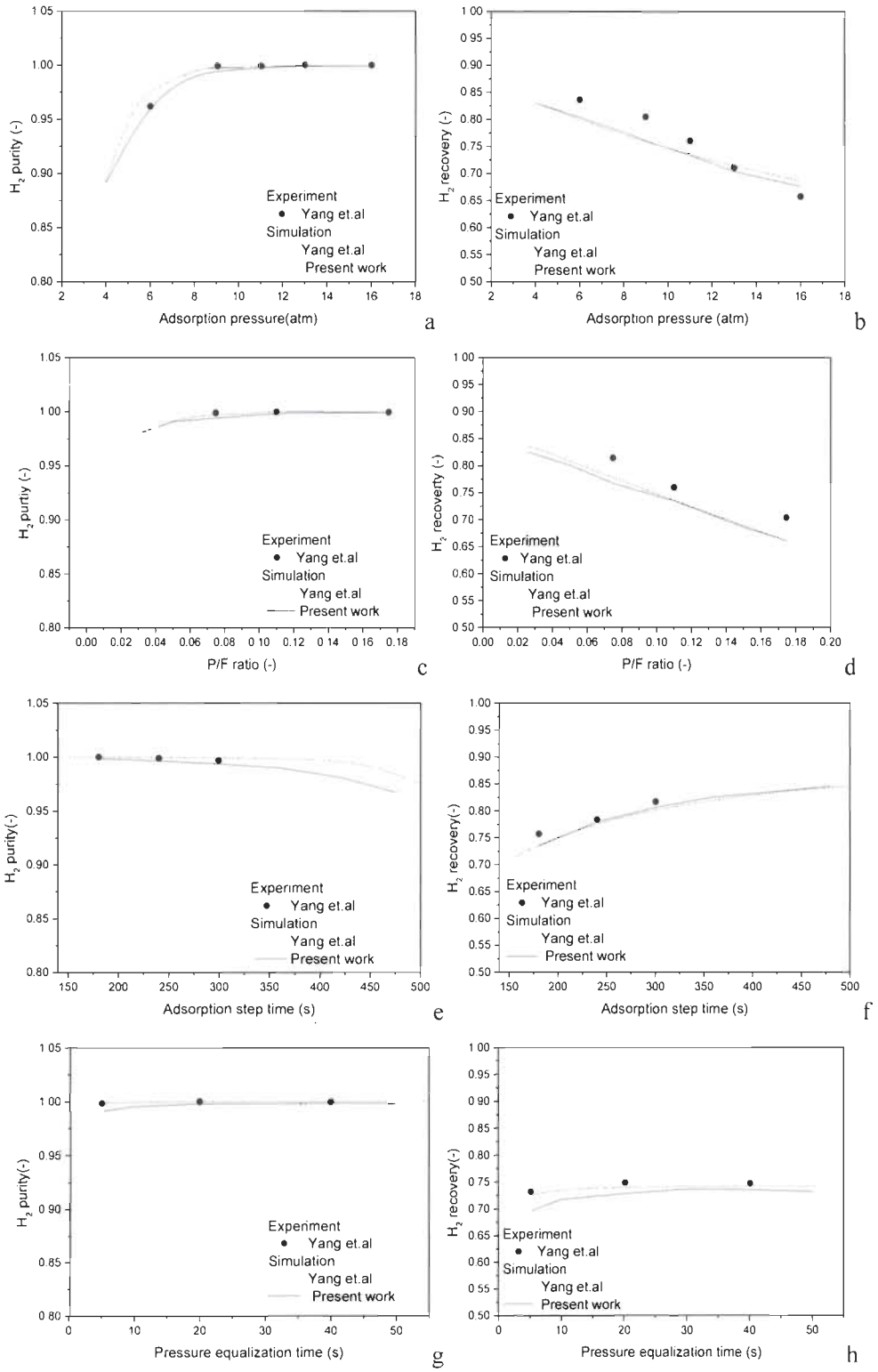

Fig.6.5 Effects of adsorption pressure (a, b), P/F ratio (c, d), adsorption step time (e, f) and pressure equalization time (g, h) on hydrogen purity (a, c, e and g) and recovery ratio (b, d, f and h), published data adopted from Ref.[61]

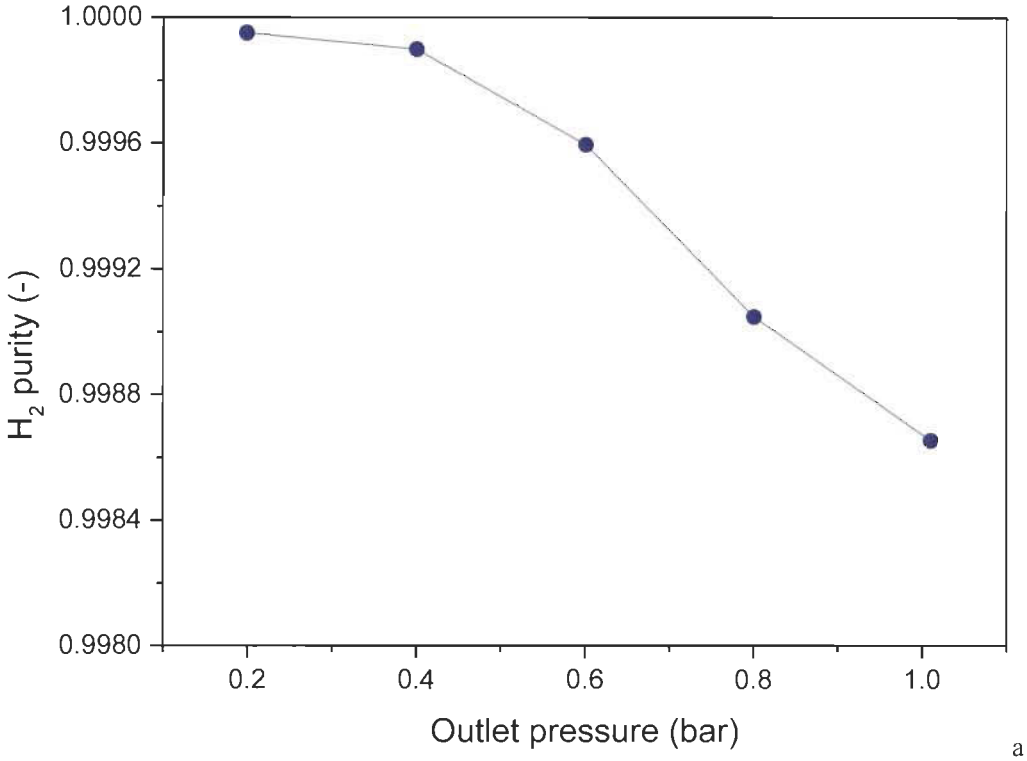

a

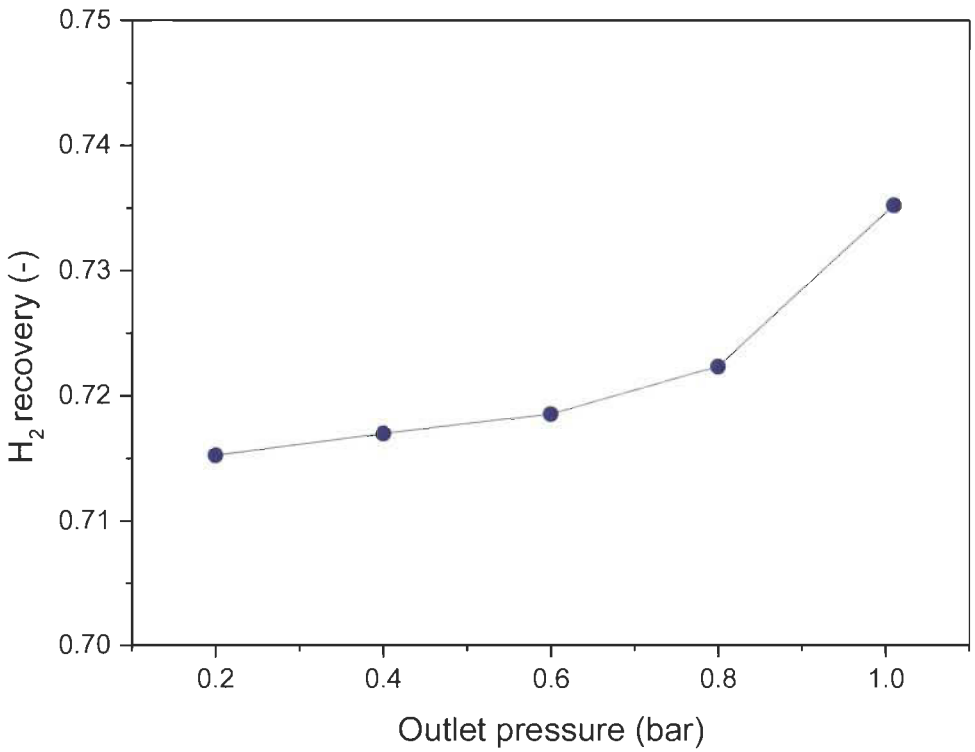

b

Fig.6.6 Effects of outlet pressure at the waster port on hydrogen purity (a) and recovery (b)

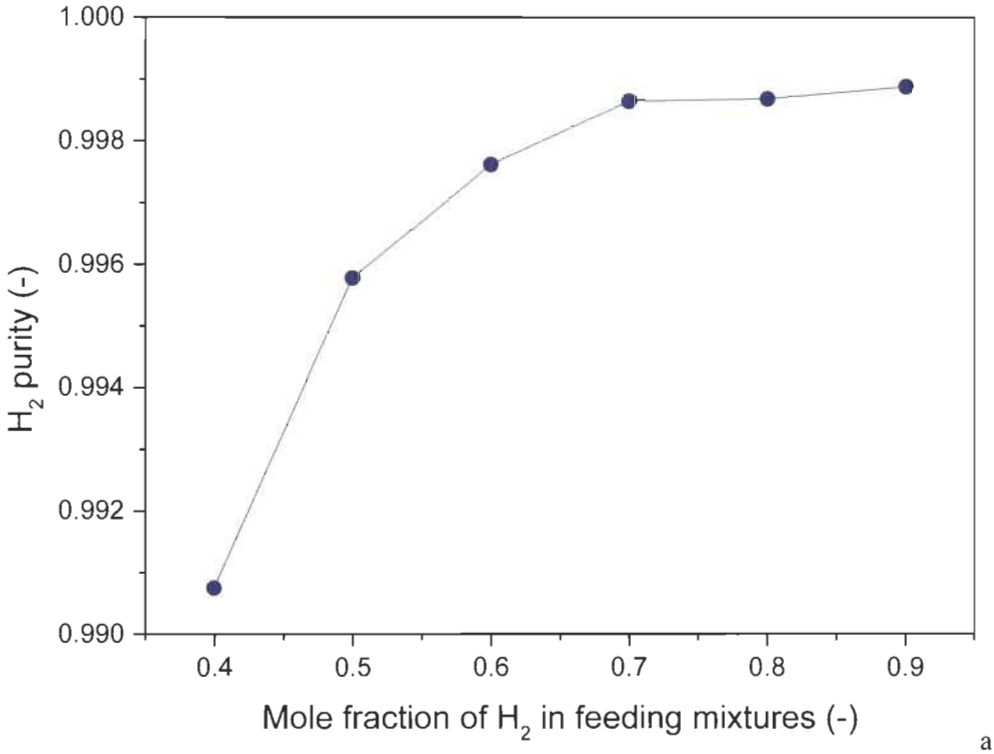

a

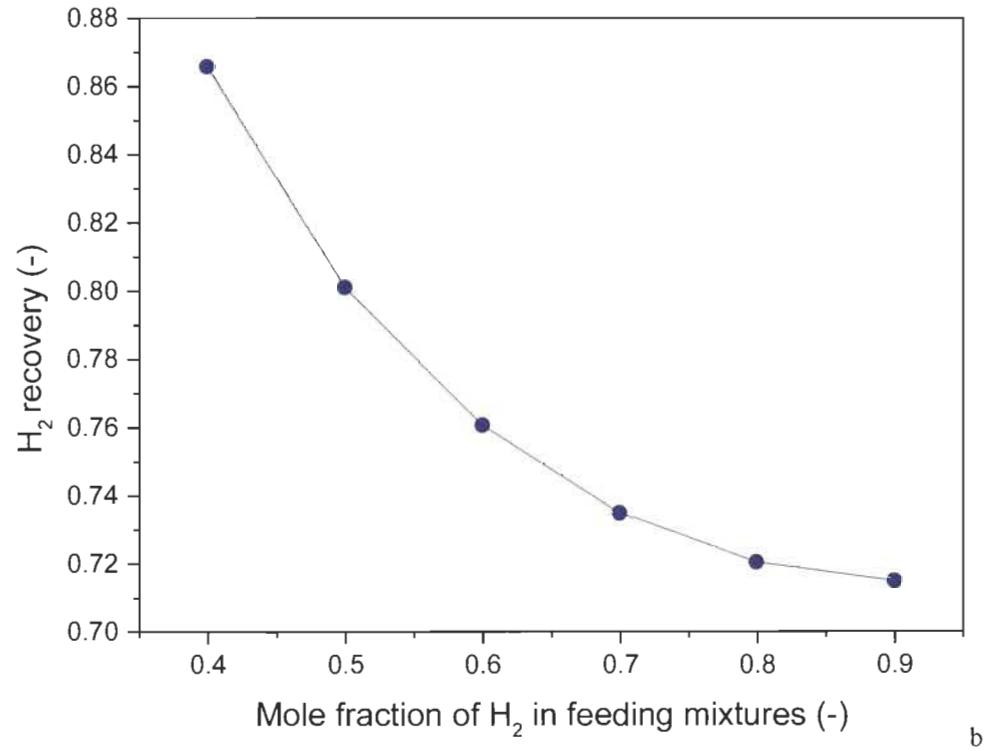

b

Fig.6.7 Effects of mole fraction of hydrogen in feeding mixtures on hydrogen purity (a) and recovery (b)

Table 6.3 Operation conditions for parametric study

Case	PSA cycle step time [s]						Adsorption pressure [bar]	Purge rate [kmol/s]	P/F ratio
	1	2	3	4	5	6			
1	30	180	40	30	180	40	4	1.61e-7	0.11
2	30	180	40	30	180	40	6	1.61e-7	0.11
3	30	180	40	30	180	40	8	1.61e-7	0.11
4	30	180	40	30	180	40	9	1.61e-7	0.11
5	30	180	40	30	180	40	11	1.61e-7	0.11
6	30	180	40	30	180	40	13	1.61e-7	0.11
7	30	180	40	30	180	40	16	1.61e-7	0.11
8	30	180	40	30	180	40	11	3.675e-8	0.025
9	30	180	40	30	180	40	11	7.35e-8	0.05
10	30	180	40	30	180	40	11	1.1e-7	0.075
11	30	180	40	30	180	40	11	2.205e-7	0.15
12	30	180	40	30	180	40	11	2.57e-7	0.175
13	30	240	40	30	240	40	11	1.61e-7	0.11
14	30	300	40	30	300	40	11	1.61e-7	0.11
15	30	360	40	30	360	40	11	1.61e-7	0.11
16	30	420	40	30	420	40	11	1.61e-7	0.11
17	30	480	40	30	480	40	11	1.61e-7	0.11
18	30	180	5	30	180	5	11	1.61e-7	0.11
19	30	180	10	30	180	10	11	1.61e-7	0.11
20	30	180	20	30	180	20	11	1.61e-7	0.11
21	30	180	30	30	180	30	11	1.61e-7	0.11
22	30	180	50	30	180	50	11	1.61e-7	0.11

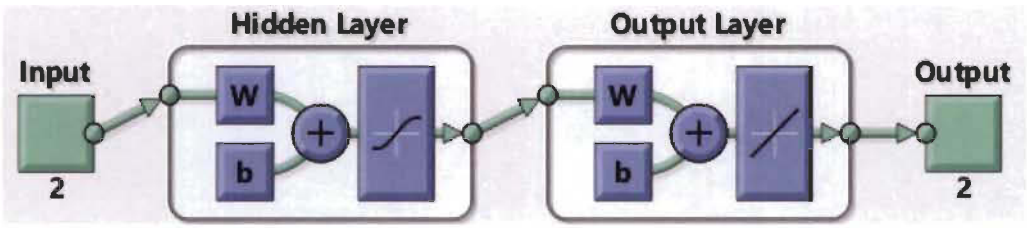

Fig.6.8 Architecture of the ANN model for predicting hydrogen purity and hydrogen recovery from adsorption pressure and adsorption step time

The adsorbent bed can adsorb more amount of methane during the adsorption step with a relatively high adsorption pressure, which leads to an increase in hydrogen purity. The higher the adsorption pressure, the more the amount of hydrogen discharged during the countercurrent depressurization step, which means the decrease of hydrogen recovery. In this work, the feed rate is fixed in the adsorption step, a relative big P/F ratio means a relatively much amount of hydrogen used to purge the adsorbent bed,

which can lead to the decrease of hydrogen recovery. Of course, a well-purified adsorbent bed is good to increase hydrogen purity. When the adsorption step time increases, the amount of product hydrogen also increases, some impurity may go through the adsorbent bed, which results in the decrease of hydrogen purity although it causes the increase of the hydrogen recovery. The effects of the pressure equalization time on the hydrogen purity and the hydrogen recovery are limited, nevertheless, a relatively short pressure equalization time is not good for the improvement of the hydrogen purity and the hydrogen recovery.

The performance of the six-step two-bed PSA cycle is compared with that of the four-step two-bed PSA cycle. The differences in the processes between the six-step two-bed PSA cycle and the four-step two-bed PSA cycle are the pressure equalization processes. As for the six-step PSA cycle, the pressure in the column increases from the low pressure to the middle pressure in the pressurizing pressure equalization step, and it continues to increase from the middle pressure to the high pressure in the feed pressurization step when the gaseous mixtures flow into the adsorbent column. There is not the pressure equalization process in the four-step PSA cycle. In the feed pressurization process of the four-step PSA cycle, a relatively large amount of hydrogen inflow into the adsorbent column, and the pressure in the column increases from the low pressure to the high pressure. As for case 5 in Table 6.3, the hydrogen purity and the recovery during the 15^{th} six-step two-bed PSA cycle are 99.8656% and 73.5225%, respectively. Based on the same operation condition as case 5, the hydrogen purity and the hydrogen recovery of the four-step two-bed PSA cycle are 98.8924% and 59.9308%, respectively. These results show that the pressure equalization processes in the PSA cycle are good to improve hydrogen recovery.

The vacuum pressure swing adsorption (VPSA) technology has been applied for hydrogen purification. There is a vacuum pump at the waster outlet in the VPSA system, which is used to decrease the pressure in the adsorbent column during the purge process. A relatively low pressure in the purge process is good to regenerate the adsorbent bed and improve the hydrogen purity. The effect of the outlet pressure at the waster port during the purge process on the hydrogen purity and recovery has been investigated, as

shown in Fig.6.6. The vacuum pump is omitted in the VPSA model, the outlet pressure is directly set for simplification. In general, the hydrogen purity increases and the recovery declines with the decrease of the outlet pressure at the waster port. The simulation results show that when the absolute pressure at the waster port is below 0.4 bar, the effect of the outlet pressure on the hydrogen purity is limited. Disregarding the slight decrease of hydrogen recovery, the vacuum pressure swing adsorption is considered as an effective method to obtain high-purity hydrogen.

Various mole fractions of hydrogen in the gaseous mixtures have been taken into consideration in the PSA model. The effects of mole fraction of hydrogen on the hydrogen purity and recovery have been presented in Fig.6.7. In general, the hydrogen recovery increases fast and the hydrogen purity declines slightly with the decrease of the mole fraction of hydrogen in the gaseous mixtures. In order to obtain a good performance of the PSA system, more works should be done to improve the operation parameters, such as the adsorption time and the adsorption pressure.

6.3 Optimization of pressure swing adsorption cycle based on artificial neural network

6.3.1 Artificial neural network model for predicting hydrogen purification performance

Artificial neural networks (ANN) are used to predict the performance of the hydrogen purification system in this section. For simplification, the adsorption pressure and the adsorption step time are considered as the input variables of the ANN model. The system performances, including the hydrogen purity and the hydrogen recovery, are set as the output results of the ANN model. The network architecture of the ANN model is shown in Fig.6.8.

Based on the validated pressure swing adsorption model, various operation conditions are taken into consideration in order to prepare a dataset used to train the artificial neural network model. The dataset is presented in Table 6.4. When this dataset is used to train the artificial neural network, it is divided into three sets: training set (70%), validation set (15%) and testing set (15%). The fractions of these three parts are set as the default values of software.

Table 6.4 Dataset used for training artificial neural network model

Operation conditions of hydrogen purification PSA cycle process as input variables		System performance as output results	
Adsorption pressure [bar]	Adsorption step time [s]	H_2 purity	H_2 recovery
6	180	0.968938	0.804422
6	240	0.956961	0.824716
6	300	0.933770	0.841704
9	180	0.994667	0.761154
9	240	0.991056	0.795785
9	300	0.985073	0.822603
11	180	0.998656	0.735225
11	240	0.996379	0.779586
11	300	0.993494	0.805815
13	180	0.99928	0.705717
13	240	0.998737	0.756373
13	300	0.997570	0.789686
16	180	0.999558	0.678232
16	240	0.999261	0.731998
16	300	0.998589	0.770266
8	180	0.991822	0.777575
6	210	0.962089	0.815132
6	270	0.944825	0.834802
9	210	0.993052	0.781199
9	270	0.988409	0.812552
11	210	0.997261	0.760934
11	270	0.995117	0.794342
13	210	0.999058	0.734082
13	270	0.998266	0.774497
16	210	0.999443	0.708675
16	270	0.998989	0.753427
8	210	0.988248	0.795795
8	240	0.985114	0.810101
8	270	0.981162	0.821507
8	300	0.977433	0.826031
15	180	0.999439	0.678158
15	210	0.999283	0.719022
15	240	0.999048	0.741992
15	270	0.998696	0.761364
15	300	0.998183	0.777414
7	180	0.983347	0.791538
7	210	0.979253	0.807599
7	240	0.974286	0.820081
7	270	0.967869	0.824785
7	300	0.963383	0.834754
14	180	0.999699	0.695892
14	210	0.999055	0.722466
14	240	0.998744	0.745637
14	270	0.998279	0.766224
14	300	0.997611	0.782298

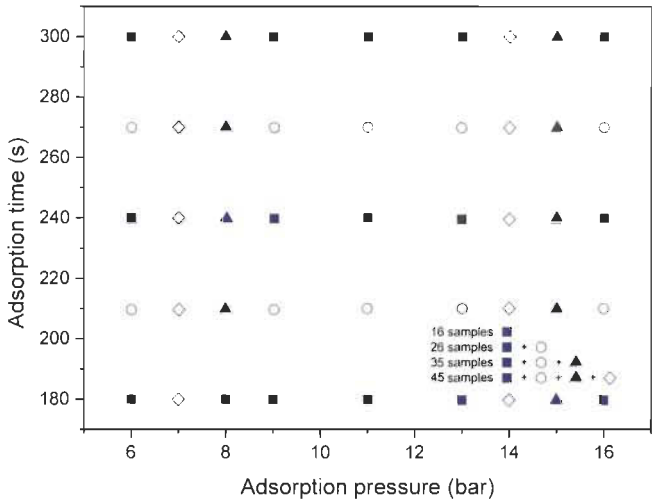

Fig.6.9 Distribution of four groups of samples (16 samples, 26 samples, 35 samples and 45 samples) produced by validated PSA model for training ANN model

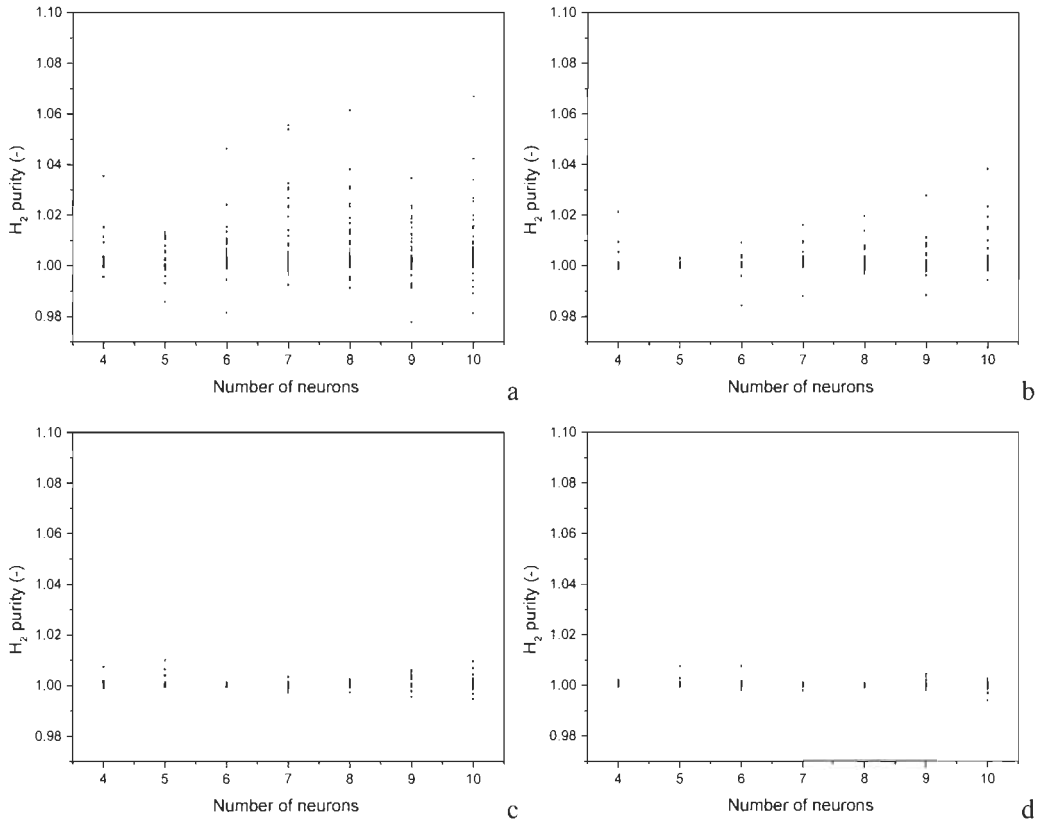

Fig.6.10 Effects of the number of neurons in the hidden layer and number of samples used for training ANN model on the maximal values of hydrogen purity predicted by trained ANN model specific operation conditions, a: 16 samples; b: 26 samples; c: 35 samples; d: 45 samples.

The artificial neural network model is carried out by the Neural Net Fitting module *nftool* in Matlab software. Levenberg-Marquardt algorithm is used to train the artificial neural network model. The *nftool* opens the Neural Net Fitting GUI and leads us to solve a data fitting problem through a feed-forward network trained with Levenberg-Marquardt.

The impact of the number of samples used for training an artificial neural network model on the predicted results is taken into consideration. Four groups of samples, which have different quantity of samples, have been used to train the artificial neural network. Fig.6.9 shows the distribution of these samples. The effect of the number of neurons in the hidden layer on the prediction results of system performance is investigated in Fig.6.10. The number of neurons in the hidden layer of artificial neural network ranges from 4 to 10. The artificial neural network models with different numbers of neurons in the hidden layer have been trained by the same dataset in order to study the effect of the number of neurons on the predicted results. The artificial neural network models with a fixed number of neurons in the hidden layer have been trained by different datasets in order to study the effect of the number of samples on the predicted results. When the number of neurons in the hidden layer is fixed, we can obtain different trained artificial neural network models even though the same dataset is used to training the artificial neural network model. It is necessary to select the best one from the trained artificial neural network models. In this work, 40 artificial neural network models with the same number of neurons, trained by the same dataset, have been used to predict the maximal value of the hydrogen purity under the specific operation conditions presented in Table 6.5. Actually, each subgraph in Fig.6.10 shows the maximal values of the hydrogen purity predicted by 280 trained ANN models under specific operation conditions.

The performance of the trained ANN is investigated by the Mean Squared Error (MSE) value of the trained model and the hydrogen purity predicted by an artificial neural network model in this work. The lower the MSE value, the better the performance of the trained artificial neural network model. As for the hydrogen purification system, the maximal value of the hydrogen purity predicted by the trained model should be close to 100% and no more than 100%. It is an important and basic thing for further

optimization work to select the trained artificial neural network model. We searched the best one from the trained artificial neural network models, which should possess the lowest MSE value and meet the requirement of hydrogen purity. The number of hidden neurons is 6 in the selected artificial neural network model. The research results in Fig.6.10 show that, the more the samples used for training an artificial neural network model, the better the predicted results. It is not good to predict system performance by choosing a relatively big number of neurons in the hidden layer.

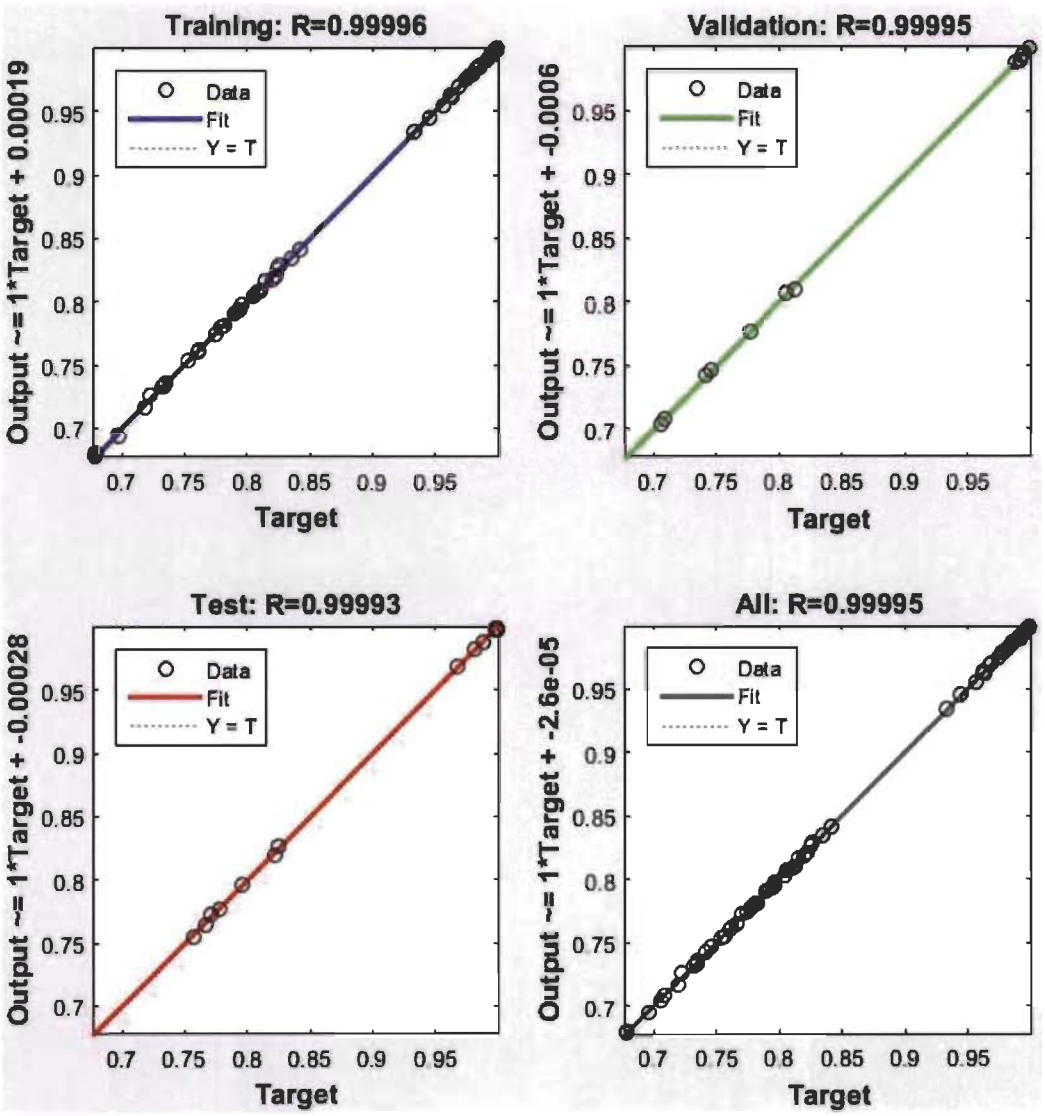

Fig.6.11 Comparison between Aspen model target and the output predicted trained ANN model, a: training set; b: validation set; c: test set; d: whole dataset.

The predicted outputs of the selected ANN model are compared with the data calculated by the pressure swing adsorption model, including the training set, the validation set, the check set and the whole dataset, as shown in Fig.6.11. The regression value R is used to measure the correlation between the predicted outputs and the targets. When the regression value R is equal to 1, it means there is a close relationship between the outputs and the targets. When the regression value R is equal to 0, it means there is a random relationship between the outputs and the targets. Fig.6.11 shows that there is a strong relationship between the predicted outputs of trained artificial neural network models and the results of the pressure swing adsorption model.

6.3.2 Performance optimization based on artificial neural network model

The well trained artificial neural network model can be used to predict the performance of the pressure swing adsorption cycle, and can also work with the optimization function *fmincon* in order to optimize the performance of the hydrogen purification system. The hydrogen purity and the hydrogen recovery of the hydrogen purification system can be predicted by the well trained artificial neural network based on the input variable X, including the adsorption pressure and the adsorption step time. The lower bound and the upper bound for the input variable X is given in Table 6.5.

Table 6.5 Lower and upper bounds for input parameters of artificial neural network model

	Adsorption pressure [bar]	Adsorption step time [s]
Lower bound	6	180
Upper bound	16	300

As for an optimization problem, there are three elements, including the objective function, the constraint condition and the design variable. The objective function for the performance optimization of the hydrogen purification system is related to the hydrogen purity and the hydrogen recovery, which is a single objective function converted by the linear weighted sum method from multi-objective function, as shown in Eq.(6.14a). The function *fmincon* on the Matlab software platform has been used to find the minimum value of the objective function under the constraint conditions. More information about performance optimization can be found in our previous works [87, 88].

The objective function and the constrained conditions for performance optimization of the pressure swing adsorption cycle process are presented as follows:

Minimize: $-[a\times RecH_2+(1-a)\times PurH_2]$, $0\leq a\leq 1$ (6.14a)

s.t.: $PurH_2>0.95$, $RecH_2>0.70$, Lower bound$<X<$Upper bound (6.14b)

where X is any of the variables of the optimal design, as shown in Table 6.5.

The well trained artificial neural network model can be applied to predict and find the optimal results under the constrained conditions. The approximate parameters are also considered in order to compare the predicted results of the artificial neural network and the simulation data from the pressure swing adsorption model. The optimal results of multi-objective optimization based on the artificial neural network model and the confirmation results by the pressure swing adsorption model are shown in Table 6.6.

Various values of the weighted factor a have been taken into consideration in the multi-objective optimization of the pressure swing adsorption system. In general, the hydrogen recovery increases with the increase of the weighted factor. The predicted results by the trained artificial neural network model on the Matlab software platform generally agree well with the simulated data of the validated pressure swing adsorption model on Aspen/Adsorption software platform. It can be considered to be a feasible method to optimize the performance of the hydrogen purification pressure swing adsorption system by the artificial neural network.

Table 6.6 Multi-objective optimization based on ANN model and confirmation by Aspen model

Weight factor a	Optimal parameters X_I	ANN prediction I	Approximate parameters X_{II}	ANN prediction II	Aspen confirmation	Error
0	[13.0482; 181.4870]	[0.705199; 0.999750]	[13.0; 181]	[0.705148; 0.999750]	[0.708169; 0.998993]	[-0.003021; 0.000757]
0.5	[8.6453; 299.9993]	[0.824119; 0.984201]	[8.6; 300]	[0.824461; 0.983851]	[0.822811; 0.985462]	[0.00165; -0.001611]
1	[6.5102; 299.9975]	[0.837481; 0.950002]	[6.5; 300]	[0.837551; 0.949719]	[0.839937; 0.951137]	[-0.002386; -0.001418]

6.4 Conclusion

A six-step two-bed pressure swing adsorption model has been developed on the Aspen/Adsorption platform in order to separate and purify hydrogen from the hydrogen/methane mixture. The extended Langmuir equation, in which the adsorption parameters are fitted from the extended Langmuir-Freundlich model, is applied to predict the adsorption isotherms of the methane and the hydrogen on the zeolite 5A adsorbent bed. The pressure swing adsorption model has been validated by comparing its simulation results with other works. The effects of the adsorption pressure, the P/F ratio, the adsorption step time and the pressure equalization time on the hydrogen purity and the hydrogen recovery of the pressure swing adsorption system are studied. A four-step two-bed pressure swing adsorption system is developed. The hydrogen recovery of the six-step two-bed pressure swing adsorption system is obviously higher than that of the four-step two-bed pressure swing adsorption system. The vacuum pressure swing adsorption system has taken into consideration. It is an effective method to obtain high-purity hydrogen through the vacuum pressure swing adsorption system. The effect of the mole fraction of hydrogen in the gaseous mixtures on the performance of the pressure swing adsorption system is investigated.

Based on the validated pressure swing adsorption model, the dataset, including the adsorption pressure and the adsorption step time as the input variables and the hydrogen purity and the hydrogen recovery as the output results, are generated to train, test and validate the artificial neural network model developed on the Matlab software platform. The well trained artificial neural network model can be applied to predict the performances of the hydrogen purification system based on the input variables. Multi-objective optimization has been considered into the hydrogen purification system through the trained artificial neural network model. The optimal results of the hydrogen purification system with various weights of the hydrogen purity and the hydrogen recovery are compared with simulation results of the validated pressure swing adsorption model. The artificial neural network model is very efficient to predict and to optimize the performance of the hydrogen purification of the pressure swing adsorption system.

Chapter 7 Hydrogen Purification based on Metal Hydride

This section has been published in: Xiao J S, Tong L, Yang T Q, et al. Lumped parameter simulation of hydrogen storage and purification systems using metal hydrides. International Journal of Hydrogen Energy, 2017, 6(42):3698-3707.
My specific contributions in this work was to simulate hydriding-dehydriding cycles by lumped parameter models and improve the efficiency of hydrogen storage system by parametric study.

Metal hydrides are attracting more and more attention due to high volumetric capacity and relatively low operation pressure. They have been used for hydrogen storage and is recently used for hydrogen purification.

7.1 Lumped parameter model for metal hydride based systems

A lumped parameter model is based on governing equations, such as mass conservation, energy conservation, reaction kinetics, the equilibrium pressure equation and the equation of state for the ideal gas. The model is implemented on the Matlab/ Simulink platform. The mass conservation equation for metal hydride can be expressed as [52]:

$$\frac{\mathrm{d}m_{\mathrm{MH}}}{\mathrm{d}t} = m_{\mathrm{s}} r_{\mathrm{a/d}} \tag{7.1}$$

where m_{MH} (g) is the mass of metal hydride, m_{s} (g) is solid material mass (excluding the mass of aluminium foam) in the system, which is assumed to be a constant for simplification, r ($g_{MH}/g_s/s$) is the metal hydride reaction rate per mass of solid material. The subscript a/d refers to absorption and desorption.

The mass conservation equations for gaseous hydrogen and carbon dioxide can be written as:

$$\frac{dm_{H_2}}{dt} = \dot{m}_{H_2 in} - \dot{m}_{H_2 out} + \dot{S}_{H_2} \tag{7.2}$$

$$\frac{dm_{CO_2}}{dt} = \dot{m}_{CO_2 in} - \dot{m}_{CO_2 out} \tag{7.3}$$

where m_{H_2} (g) and m_{CO_2} (g) is masses of gaseous hydrogen and carbon dioxide, respectively, $\dot{m}$ (g/s) is net mass flow rate, and $\dot{S}_{H_2}$ (g/s) is hydrogen generation rate. The source term $\dot{S}_{H_2}$ can be present as $\dot{S}_{H_2} = -\frac{dm_{MH}}{dt}\frac{M_{H_2} SC}{M_{MH}}$, where SC is the stoichiometric coefficient, M_{H_2} (g/mol) and M_{MH} (g/mol) is the molecular weight of hydrogen and metal hydride, respectively. The subscript in/out is used to describe the status of inflow and outflow.

An effective way to improve the heat transfer efficiency of the metal hydride reactor is to equip them with the Al foam. A general form of the energy conservation equation is [52]:

$$\begin{aligned}&\left(m_{H_2}c_{pH_2} + m_{CO_2}c_{pCO_2} + m_s c_{ps} + m_{Al}c_{pAl}\right)\frac{dT}{dt} = \\ &\left(\dot{m}_{H_2 in}c_{pH_2} + \dot{m}_{CO_2 in}c_{pCO_2}\right)\left(T_\infty - T\right) + AU\left(T_{fa/d} - T\right) + \Delta H_{a/d} r_{a/d} m_s \frac{SC}{M_{MH}}\end{aligned} \tag{7.4}$$

where c_{pH_2} (J/g/K), c_{pCO_2} (J/g/K), c_{ps} (J/g/K) and c_{pAl} (J/g/K) are the heat capacity of gaseous hydrogen, carbon dioxide, the solid material and the aluminium foam, respectively, T_∞ (K) is the inflow/outflow temperature, and we assume that the outflow temperature is equal to the average temperature in the reactor. A (m^2) is the surface area for heat transfer, U ($W/m^2/K$) is overall heat transfer coefficient, T_j (K) is the ambient temperature, which is the temperature of cooling/heating water when the reactor is equipped with a circulating water device. ΔH (J/mol) is the enthalpy of reaction. The mass of Al foam m_{Al} (g) should be set as 0 when there is no Al foam in the reactor.

The reaction rates for the metal hydride during absorption and desorption can be shown to be, respectively [52]:

$$r_a = C_a e^{-E_a/(RT)} \left(\ln \frac{p_{H_2}}{p_{eq}} \right) \left(1 - \frac{m_{MH}}{m_s} \right) \tag{7.5}$$

$$r_d = C_d e^{-E_d/(RT)} \left(\frac{p_{H_2} - p_{eq}}{p_{eq}} \right) \left(\frac{m_{MH}}{m_s} \right) \tag{7.6}$$

where C is the kinetics constant, E (J/mol) is activation energy, p_{eq} (bar) is the equilibrium pressure, T (K) is the average temperature. p_{H_2} (bar) is the partial pressure of gaseous hydrogen in the reactor, which is equal to the supply pressure p_a during absorption, or the outlet pressure p_d during desorption in the metal hydride hydrogen storage system.

The total pressure is assumed to be constant in the lumped parameter model. The equilibrium pressure equation can be described as [52]:

$$\ln \left(\frac{p_{eq}}{p_0} \right) = - \frac{\Delta H_{a/d}}{RT} + \frac{\Delta S_{a/d}}{R} + k_{sl} \left(\frac{m_{MH}}{m_s} - 0.5 \right) \tag{7.7}$$

where ΔS (J/mol/K) is the entropy, k_{sl} is the plateau slope coefficient which is equal to 0.13, and p_0 (bar) is the reference pressure (1bar).

In this work, the gaseous hydrogen and carbon dioxide can be assumed to be ideal gases:

$$m_{H_2} = \frac{p_{H_2} V_g}{RT} M_{H_2} \tag{7.8}$$

$$m_{CO_2} = \frac{p_{CO_2} V_g}{RT} M_{CO_2} \tag{7.9}$$

where p_{H_2} (bar) and p_{CO_2} (bar) are the partial pressures of gaseous hydrogen and carbon dioxide respectively, V_g (m^3) is the volume for the gas phase in the reactor, and R (J/mol/K) is universal gas constant. Pure hydrogen gas is used for hydrogen storage

systems, and carbon dioxide is the only impurity considered for the case of the hydrogen purification system. The gas phase materials in the hydrogen purification system include gaseous hydrogen and carbon dioxide in the reactor during absorption and venting process.

The concentration of impurity imp in the hydrogen purification system is [53]

$$\text{imp} = \frac{m_{CO_2}}{m_{CO_2} + m_{H_2}} \times 100 \tag{7.10}$$

The carbon dioxide concentration of mass inflow imp is assumed to be 2.15 during absorption. The relationship between mass flow rates of gaseous hydrogen and carbon dioxide can be written as [53]:

$$\dot{m}_{H_2 in/out} = \dot{m}_{CO_2 in/out}\left(\frac{100}{\text{imp}} - 1\right) \tag{7.11}$$

where the subscript in/out refers to inflow/outflow.

During the venting process, the mass outflow rate of gaseous hydrogen and carbon dioxide should satisfy the following equation in order to avoid exterior gas entering the reactor [53].

$$\dot{m}_{H_2 out} + \dot{m}_{CO_2 out} = -k_{FC}\pi r_v^2 p\sqrt{\frac{2k}{RT(k-1)}\left(M_{H_2}\frac{p_{H_2}}{p} + M_{CO_2}\frac{p_{CO_2}}{p}\right)\left[\left(\frac{p_{ext}}{p}\right)^{2/k} - \left(\frac{p_{ext}}{p}\right)^{(k+1)/k}\right]} \tag{7.12}$$

where $\dot{m}_{H_2 out}$ and $\dot{m}_{CO_2 out}$ can be set to 0 during the absorption stage while $\dot{m}_{H_2 in}$ and $\dot{m}_{CO_2 in}$ are equal to 0 during the venting stage. The gas phase is composed of hydrogen and carbon dioxide in the reactor during absorption and venting. We assume that carbon dioxide has been discharged completely at the end of the venting process. Therefore, $\dot{m}_{H_2 in}$, $\dot{m}_{CO_2 in}$ and $\dot{m}_{CO_2 out}$ can be taken as 0 during desorption.

7.2 Simulation of hydrogen storage system using metal hydrides

In order to validate the lumped parameter model, the simulation results have been compared with experimental data [42]. This reference considers two reactors packed

with $LaNi_5$ of different sizes: a small metal hydride reactor without any heat exchanger, and a big one with aluminium foam cooled/heated by circulating water. The parameters used in hydrogen storage system simulations are shown in Table 7.1 [52]. Since the effect of the reversible part of the PCT plateau on the simulation has been taken into consideration in this work, the value of SC was set as 2.76 rather than 3 [52].

Table 7.1 Parameters used in hydrogen storage simulation

Parameter	Value in small reactor	Value in big reactor	Parameter	Value in small reactor	Value in big reactor
A [m^2]	5.0e-4	3.0e-3	E_a [J/mol]	21170	21170
V_g [m^3]	4.4e-7	4.8e-6	E_d [J/mol]	16420	16420
U [$W/m^2/K$]	80	2500	C_a [1/s]	59.2	59.2
m_s [g]	1	25	C_d [1/s]	9.6	9.6
p_a [bar]	6	12.7	c_{pH_2} [J/g/K]	14.3	14.3
p_d [bar]	0.068	0.086	c_{ps} [J/g/K]	0.355	0.355
$T_{fa/d}$ [K]	296	323	c_{pAl} [J/g/K]	-	0.963
T_∞ [K]	290	290	m_{Al} [g]	-	18
ΔH_a [J/mol]	30478	30478	R [J/mol/K]	8.314	8.314
ΔH_d [J/mol]	30800	30800	M_{H_2} [g/mol]	2	2
$\Delta S_{a/d}$ [J/mol]	108	108	M_{MH} [g/mol]	432	432
p_0 [bar]	1	1	k_{sl} [1]	0.13	0.13

Our simulations results for the two reactor configurations have been compared with Refs.[42, 52]. Laurencelle et al. [42] have performed these experiments and developed one-dimension model along the radial direction, and the simulation results agreed well with the experiment data. In addition, Talaganis et al. [52] have built a lumped parameter model and validated it in contrast with simulation data from Ref.[42]. Their simulation results can be used to validate our lumped parameter model.

Hydrogenation capacity in the metal hydride hydrogen storage system is explained by the following equation:

$$\mathrm{wt} = \frac{m_{MH} M_{H_2} SC}{m_s M_{MH}} \times 100\% \tag{7.13}$$

The average temperature and the hydrogen storage capacity in metal hydride tank are shown in Fig.7.1. As shown in a hydriding-dehydriding cycle, the hydrogen storage capacity increases during absorption and decreases during desorption. The average temperature rises quickly during the early stages of the hydriding process due to the amount of heat generated, followed by a decline due to a decrease in the reaction rate and heat being released into the environment. In general, the simulation results agreed well with other results, and the model can be considered to be validated.

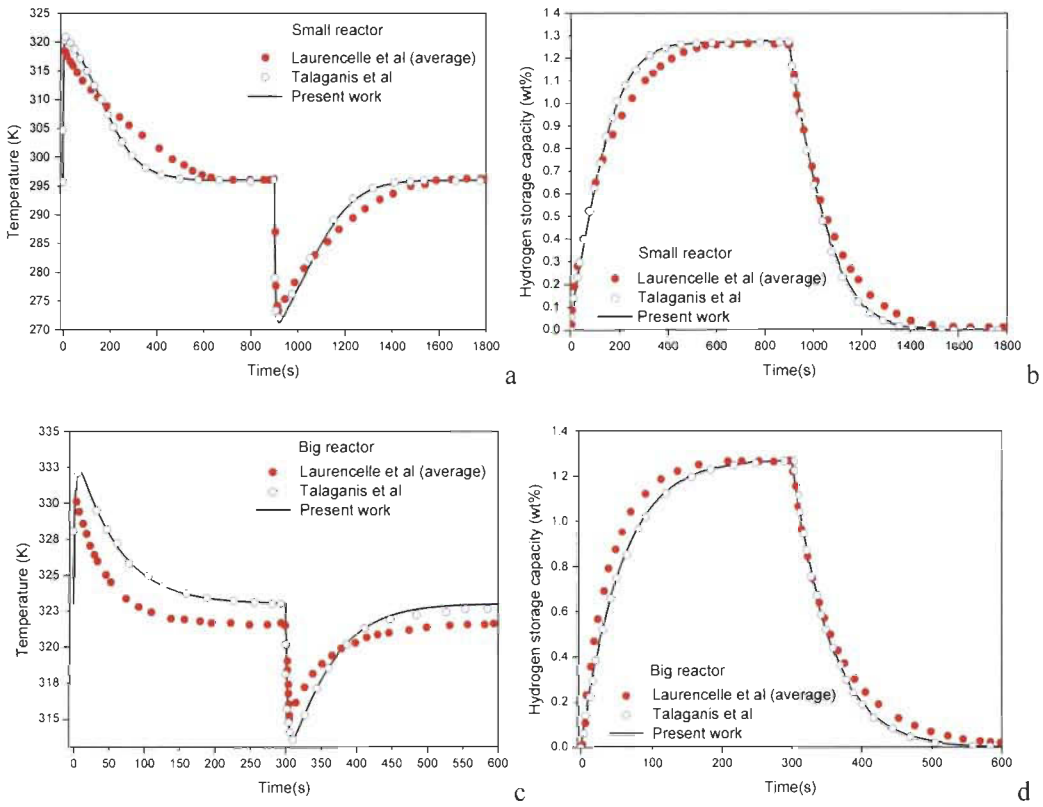

Fig. 7.1 Model validation for small reactor (a,b) and big reactor (c,d): temperature comparison(a,c), hydrogen storage capacity comparison (b,d)

7.3 Simulation of hydrogen purification system using metal hydrides

Metal hydrides can also be used to purify hydrogen. A sorption-based purification process requires three basic steps: (1) absorption, (2) venting and (3) desorption. Pure hydrogen can be separated from impurities by hydriding reaction in the absorption step; the impurities are removed from the purification system during the venting step; and the purified hydrogen is generated by dehydriding during the desorption step.

7.3.1 Description of hydrogen purification system

In this section, carbon dioxide is the only impurity present in the system. It is assumed to remain chemically inert during the purification process. A furnace in an assumed industrial process is the source of impurity. As shown in Fig.1 of Ref. [53], the furnace is fed by hydrogen gas from the purification system for reduction reaction and produces the impurity carbon dioxide. The purification system is assumed to be composed of two identical reactors which are cooled or heated by circulating water. When one is in the adsorbing step, the other is in the desorbing step in order to supply purified hydrogen to the furnace continuously. Some hydrogen storage tanks filled with pure hydrogen can be used to supply hydrogen when the metal hydride reactor is operated in the venting process.

There are three control valves for each reactor, which can be used to change the reaction process of the purification system. We assume that the absorption time t_a is equal to the sum of the venting time t_v and the desorption time t_d. Table 7.2 shows the scheme of the operation process. More information about this process can be obtained from Ref.[53].

Table 7.2 Scheme of operation process

	Valve	Absorption	Venting	Desorption
Reactor1	Inlet	opened	closed	closed
	Outlet	closed	closed	opened
	Venting	closed	opened	closed

	Valve	Venting	Desorption	Absorption
Reactor2	Inlet	closed	closed	opened
	Outlet	closed	opened	closed
	Venting	opened	closed	closed

Table 7.3 Parameters used in hydrogen purification simulation

Parameter	Value	Parameter	Value	Parameter	Value
A [m^2]	5.7	k	1.38	t_a [s]	1985.60
V_g [m^3]	0.018	k_{FC}	0.62	t_v [s]	3.64
$\mathrm{imp_{in}}$	2.15	r_v [m]	0.05	t_d [s]	1981.96
m_s [kg]	150	c_{pCO_2} [J/g/K]	0.839	p_{ext} [bar]	1
$T_{fa/d}$ [K]	309	$\dot{m}_{in}$ [g/s]	0.56	M_{CO_2} [g/mol]	44
T_∞ [K]	326	m_{s0} [kg]	26.47	SC	3

7.3.2 Complementary equations and parameters for hydrogen purification system

The parameters specific to the purification simulations are given in Table 7.3. Based on these complementary conditions, the Simulink model can be developed to predict the process of purification system using metal hydride.

The efficiency of hydrogen purification system can be measured by the hydrogen recovery rate:

$$\mathrm{RE}_{\mathrm{H_2}} = \frac{m_{\mathrm{MH\text{-}vf}} - m_{\mathrm{MH\text{-}ai}}}{m_{\mathrm{MH\text{-}af}} - m_{\mathrm{MH\text{-}ai}}} \times 100\% \tag{7.14}$$

where $m_{\mathrm{MH\text{-}ai}}$ and $m_{\mathrm{MH\text{-}af}}$ are initial and final mass of metal hydride during the absorption process, respectively, and where $m_{\mathrm{MH\text{-}vf}}$ is the final mass of metal hydride during the venting process.

7.3.3 Simulation results for hydrogen purification system

Based on the above equations, the hydrogen purification model was implemented on the Matlab/Simulink platform, and its simulation results have been compared with other works[53]. In this section, supply pressure during absorption is set to 5 bar, while outlet pressure is assumed to be 2 bar during desorption. The mass flow rate during the absorption process is equal to 0.56 g/s. The venting step begins when the total pressure in the reactor reaches 5 bar during the hydriding process. The outlet pressure during the dehydrogenation process is set as constant, mass outflow rate in pulse form can be taken into consideration for boundary condition. The overall heat transfer coefficient is assumed to be 243 $W/m^2/K$. Some pure hydrogen reservoirs can be used to ensure a continuous supply of hydrogen for the assumed industrial process.

Fig.7.2 shows the variation of temperature (a); equilibrium pressure (b); impurity concentration (c); metal hydride mass(d); total and partial pressure of gaseous H_2 and CO_2 (f); and gaseous H_2 and CO_2 mass (e). In general, our results agree well with the data from other literature. The CO_2 partial pressure and impurity concentration increase during absorption, and decrease to about 0 during venting. The average temperature rises quickly during the early stages of the absorption process. At the beginning of the

absorption, 26.47 kg metal hydride has been converted from some of the 150kg $LaNi_5$ alloy. The final mass of metal hydride during absorption and venting process are 104.6 kg and 101.9 kg, respectively. In this case, the hydrogen recovery rate of purification system is equal to 96.54%.

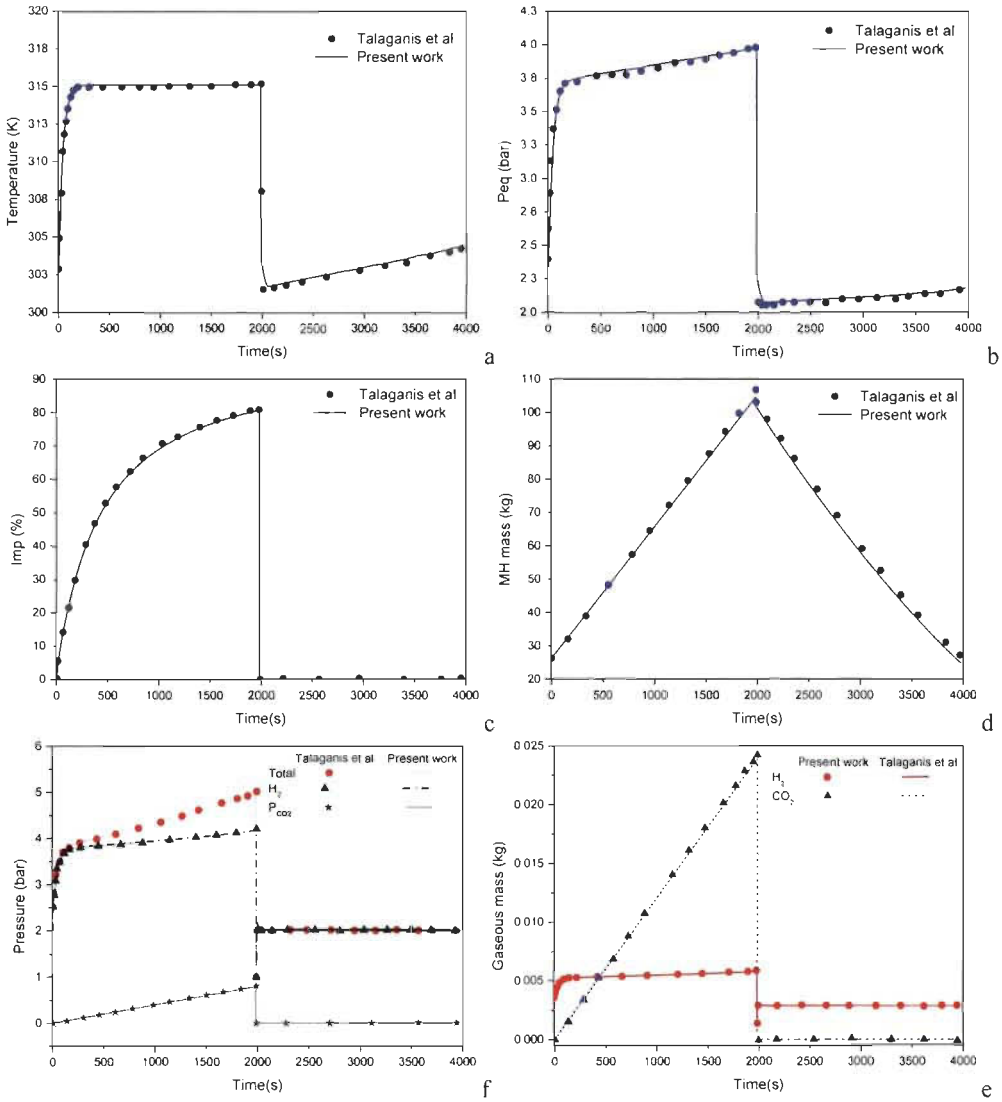

Fig.7.2 Model validation for hydrogen purification system, comparisons of temperature(a); equilibrium pressure(b); impurity concentration(c); metal hydride mass(d); total and partial pressure of gaseous H_2 and CO_2(e); and gaseous H_2 and CO_2 mass(f)

7.3.4 Parametric study for hydrogen purification system

In order to improve the hydrogen recovery rate of the purification system, a parametric study was performed. The effects of solid material mass, overall heat transfer

coefficient and cooling water temperature on the hydrogen recovery rates have been analyzed. The change of solid material mass could be related to the variation of the size of metal hydride reactors. Table 7.4 presents the parameters used for the parametric study of the hydrogen purification system. The outlet pressure in each case is the same. The total pressure in the reactor reaches up to the supply pressure at the end of the absorption process. The mass of carbon dioxide increases in the absorption process and decreases during venting. Venting is performed until the concentration of carbon dioxide is less than 4×10^{-6}, at which point we assume that carbon dioxide has been completely discharged.

Table 7.4 Parameters used in parametric studies for hydrogen purification system

Case	T_{wa} [K]	U [W/m^2/K]	p_a [bar]	m_s [kg]	t_a [s]	t_v [s]	t_d [s]
1	309	243	5	60	84.65	3.55	81.31
2				75	204	3.24	200.76
3				90	568.54	2.82	565.72
4				105	942.48	2.86	939.62
5				120	1311.24	3.06	1308.18
6				135	1675.38	3.34	1672.04
7				150	1985.6	3.64	1981.96
8	309	243	4	60	37.06	4.83	32.23
9			6		398.43	2.12	396.31
10			7		844.88	1.66	843.22
11			8		1051.54	1.59	1049.95
12			9		1128.91	1.57	1127.34
13			10		1164.93	1.57	1163.36
14	309	193	5	60	70.19	3.62	66.57
15		293			125.5	3.35	122.15
16		343			265.79	2.81	262.98
17		393			396.97	2.52	394.45
18		443			492.8	2.39	490.41
19		493			564.8	2.32	562.48
20	284	243	5	60	1112.28	4.04	1108.24
21	289				1068.37	2.88	1065.49
22	294				969.18	2.39	966.79
23	299				735.18	2.24	732.94
24	304				322.87	2.67	320.20
25	314				52.21	3.70	48.51

Fig. 7.3 shows some of the simulation results of the parametric study. In total, 25 cases are used for the parametric study of the purification system. Fig 7.3a shows that the hydrogen recovery rate of the purification system rises with the increase of solid material mass. As the cost of the solid material rises when its mass is increased, it is important to improve the hydrogen recovery of the hydrogen purification reactor

compacted with a relatively small solid material mass. Thus, the solid material mass is set as 60 kg for further study in Fig 7.3b, c and d. The simulation results show that a relatively large overall heat transfer coefficient is beneficial to improve the hydrogen recovery, and constitute a good way to increase hydrogen recovery rate by reducing the cooling water temperature and enhancing the supply pressure.

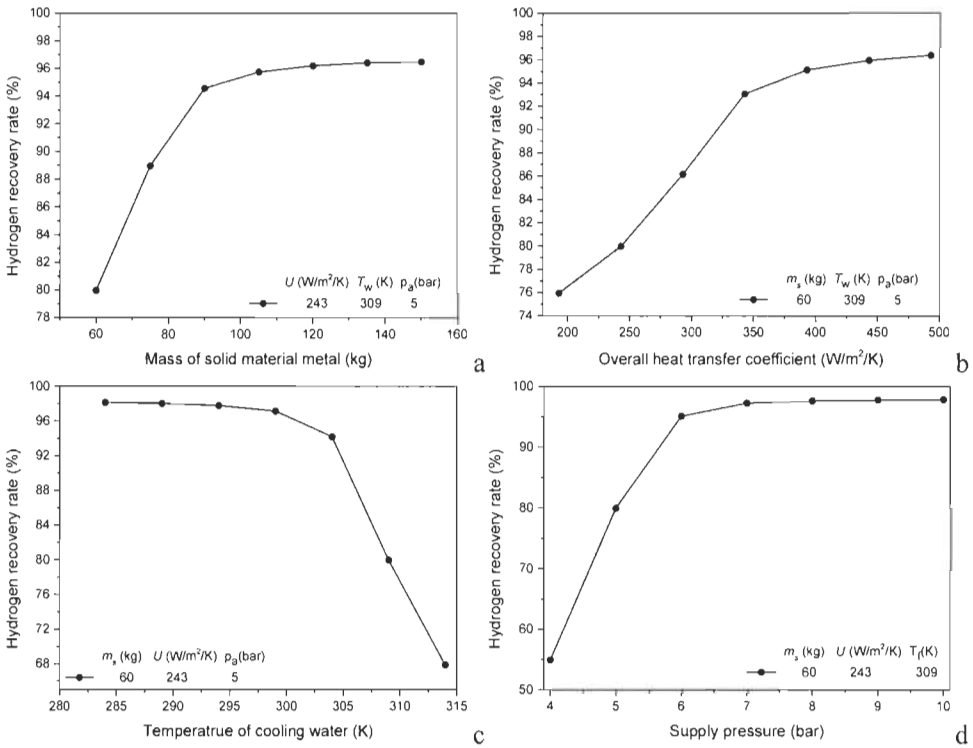

Fig.7.3 Parametric studies for hydrogen purification system, Solution for different solid material mass (a), overall heat transfer coefficient (b), cooling water temperature (c) and supply pressure (d)

7.4 Conclusion

Lumped parameter models based on the Matlab/Simulink software platform have been implemented for hydrogen storage and purification systems using metal hydrides. The hydrogen storage models were based on the following governing equations: mass conservation, energy conservation, reaction kinetics, equilibrium pressure equation and the equation of state for the ideal gas. The models have been validated by comparing the simulation results with data from the literature.

Based on the validated hydrogen storage models, a hydrogen purification model has

been developed by combining them with some complementary equations. The model has been validated, and its simulation results agree well with the data from the literature. In order to improve the hydrogen recovery rate of the purification system, the effects of solid material mass, overall heat transfer coefficient and cooling water temperature on the hydrogen recovery rates were taken into consideration. In general, the hydrogen recovery rate of the purification system rises with the increase of solid material mass and overall heat transfer coefficient. In addition, reducing cooling temperature and enhancing the supply pressure can be considered to increase the hydrogen recovery rate.

Chapter 8 Conclusion, Contribution and Future Work

8.1 Conclusions

During this work, I completed the simulation and optimization of the filling of a hydrogen storage tank filled with compacted activated carbon as the adsorbent using pre-cooling and flow-through cooling methods. The coiled tube heat exchanger and the phase change material heat exchanger have been taken into consideration the metal hydride hydrogen storage tank in order to improve system performance. Lumped parameter models have been developed for hydrogen storage and purification system using metal hydride. The hydrogen purification performance optimization of the PSA cycle using zeolite has been completed using the artificial neural network model.

The method of flow-through cooling is studied for a hydrogen delivery tank packed with activated carbon. As a result, it can improve the hydrogen storage capacity by about 15%. The flow-through cooling combined with pre-cooling takes less time to cool adsorbent material in the hydrogen storage system than other cases, and can be considered as an effective way to improve the heat transfer in the adsorbent bed during the adsorption process and increase the hydrogen storage capacity of the hydrogen delivery tank.

The analytical solutions of lumped temperature for the metal hydride hydrogen storage system are obtained from the thermodynamic model in various processes. The analytical solution can be used as a reference for more detailed two-dimensional or three-dimensional models. Four cases under constant/variable inflow/outflow temperature conditions are analytically studied, the results show that the effect the variable inflow/outflow temperature condition on the lumped temperature in metal hydride system is not obvious compared to the constant inflow/outflow temperature condition. The analytical solution for the hydriding-dehydriding cycle is compared with the result of a reduced model proposed in the reference, the comparison shows

that the analytical solution is more accurate than the reduced model. Then, the variable mass source term is taken into consideration in the validated lumped parameter numerical model. The metal hydride source term during hydriding can be considered roughly as constant, which is true when the hydrogen storage capacity of the metal hydride system is not beyond about 90% of its limited capacity.

Various heat exchangers are taken into consideration in the design of the metal hydride reactor. The coiled-tube heat exchanger presents better heat transfer performance than the straight pipe heat exchanger. Dual heat exchangers, including the combination of the coiled-tube heat exchanger and straight pipe heat exchanger and the dual coiled-tube heat exchangers, are discussed. As for the metal hydride hydrogen storage reactor equipped with the coiled-tube heat exchanger, reduced two-dimensional model is taken into consideration in order to decrease the computing time. The effectiveness has been validated by comparing the simulation results of the reduced model with those of the complete three-dimensional model. The reduced two-dimensional model can well approximate the complete three-dimensional model for the case with more turns of coiled-tube.

The phase change material heat exchanger has been introduced to the metal hydride hydrogen storage system in this work. Metal foams, including Al foam and copper foam, were composited with phase change materials in order to increase the effective thermal conductivity of phase change materials and improve the hydrogen storage efficiency of metal hydride reservoir. Compared with the system equipped with Al foam, the system equipped with copper foam shown about 34% improvement of the time when the hydrogen storage capacity reached up to the maximum value.

As for the hydrogen purification system using adsorbent, a six-step two-bed pressure swing adsorption model has been developed and validated to separate and purify hydrogen from the hydrogen/methane mixture. The extended Langmuir equation fitted from the extended Langmuir-Freundlich model is applied to predict the adsorption isotherms of methane and hydrogen on zeolite 5A adsorbent bed. The effects of the adsorption pressure, the P/F ratio, the adsorption step time and the pressure equalization time on the system performances are studied. The research results show that the

hydrogen recovery of the six-step two-bed pressure swing adsorption system is obviously higher than that of the four-step two-bed pressure swing adsorption system. It is an effective method to obtain high-purity hydrogen through the vacuum pressure swing adsorption system. The effect of the mole fraction of hydrogen in the gaseous mixtures on the performance of the pressure swing adsorption system is investigated. Then, the validated pressure swing adsorption model is applied to generate a dataset, which is used to train, test and validate the artificial neural network model. The well trained artificial neural network model can be applied to predict the performances of hydrogen purification system based on the input variables. Multi-objective optimization has been considered into the hydrogen purification system through the trained artificial neural network model. The artificial neural network model is very efficient to predict and to optimize the performance of the hydrogen purification of the pressure swing adsorption system.

Lumped parameter models based on Matlab/Simulink platform have been implemented for hydrogen storage and purification systems using metal hydrides. The models have been validated by comparing the simulation results with data from the literature. In order to improve the hydrogen recovery rate of the purification system, the effects of solid material mass, overall heat transfer coefficient and cooling water temperature on the hydrogen recovery rates were taken into consideration. In general, the hydrogen recovery rate of the purification system rises with the increase of solid material mass in the reactor and overall heat transfer coefficient. In addition, reducing cooling temperature and enhancing the supply pressure can be considered to increase the hydrogen recovery rate.

8.2 Contributions

During the course of this Ph.D. work I have successfully published three articles as first author :

1. Tong L, Xiao J S, Cai Y H, et al. Thermal effect and flow-through cooling of an adsorptive hydrogen delivery tank. International Journal of Hydrogen Energy, 2016, 36(41):16094-16100. (Chapter 2)

2. Tong L, Xiao J S, Yang T Q, et al. Complete and reduced models for metal hydride reactor with coiled-tube heat exchanger. International Journal of Hydrogen Energy, 2019, 30(44):15907-15916.(Chapter 4)

3. Tong L, Xiao J S, Bénard P, et al. Thermal management of metal hydride hydrogen storage reservoir using phase change materials. International Journal of Hydrogen Energy, 2019, 38(44):21055-21066. (Chapter 5)

and co-authored two published papers:

1. Xiao J S, Tong L, Bénard P, et al. Thermodynamic analysis for hydriding-dehydriding cycle of metal hydride system. Energy 2019. https://doi.org/10.1016/j.energy.2019.116535. (Chapter 3)

2. Xiao J S, Tong L, Yang T Q, et al. Lumped parameter simulation of hydrogen storage and purification systems using metal hydrides. International Journal of Hydrogen Energy, 2017, 6(42):3698-3707. (Chapter 6)

I simulated and examine the optimization of a flow-through cooling method on a cryoadsorption-based delivery tank for hydrogen based on activated carbon using a validated model[18].

The lumped parameter models for the hydrogen storage system and the hydrogen purifications system using metal hydride have been developed and validated to study the system performance as a whole[60]. An analytical solution for the lumped temperature of the metal hydride hydrogen storage system has been obtained from the basic thermodynamical model, which can be considered as a benchmark to validate the lumped parameter model and the distributed parameter model[15].

The coiled tube heat exchanger has been applied to the metal hydride hydrogen storage system to improve the heat transfer in the reactor. The validated reduced 2D model for the metal hydride reactor equipped with the coiled tube heat exchanger is effective method to study the system performance[41].

The phase change material heat exchanger, which can be used to store the heat released during hydriding and provide the heat during dyhydriding, has been introduced to the metal hydride hydrogen storage system. The phase change material has been

composited with the metal foam in order to increase the effective thermal conductivity. The composited phase change material has been applied to the metal hydride hydrogen storage system in order to improve system performance[51].

The six-step two-bed pressure swing adsorption model has been developed and validated to purify hydrogen from the hydrogen/methane mixture using zeolite 5A as the adsorbent. The artificial neural network model has been trained by the dataset generated the validated model under various operation conditions. The trained artificial neural network model has been used to predict and optimize the performance of the hydrogen purification pressure swing adsorption system.

8.3 Future works

As for the hydrogen storage system based on the metal hydride, the lumped parameter model and the distributed parameter model are both developed to optimize the system performance. The lumped parameter model is used to study the hydrogen storage system as a whole. The distributed parameter model is applied to research heat and mass transfer, which is used for the metal hydride reactor with a complicated structure. The coiled tube heat exchanger and the phase change material heat exchangers have been applied to the metal hydride reactor. However, only the hydriding process is studied based on the distributed parameter model in present work. More works can be done for the hydriding/dehydriding cycle through these distributed parameter models.

As for the hydrogen purification system based on the metal hydride, a lumped parameter model has been developed and validated to investigate the system performance. The distributed parameter model for the hydrogen purification system is necessary to research the heat and mass transfer in the metal hydride bed. More measures should be taken into consideration to improve the thermal effect during hydriding/dehydriding on the performance of the hydrogen purification system.

As for the hydrogen purification system based on the adsorbent, the layered bed and the novel adsorbent materials play important roles to improve the performance of the hydrogen purification system. More works should be done to research the hydrogen purification pressure swing adsorption cycle and vacuum pressure swing adsorption

cycle from the multicomponent gaseous mixtures based on the layered bed and the novel adsorbent materials.

Machine learning has been received wide attention in all fields. Deep learning can be considered as an effective method to predict and optimize the performance of a complicated system . The artificial neural network used in present work is a basic two-layer feed-forward neural network on the Matlab software platform. In general, deep learning is more complicated than the artificial neural network. Deep learning can be applied to solve complex problems. In further research, the deep learning method can be used to optimize the performance of the hydrogen purification pressure swing adsorption system.

Reference

[1] Nikolaidis P, Poullikkas A. A comparative overview of hydrogen production processes[J]. Renewable and Sustainable Energy Reviews, 2017, 67):597-611.

[2] Zheng J Y, Liu X X, Xu P, et al. Development of high pressure gaseous hydrogen storage technologies[J]. International Journal of Hydrogen Energy, 2012, 1(37):1048-1057.

[3] Petitpas G, Bénard P, Klebanoff L E, et al. A comparative analysis of the cryo-compression and cryo-adsorption hydrogen storage methods[J]. International Journal of Hydrogen Energy, 2014, 20(39):10564-10584.

[4] Jiménez V, Ramírez-Lucas A, Sánchez P, et al. Improving hydrogen storage in modified carbon materials[J]. International Journal of Hydrogen Energy, 2012, 5(37):4144-4160.

[5] Xiao J S, Peng R, Cossement D, et al. CFD model for charge and discharge cycle of adsorptive hydrogen storage on activated carbon[J]. International Journal of Hydrogen Energy, 2013, 3(38):1450-1459.

[6] Xiao J S, Zhou Z Q, Cossement D, et al. Lumped parameter model for charge–discharge cycle of adsorptive hydrogen storage system[J]. International Journal of Heat and Mass Transfer, 2013, 64):245-253.

[7] Xiao J S, Wang J J, Cossement D, et al. Finite element model for charge and discharge cycle of activated carbon hydrogen storage[J]. International Journal of Hydrogen Energy, 2012, 1(37):802-810.

[8] Xiao J S, Hu M, Cossement D, et al. Finite element simulation for charge–discharge cycle of cryo-adsorptive hydrogen storage on activated carbon[J]. International Journal of Hydrogen Energy, 2012, 17(37):12947-12959.

[9] Xiao J S, Tong L, Cossement D, et al. CFD simulation for charge–discharge cycle of cryo-adsorptive hydrogen storage on activated carbon[J]. International Journal of Hydrogen Energy, 2012, 17(37):12893-12904.

[10] Xiao J S, Li Q, Cossement D, et al. Lumped parameter simulation for charge–discharge cycle of cryo-adsorptive hydrogen storage system[J]. International Journal of Hydrogen Energy, 2012, 18(37):13400-13408.

[11] Xiao J S, Zhou T T, Cossement D, et al. Coupled thermal simulation of hydrogen storage tank-dewar flask system[J]. International Journal of Hydrogen Energy, 2013, 25(38):10880-10888.

[12] Xiao J S, Hu M, Bénard P, et al. Simulation of hydrogen storage tank packed with metal-organic framework[J]. International Journal of Hydrogen Energy, 2013, 29(38):13000-13010.

[13] Xiao J S, Bénard P, Chahine R. Adsorption–desorption cycle thermodynamics for adsorptive hydrogen storage system[J]. International Journal of Hydrogen Energy, 2016, 14(41):6139-6147.

[14] Xiao J S, Bénard P, Chahine R. Charge-discharge cycle thermodynamics for compression hydrogen storage system[J]. International Journal of Hydrogen Energy, 2016, 12(41):5531-5539.

[15] Xiao J S, Tong L, Bénard P, et al. Thermodynamic analysis for hydriding-dehydriding cycle of metal hydride system. Energy 2019. https://doi.org/10.1016/j.energy.2019.116535.

[16] Corgnale C, Hardy B, Chahine R, et al. Simulation of hydrogen adsorption systems adopting the flow through cooling concept[J]. International Journal of Hydrogen Energy, 2014, 30(39):17083-17091.

[17] Ubaid S, Zacharia R, Xiao J S, et al. Effect of flowthrough cooling heat removal on the performances of MOF-5 cryo-adsorptive hydrogen reservoir for bulk storage applications[J]. International Journal of Hydrogen Energy, 2015, 30(40):9314-9325.

[18] Tong L, Xiao J S, Cai Y H, et al. Thermal effect and flow-through cooling of an adsorptive hydrogen delivery tank[J]. International Journal of Hydrogen Energy, 2016, 36(41):16094-16100.

[19] Xiao J S, Wang X, Bénard P, et al. Determining hydrogen pre-cooling temperature from refueling parameters[J]. International Journal of Hydrogen Energy, 2016, 36(41):16316-16321.

[20] Lv P, Huot J. Hydrogen storage properties of $Ti_{0.95}FeZr_{0.05}$, $TiFe_{0.95}Zr_{0.05}$ and $TiFeZr_{0.05}$ alloys[J]. International Journal of Hydrogen Energy, 2016, 47(41):22128-22133.

[21] Lv P, Huot J. Hydrogenation improvement of TiFe by Aadding $ZrMn_2$[J]. Energy, 2017, 138:375-382.

[22] MacDonald B D, Rowe A M. Impacts of external heat transfer enhancements on metal hydride storage tanks[J]. International Journal of Hydrogen Energy, 2006, 12(31):1721-1731.

[23] Mayer U, Groll M, Supper W. Heat and mass transfer in metal hydride reaction beds: experimental and theoretical results[J]. Journal of the Less Common Metals, 1987, 1(131):235-244.

[24] Yang F S, Meng X Y, Deng J Q, et al. Identifying heat and mass transfer characteristics of metal hydride reactor during adsorption: improved formulation about parameter analysis[J]. International Journal of Hydrogen Energy, 2009, 4(34):1852-1861.

[25] Chung C A, Ho C J. Thermal–fluid behavior of the hydriding and dehydriding processes in a metal hydride hydrogen storage canister[J]. International Journal of Hydrogen Energy, 2009, 10(34):4351-4364.

[26] Jemni A, Nasrallah S B, Lamloumi J. Experimental and theoretical study of a metal–hydrogen reactor[J]. International Journal of Hydrogen Energy, 1999, 7(24):631-644.

[27] Chung C A, Lin C S. Prediction of hydrogen desorption performance of Mg_2Ni hydride reactors[J]. International Journal of Hydrogen Energy, 2009, 23(34):9409-9423.

[28] Chung C A, Yang S W, Yang C Y, et al. Experimental study on the hydrogen charge and discharge rates of metal hydride tanks using heat pipes to enhance heat transfer[J]. Applied Energy, 2013, 103:581-587.

[29] Bhouri M, Goyette J, Hardy B J, et al. Honeycomb metallic structure for improving heat exchange in hydrogen storage system[J]. International Journal of Hydrogen Energy, 2011, 11(36):6723-6738.

[30] Bhouri M, Goyette J, Hardy B J, et al. Numerical modeling and performance evaluation of multi-tubular sodium alanate hydride finned reactor[J]. International Journal of Hydrogen Energy, 2012, 2(37):1551-1567.

[31] Corgnale C, Hardy B, Chahine R, et al. Hydrogen desorption using honeycomb finned heat exchangers integrated in adsorbent storage systems[J]. Applied Energy, 2018, 213:426-434.

[32] Zheng H P, Wang C H, Liu Q M, et al. Thermal performance of copper foam/paraffin composite phase change material[J]. Energy Conversion and Management, 2018, 157:372-381.

[33] Mellouli S, Askri F, Abhilash E, et al. Impact of using a heat transfer fluid pipe in a metal hydride-phase change material tank[J]. Applied Thermal Engineering, 2017, 113:554-565.

[34] Pan M Q, Zhong Y J. Experimental and numerical investigation of a thermal management system for a Li-ion battery pack using cutting copper fiber sintered skeleton/paraffin composite phase change materials[J]. International Journal of Heat and Mass Transfer, 2018, 126:531-543.

[35] Xie Y Q, Tang J C, Shi S, et al. Experimental and numerical investigation on integrated thermal management for lithium-ion battery pack with composite phase change materials[J]. Energy Conversion and Management, 2017, 154:562-575.

[36] Wang X M, Xie Y Q, Day R, et al. Performance analysis of a novel thermal management system with composite phase change material for a lithium-ion battery pack[J]. Energy, 2018, 156:154-168.

[37] Gkanas E I, Grant D M, Khzouz M, et al. Efficient hydrogen storage in up-scale metal hydride tanks as possible metal hydride compression agents equipped with aluminium extended surfaces[J]. International Journal of Hydrogen Energy, 2016, 25(41):10795-10810.

[38] Wu Z, Yang F S, Zhang Z X, et al. Magnesium based metal hydride reactor incorporating helical coil heat exchanger: simulation study and optimal design[J]. Applied Energy, 2014, 130:712-722.

[39] Visaria M, Mudawar I. Coiled-tube heat exchanger for high-pressure metal hydride hydrogen storage systems – part 1. experimental study[J]. International Journal of Heat and Mass Transfer, 2012, 5(55):1782-1795.

[40] Visaria M, Mudawar I. Coiled-tube heat exchanger for high-pressure metal hydride hydrogen storage systems – part 2. computational model[J]. International Journal of Heat and Mass Transfer, 2012, 5(55):1796-1806.

[41] Tong L, Xiao J S, Yang T Q, et al. Complete and reduced models for metal hydride reactor with coiled-tube heat exchanger[J]. International Journal of Hydrogen Energy, 2019, 30(44):15907-15916.

[42] Laurencelle F, Goyette J. Simulation of heat transfer in a metal hydride reactor with aluminium foam[J]. International Journal of Hydrogen Energy, 2007, 14(32):2957-2964.

[43] Mellouli S, Dhaou H, Askri F, et al. Hydrogen storage in metal hydride tanks equipped with metal foam heat exchanger[J]. International Journal of Hydrogen Energy, 2009, 23(34):9393-9401.

[44] Arena S, Casti E, Gasia J, et al. Numerical simulation of a finned-tube LHTES system: influence of the mushy zone constant on the phase change behaviour[J]. Energy Procedia, 2017, 126:517-524.

[45] Garrier S, Delhomme B, de Rango P, et al. A new MgH_2 tank concept using a phase-change material to store the heat of reaction[J]. International Journal of Hydrogen Energy, 2013, 23(38):9766-9771.

[46] Ben Mâad H, Askri F, Ben Nasrallah S. Heat and mass transfer in a metal hydrogen reactor equipped with a phase-change heat-exchanger[J]. International Journal of Thermal Sciences, 2016, 99:271-278.

[47] Mellouli S, Ben Khedher N, Askri F, et al. Numerical analysis of metal hydride tank with phase change material[J]. Applied Thermal Engineering, 2015, 90:674-682.

[48] Tsai M L, Yang T S. On the selection of metal foam volume fraction for hydriding time minimization of metal hydride reactors[J]. International Journal of Hydrogen Energy, 2010, 20(35):11052-11063.

[49] Wang H, Prasad A K, Advani S G. Hydrogen storage systems based on hydride materials with enhanced thermal conductivity[J]. International Journal of Hydrogen Energy, 2012, 1(37):290-298.

[50] Ferekh S, Gwak G, Kyoung S, et al. Numerical comparison of heat-fin- and metal-foam-based hydrogen storage beds during hydrogen charging process[J]. International Journal of Hydrogen Energy, 2015, 42(40):14540-14550.

[51] Tong L, Xiao J S, Bénard P, et al. Thermal management of metal hydride hydrogen storage reservoir using phase change materials[J]. International Journal of Hydrogen Energy, 2019, 38(44):21055-21066.

[52] Talagañis B A, Meyer G O, Aguirre P A. Modeling and simulation of absorption–desorption cyclic processes for hydrogen storage-compression using metal hydrides[J]. International Journal of Hydrogen Energy, 2011, 21(36):13621-13631.

[53] Talagañis B A, Meyer G O, Oliva D G, et al. Modeling and optimal design of cyclic processes for hydrogen purification using hydride-forming metals[J]. International Journal of Hydrogen Energy, 2014, 33(39):18997-19008.

[54] Saitou T, Sugiyama K. Hydrogen purification with metal hydride sintered pellets using pressure swing adsorption method[J]. Journal of Alloys and Compounds, 1995, 1(231):865-870.

[55] Minko K B, Artemov V I, Yan'kov G G. Numerical simulation of sorption/desorption processes in metal-hydride systems for hydrogen storage and purification, part I: development of a mathematical model[J]. International Journal of Heat and Mass Transfer, 2014, 68:683-692.

[56] Minko K B, Artemov V I, Yan'kov G G. Numerical simulation of sorption/desorption processes in metal-hydride systems for hydrogen storage and purification, part II: verification of the mathematical model[J]. International Journal of Heat and Mass Transfer, 2014, 68:693-702.

[57] Minko K B, Artemov V I, Yan'kov G G. Numerical study of hydrogen purification using metal hydride reactor with aluminium foam[J]. Applied Thermal Engineering, 2015, 76:175-184.

[58] Artemov V I, Minko K B, Yan'kov G G. Numerical study of heat and mass transfer processes in a metal hydride reactor for hydrogen purification[J]. International Journal of Hydrogen Energy, 2016, 23(41):9762-9768.

[59] Dunikov D, Borzenko V, Malyshenko S. Influence of impurities on hydrogen absorption in a metal hydride reactor[J]. International Journal of Hydrogen Energy, 2012, 18(37):13843-13848.

[60] Xiao J S, Tong L, Yang T Q, et al. Lumped parameter simulation of hydrogen storage and purification systems using metal hydrides[J]. International Journal of Hydrogen Energy, 2017, 6(42):3698-3707.

[61] Yang J, Lee C H, Chang J W. Separation of hydrogen mixtures by a two-bed pressure swing adsorption process using zeolite 5A[J]. Industrial & Engineering Chemistry Research, 1997, 7(36):2789-2798.

[62] Zhang N N, Xiao J S, Bénard P, et al. Single- and double-bed pressure swing adsorption processes for H_2/CO syngas separation[J]. International Journal of Hydrogen Energy, 2019, 44(48):26405-26418.

[63] Ahn H, Chun C, Park M, et al. Thermal effects on the breakthrough curve of a hydrogen ternary system at a fixed bed[J]. Separation Science and Technology, 2001, 10(36):2121-2145.

[64] Lee C H, Yang J, Ahn H. Effects of carbon-to-zeolite ratio on layered bed H_2 PSA for coke oven gas[J]. AIChE Journal, 1999, 3(45):535-545.

[65] Ahn H, Yang J, Lee C H. Effects of feed composition of coke oven gas on a layered bed H_2 PSA process[J]. Adsorption, 2001, 4(7):339-356.

[66] Ahn S, You Y W, Lee D G, et al. Layered two- and four-bed PSA processes for H_2 recovery from coal gas[J]. Chemical Engineering Science, 2012, 1(68):413-423.

[67] Jee J G, Kim M B, Lee C H. Adsorption characteristics of hydrogen mixtures in a layered bed: binary, ternary, and five-component mixtures[J]. Industrial & Engineering Chemistry Research, 2001, 3(40):868-878.

[68] You Y-W, Lee D-G, Yoon K-Y, et al. H_2 PSA purifier for CO removal from hydrogen mixtures[J]. International Journal of Hydrogen Energy, 2012, 23(37):18175-18186.

[69] Lopes F V S, Grande C A, Rodrigues A E. Activated carbon for hydrogen purification by pressure swing adsorption: multicomponent breakthrough curves and PSA performance[J]. Chemical Engineering Science, 2011, 3(66):303-317.

[70] Silva B, Solomon I, Ribeiro A M, et al. H_2 purification by pressure swing adsorption using CuBTC[J]. Separation and Purification Technology, 2013, 118:744-756.

[71] Xiao J, Fang L, Bénard P, et al. Parametric study of pressure swing adsorption cycle for hydrogen purification using Cu-BTC[J]. International Journal of Hydrogen Energy, 2018, 30(43):13962-13974.

[72] Jamali S, Mofarahi M, Rodrigues A E. Investigation of a novel combination of adsorbents for hydrogen purification using Cu-BTC and conventional adsorbents in pressure swing adsorption[J]. Adsorption, 2018, 5(24):481-498.

[73] Moon D K, Park Y, Oh H T, et al. Performance analysis of an eight-layered bed PSA process for H_2 recovery from IGCC with pre-combustion carbon capture[J]. Energy Conversion and Management, 2018, 156:202-214.

[74] Brea P, Delgado J A, Águeda V I, et al. Comparison between MOF UTSA-16 and BPL activated carbon in hydrogen purification by PSA[J]. Chemical Engineering Journal, 2019, 355:279-289.

[75] Nikolić D D, Kikkinides E S. Modelling and optimization of hybrid PSA/membrane separation processes[J]. Adsorption, 2015, 4(21):283-305.

[76] Zhu X, Shi Y, Li S, et al. Two-train elevated-temperature pressure swing adsorption for high-purity hydrogen production[J]. Applied Energy, 2018, 229:1061-1071.

[77] Park Y, Moon D K, Kim Y H, et al. Adsorption isotherms of CO_2, CO, N_2, CH_4, Ar and H_2 on activated carbon and zeolite LiX up to 1.0 MPa[J]. Adsorption, 2014, 4(20):631-647.

[78] Moon D K, Lee D G, Lee C H. H_2 pressure swing adsorption for high pressure syngas from an integrated gasification combined cycle with a carbon capture process[J]. Applied Energy, 2016, 183:760-774.

[79] Kloutse F A, Hourri A, Natarajan S, et al. Hydrogen separation by adsorption: experiments and modelling of H_2-N_2-CO_2 and H_2-CH_4-CO_2 mixtures adsorption on CuBTC and MOF-5[J]. Microporous and Mesoporous Materials, 2018, 271:175-185.

[80] Kloutse F A, Hourri A, Natarajan S, et al. Experimental Benchmark Data of CH_4, CO_2 and N_2 Binary and Ternary Mixtures Adsorption on MOF-5[J]. Separation and Purification Technology, 2018, 197:228-236.

[81] Casas N, Schell J, Pini R, et al. Fixed bed adsorption of CO_2/H_2 mixtures on activated carbon: experiments and modeling[J]. Adsorption, 2012, 2(18):143-161.

[82] Park J H, Kim J N, Cho S H, et al. Adsorber dynamics and optimal design of layered beds for multicomponent gas adsorption[J]. Chemical Engineering Science, 1998, 23(53):3951-3963.

[83] Xiao J S, Li R P, Bénard P, et al. Heat and mass transfer model of multicomponent adsorption system for hydrogen purification[J]. International Journal of Hydrogen Energy, 2015, 14(40):4794-4803.

[84] Xiao J S, Peng Y Z, Bénard P, et al. Thermal effects on breakthrough curves of pressure swing adsorption for hydrogen purification[J]. International Journal of Hydrogen Energy, 2016, 19(41):8236-8245.

[85] Song C F, Liu Q L, Ji N, et al. Optimization of steam methane reforming coupled with pressure swing adsorption hydrogen production process by heat integration[J]. Applied Energy, 2015, 154:392-401.

[86] Golmakani A, Fatemi S, Tamnanloo J. Investigating PSA, VSA, and TSA methods in SMR unit of refineries for hydrogen production with fuel cell specification[J]. Separation and Purification Technology, 2017, 176:73-91.

[87] Ye F, Ma S, Tong L, et al. Artificial neural network based optimization for hydrogen purification performance of pressure swing adsorption[J]. International Journal of Hydrogen Energy, 2019, 11(44):5334-5344.

[88] Ma S, Tong L, Ye F, et al. Hydrogen purification layered bed optimization based on artificial neural network prediction of breakthrough curves[J]. International Journal of Hydrogen Energy, 2019, 11(44):5324-5333.

[89] Huang Q L, Malekian A, Eić M. Optimization of PSA process for producing enriched hydrogen from plasma reactor gas[J]. Separation and Purification Technology, 2008, 1(62):22-31.

[90] Tao W, Ma S, Xiao J S, et al. Simulation and optimization for hydrogen purification performance of vacuum pressure swing adsorption[J]. Energy Procedia, 2019, 158:1917-1923.

[91] Makarem M A, Mofarahi M, Jafarian B, et al. Simulation and analysis of vacuum pressure swing adsorption using the differential quadrature method[J]. Computers & Chemical Engineering, 2019, 121:483-496.

[92] Şenkal O, Kuleli T. Estimation of solar radiation over Turkey using artificial neural network and satellite data[J]. Applied Energy, 2009, 7(86):1222-1228.

[93] Fast M, Assadi M, De S. Development and multi-utility of an ANN model for an industrial gas turbine[J]. Applied Energy, 2009, 1(86):9-17.

[94] Yucel O, Aydin E S, Sadikoglu H. Comparison of the different artificial neural networks in prediction of biomass gasification products[J]. International Journal of Energy Research, 2019, 11(43):5992-6003.

[95] Morse G, Jones R, Thibault J, et al. Neural network modelling of adsorption isotherms[J]. Adsorption, 2011, 2(17):303-309.

[96] Rezakazemi M, Mohammadi T. Gas sorption in H_2-selective mixed matrix membranes: experimental and neural network modeling[J]. International Journal of Hydrogen Energy, 2013, 32(38):14035-14041.

[97] Sipöcz N, Tobiesen F A, Assadi M. The use of artificial neural network models for CO_2 capture plants[J]. Applied Energy, 2011, 7(88):2368-2376.

[98] Esfandiari K, Ghoreyshi A A, Jahanshahi M. Using artificial neural network and ideal adsorbed solution theory for predicting the CO_2/CH_4 selectivities of metal–organic frameworks: a comparative study[J]. Industrial & Engineering Chemistry Research, 2017, 49(56):14610-14622.

[99] Tian Q F, Zhang Y, Wu Y, et al. The cycle life prediction of Mg-based hydrogen storage alloys by artificial neural network[J]. International Journal of Hydrogen Energy, 2009, 4(34):1931-1936.

[100] Rahnama A, Zepon G, Sridhar S. Machine learning based prediction of metal hydrides for hydrogen storage, part I: prediction of hydrogen weight percent[J]. International Journal of Hydrogen Energy, 2019, 14(44):7337-7344.

Acknowledgement

Endless gratitude should be given to Prof. Jinsheng Xiao and Prof. Pierre Bénard for useful and patient directions through my Ph.D. project. I have benefited a lot from their profound insights and rigid attitude toward researching and teaching. Thanks also should be given to the wife of Prof. Jinsheng Xiao, Ms. Lijun Zhu, for encouragement and support in life when I studied in Université du Québec à Trois-Rivières, Canada.

Gratefulness to all my teachers and colleagues in Wuhan University of Technology and Université du Québec à Trois-Rivières, specifically:

Prof. Fuwu Yan, Prof. Guofang Zhang, Prof. Pang-Chieh Sui, Prof. Maji Luo, Prof. Yonghua Cai, Prof. Feng Ye, Prof. Weiqun Han, Dr. Tianqi Yang, Dr. Shuo Ma, Mr. Yunzhi Peng, Mr. Xiaoqing Mu, Mr Liang Fang, Mr Xu Wang, Mr. Ji Cheng, Mr. Shuhao Zhao, Mr. Yiqun Wang, Ms. Shanshan Deng, Ms. Qianqian Xin, Ms Nannan Zhang, Ms. Hafsa El Mghari, Ms. Li Wang, Ms. Wei Tao, Mr. Feng Li, Mr. Xiang Li, Mr. Xingguang Wang, Mr. Linhai Yuan, Mr. Longcheng Li, Mr.Koua Koua Alain Jesus, Mr. Xin Zhou, Mr. Chao Zhan, Mr. Ang Mei, Mr. Cheng Bi, Mr. Guanghui Tu and Mr. Hao Hu.

Prof. Richard Chahine, Prof. Jacques Huot, Prof. Adam Duong, Prof. Jacques Goyette, Prof. Yves Dubé, Dr. Ahmed Hourri, Ms. Anik Surprenant, Ms. Geneviève Côté, Dr. Lv Peng, Dr. Jingjing Liu, Dr.Follivi Kloutse Ayevide, Mr. David Durette and Mr. Marc-Antoine Page.

I wish to thank the financial supports from National Natural Science Foundation of China (NSFC Project No.51476120) and the China Scholarship Council (CSC), the Fonds de Recherche du Québec - Nature et Technologies (FRQNT) for a PBEEE fellowship and the Fundamental Research Funds for the Central Universities of China (Project No. 2016-JL-008).

Last but not least, I am grateful to my parents for giving me life and freedom. Thanks also should be given to my wife for constant support and companion. It is your love that makes me keep moving forward.

List of Publications

[1] Tong L, Xiao JS, Cai YH, Bénard P, Chahine R. Thermal effect and flow-through cooling of an adsorptive hydrogen delivery tank. *International Journal of Hydrogen Energy*, 2016; 41(36): 16094-16100.

[2] Tong L, Xiao JS, Yang TQ, Bénard P, Chahine R. Complete and reduced models for metal hydride reactor with coiled-tube heat exchanger. *International Journal of* Hydrogen Energy, 2019; 44(30): 15907-15916.

[3] Tong L, Xiao JS, Bénard P, Chahine R. Thermal management of metal hydride hydrogen storage reservoir using phase change materials. *International Journal of Hydrogen Energy*, 2019; 44(38): 21055-21066.

[4] Xiao JS, Tong L, Bénard P, Chahine R. Thermodynamic analysis for hydriding-dehydriding cycle of metal hydride system. *Energy* 2019. https://doi.org/10.1016/j.energy.2019.116535.

[5] Xiao JS, Tong L, Yang TQ, Bénard P, Chahine R. Lumped parameter simulation of hydrogen storage and purification systems using metal hydrides. *International Journal of Hydrogen Energy*, 2017; 42(6): 3698-3707.

[6] Ma S, Tong L, Ye F, Xiao JS, Bénard P, Chahine R. Hydrogen purification layered bed optimization based on artificial neural network prediction of breakthrough curves, *International Journal of Hydrogen Energy*, 44(2019) 5324-5333.

[7] Ye F, Ma S, Tong L, Xiao JS, Bénard P, Chahine R. Artificial neural network based optimization for hydrogen purification performance of pressure swing adsorption. *International Journal of Hydrogen Energy*, 44(2019) 5334-5344.